

Northumbria Research Link

Citation: Younus, Othman Isam (2022) Visible Light and Camera-based Receiver Employing Machine Learning for Indoor Positioning Systems and Data Communications. Doctoral thesis, Northumbria University.

This version was downloaded from Northumbria Research Link:
<https://nrl.northumbria.ac.uk/id/eprint/51139/>

Northumbria University has developed Northumbria Research Link (NRL) to enable users to access the University's research output. Copyright © and moral rights for items on NRL are retained by the individual author(s) and/or other copyright owners. Single copies of full items can be reproduced, displayed or performed, and given to third parties in any format or medium for personal research or study, educational, or not-for-profit purposes without prior permission or charge, provided the authors, title and full bibliographic details are given, as well as a hyperlink and/or URL to the original metadata page. The content must not be changed in any way. Full items must not be sold commercially in any format or medium without formal permission of the copyright holder. The full policy is available online: <http://nrl.northumbria.ac.uk/policies.html>

Visible Light and Camera-based Receiver Employing Machine Learning for Indoor Positioning Systems and Data Communications

Othman Isam Younus

A thesis submitted in partial fulfilment of the requirements
of Northumbria University for the degree of
Doctor of Philosophy

Research undertaken in the Faculty of Engineering and
Environment

May 2022

Dedication

To Dad,

*Though you never got to see this
You're in every page
this humble work is a sign of my love to you . . .*

To you,

*The reader of this thesis
Who strives to make this world a better place*

Abstract

Indoor location-based services have played a crucial role in the development of various Internet of Things applications over the last few decades. The use of radio frequency (RF)-based systems in indoor environments suffers from additional interference due to the high penetration rate and reflections of the RF, which may severely affect positioning accuracy. Alternatively, the optical technology using the existing light-emitting diode (LED)-based lights, photodetectors (PDs), and/or image sensors could be utilised to provide indoor positioning with high accuracy. Because of its resilience to electromagnetic interference, license-free operation, large bandwidth, and dual-use for illumination and communication, visible light positioning (VLP) systems have shown great potential in achieving high-precision indoor positioning. This thesis focus is on investigating VLP systems based on employing a single PD, or an array of PDs in the form of a single image sensor (i.e. a camera) for both localization and data communication. Following a comprehensive literature review on VLP, the key challenges in existing positioning methods for achieving a low-cost, accurate, and less complex indoor positioning systems design are highlighted by considering the design characteristics of an indoor environment, position accuracy, number of light-emitting LED, PD, and any additional sensors utilized. The thesis focuses on the major constraints of VLP and provides novel contributions. In most reported VLP schemes, the assumptions of fixed transmitter (Tx) angle and height may not be valid in many physical environments. In this work, the impact of tilting Tx and multipath reflections are investigated. The findings demonstrated that tilting Tx can be beneficial in VLP by leveraging the influence of reflections from both near- and far-walls. It also showed that proposed system offers a significant accuracy improvement by up to ~66% compared with a typical non-tilted Tx VLP system. Furthermore, increasing robustness of image sensor-based receiver (Rx) is a major challenge, which is being addressed using a novel angle of arrival-received signal intensity and a single LED. Experimental results show that the proposed algorithm can achieve a three-dimensional root mean squared error of 7.56 cm. Visible light communications employing a camera-based Rx is best known as optical camera communications (OCC), which can also be used for VLP. However, in OCC the transmission data rate is mainly limited by the exposure time and the frame rate of the camera. In addition, the camera's sampling introduces intersymbol interference

Abstract

(ISI), which will degrade the system performance. In this thesis, a VLP system with an artificial neural network-based equaliser with the adaptive algorithm is proposed for the first time to mitigate ISI and therefore increase the data rate. The data rates achieved were the highest in the OCC field, recorded as 12 kbps at the exposure time of 2, 1, and 0.5 ms using a single source and the Manchester line code non-return to zero encoded signal. Finally, a non-flickering Constant Power- Pulse-amplitude modulation-based OCC system using a single LED is proposed and investigated offering data rates of up to 18.6 and 24.4 kbps with and without the equalization, respectively. The quality of the received signal is assessed in terms of eye diagrams, system linearity, and the bit error rate performance.

Acknowledgement

First and foremost, I would want to convey my heartfelt appreciation to the individuals who assisted me in shaping my PhD and with whom I have experienced this wonderful journey. The first person I would like to thank is Prof. Fary Ghassemlooy (my principal supervisor) for his ongoing support, motivation, enthusiasm, and immense knowledge. He has been an outstanding mentor as well as a wonderful friend. His advice was vital throughout the research process, as evidenced by the various collaborations and research outputs I have produced through this journey. Besides my advisor, I would like to thank the rest of my supervisory team including Dr Hoa Le-Minh, Dr Luis Alves, and Dr Paul Haigh, for their encouragement, and the insightful comments.

Special thanks to Dr Navid Bani Hassan and for the invaluable input on the research and the collaboration, positive support, and valuable feedback. Many thanks to Prof. Stanislav Zvánovec and all of my colleagues at Czech Technical University in Prague for their assistance when I was conducting research there.

My sincere thanks also goes to all members of the European Collaborative Research Network and my labmates for the stimulating discussions, the sleepless nights we spent working together before deadlines, and all the fun we've had over the years, specifically Dr Neha Chaudhary, Ms. Zun Htay, Dr. Xicong Li, Dr. Mojtaba Abadi, Mr. Nithin Mohan, Ms. Rida Zia-ul-Mustafa, Dr. Vicente Matus, Ms. Elena Niarchou, and Mr. Cristo Jurado-Verdugo.

In addition, I would like to present my sincere thankfulness to my dear Mother and my late father, who will be unable to read this since he departed this world last August, for their great role in my life and their innumerable sacrifices for me and for the rest of my cherished family. Many thanks to my siblings Nawar, Ahmed, and Amenah for their spiritual support throughout my life. I will also thank my brother in law, baby Yousef, my aunt and all other relatives for their support.

A debt of gratitude is also to my friends for their inspiration and encouragement during my academic career. Dr. Elhasanin Salem, Dr. Zaid Abdullah, Dr. Cecilia Pesce, Ms. Nassima Kadri, Mr. Omar Sameer, Mr. Baraa Hussein, and Mr. Mohamed AlNaaib. The time I spent with them is the most valuable memory I have. I count myself lucky to have met you all. Please forgive me if I have forgotten to thank you.

Also, I am indebted to Almighty for providing me with the willpower and strength to continue on this road, as well as the opportunity to meet the entire ISOC legendary team, of which I am honoured to be a part, and for a wonderful time in the UK.

Foremost, I would like to thank everyone who has supported me financially, including the Northumbria University for sponsoring the full PhD scholarship and various IEEE and university grants for conference attendance and journal charges. I'd also want to thank the European Cooperation in Science and Technology for funding my short-term scientific mission through.

Declaration

I declare that the work contained in this thesis is entirely mine and that no portion of it has been submitted in support of an application for another degree or qualification in this, or any other university, or institute of learning, or industrial organization.

Any ethical clearance for the research presented in this commentary has been approved. Approval has been sought and granted through the Researcher's submission to Northumbria University's Ethics Online System / external committee on 27 January 2020 [Submission Ref: 21486].

I declare that the Word Count of this Thesis is 31,042 words

Othman Isam Younus

17th May 2022

Table of Contents

Abstract	i
Acknowledgement.....	iii
Declaration	iv
Table of Contents	v
List of Figures	viii
List of Tables.....	xii
List of Abbreviations.....	xiii
Glossary of Symbols	xv
Chapter 1	19
Introduction	19
1.1 Background	19
1.2 Problem Statement	21
1.2.1 Impact of The Tx Tilting Angles	21
1.2.2 Multipath Reflection Impact.....	22
1.2.3 IS-VLP Utilization.....	22
1.2.3.1 Limited frame rate	23
1.2.3.2 Limited bandwidth.....	23
1.2.3.3 Flickering issue	23
1.2.3.4 Number of TxS	23
1.3 Research Aims and Objectives.....	25
1.4 Original Contributions to Knowledge.....	26
1.5 Thesis Structure.....	29
1.6 List of Publications and Awards	30
1.6.1 Peer Reviewed Journal Papers	30
1.6.2 Peer Reviewed Conference Papers	31
1.6.3 Posters.....	32
1.6.4 Invited Keynote Speaker.....	32
1.6.5 Training School.....	32
1.6.6 Awards.....	32
Chapter 2	33
Overview of Indoor Positioning Systems	33
2.1 Introduction	33
2.2 Indoor Positioning System	33

Table of Contents

2.3	Indoor Positioning Technologies	35
2.4	VLC-based-IPSS Techniques	38
2.4.1	Mathematical Method	38
2.4.1.1	Fingerprinting Technique	38
2.4.1.2	Range-free Technique	42
2.4.1.3	Range-based Technique	45
2.4.2	Sensor-Assisted Method	53
2.4.2.1	Image Positioning Camera-based VLC IPS	53
2.4.2.2	Sensor Fusion	54
2.4.3	Positioning Optimization Method	57
2.4.3.1	Machine Learning Techniques	57
2.4.3.2	Filtering Techniques	58
2.4.3.3	Other Estimation Techniques	59
2.5	Summary	60
Chapter 3	61
	An Indoor Visible Light Positioning System Using Tilted LEDs with High Accuracy	61
3.1	Introduction	61
3.2	Proposed VLP System Model	64
3.3	Positioning Algorithm	71
3.3.1	Distance Estimation Using Polynomial Regression	71
3.3.2	LLS Estimation	72
3.4	Results and Discussion	73
3.4.1	Impact of the Tx Tilting on the Radiation Pattern	73
3.4.2	Polynomial Fitting	75
3.4.3	Impact of the Tx Tilting and the Altitude of F on VLP	77
3.4.4	Uniformity	79
3.5	Summary	81
Chapter 4	82
	A Unilateral 3D Indoor Positioning System Employing OCC	82
4.1	Introduction	82
4.2	System Model	86
4.2.1	ROI Detection Using CHT Algorithm	88
4.2.2	RSSI- based IS Measurements	89
4.2.3	Ellipse-shaped Mask Generation	89

Table of Contents

4.2.4	AoA- based IS Measurements	90
4.3	Results and Discussion.....	92
4.3.1	The Exposure Time Impact on ROI.....	93
4.3.2	The Accuracy of the Proposed VLP system	96
4.4	Summary	97
Chapter 5	98
	Artificial Neural Network Equalizer	98
5.1	Introduction	98
5.2	CMOS IS Modelling in OCC System	100
5.3	Artificial Neural Network Equaliser	102
5.4	System Model.....	107
5.5	Results and Discussion.....	113
5.6	Summary	117
Chapter 6	118
	The Utilization of ANN Equalizer and a Constant Power-PAM in RS-Based OCC System.....	118
6.1	Introduction	118
6.2	Constant Power-PAM in RS-Based OCC System	121
6.3	ANN Equalizer.....	124
6.4	Experimental Setup	126
6.5	Results and Discussions	132
6.6	Summary	138
Chapter 7	139
	Conclusion and Future Works	139
7.1	Conclusions	139
7.2	Future Works.....	142

List of Figures

Figure 1-1. Summary of original contributions.	28
Figure 2-1. The entire electromagnetic spectrum. The combined infrared and visible light spectra are 2600 times larger than the entire RF spectrum [61].	35
Figure 3-1. An example of a reflected light ray in case of LED tilt: (a) near-wall reflections case, and (b) far wall reflections case.	65
Figure 3-2. The proposed indoor VLP system with the tilted Tx.	67
Figure 3-3. Block diagram of the proposed VLP system.....	69
Figure 3-4. Positioning based on RSS.	72
Figure 3-5. The received power distributions for the proposed system for the Tx's with: (a) no tilting, and (b) tilting.....	74
Figure 3-6. The distance estimation for Tx-k using the PR method employed in S2 for the Tx's with: (a) no tilting, and (b) tilting.	76
Figure 3-7. The measured quantile function at χ of 90% for various D_r for LLS with and without the tilted Tx's.	77
Figure 3-8. The measured quantile function at χ of 90% for various z_F values for: (a) S1, and (b) S2.	79
Figure 3-9. The uniformity of light distribution in different D_r w/o and with the tilting Tx's.....	80
Figure 4-1. System model for the proposed positioning method: (a) Tx block diagram, (b) projection of a 3D object on a 2D image, and (c) flowchart of detection and extraction of information required for positioning.....	87
Figure 4-2. The geometrical model for the proposed system.....	91

List of Figures

Figure 4-3. A photograph of the experimental setup of the proposed AoA-RSS-based VLP system.....	92
Figure 4-4. The ROI detected at the captured $\mathbf{F}_{U \times V}^k$ for a range of EV in the image domain.....	94
Figure 4-5. The intensity profiles versus the EV for the captured images and F-stop of f/3.5 for: (a) entire image, and (b) the ROI detected region ($\mathbf{F}_{U \times V}^k$).	94
Figure 4-6. The PSNR as a function of EV for the entire frame and the ROI detected region.....	95
Figure 4-7. The captured frame with and without the proposed method for: (a) conventional $FU \times Vm, k$, (b) generated ellipse-shaped mask $MU \times V$, and (c) the output frame ($FU \times V k \odot MU \times V$).	96
Figure 4-8. The normalized received power versus the EV for the conventional and proposed systems.	96
Figure 4-9. The comparison between the real and estimated 3D position of the Rx when moving along: (a) x -axis ($y = 0; z = 88$ cm), (b) y -axis ($x = 0; z = 88$ cm), and (c) z -axis ($x = 0; y = 0$).	97
Figure 5-1. (a) An example of the frame acquisition based on rolling-shutter CMOS sensor. (b) The LSI model of a CMOS image sensor receiver.	102
Figure 5-2. An example of the frame acquisition based on the RS CMOS sensor.	103
Figure 5-3. Block diagram of a single-hidden-layer ANN based equaliser.	104
Figure 5-4. (a) System block diagram for OCC using LED and rolling shutter CMOS sensor. (b) The proposed structure of data frame packet.	107
Figure 5-5. The received signal at a signal bandwidth of 400 Hz with T_{exp} of 1 ms: (a) without DC gain normalization and (b) with normalization.	110

List of Figures

Figure 5-6. BER and MSE as a function of the number of neurons in input layer k_i , and the hidden layer k_h and N_{bit} of 192.	113
Figure 5-7. Image Sensor frequency response with different exposure time.....	114
Figure 5-8. BER measurements of the system with and without equalisation in respect to effective data rates of different exposure times with Rf of 30.....	115
Figure 5-9. Eye diagram of the received signal at a signal bandwidth of 400 Hz of: (a) without deploying the ANN-based receiver, and (b) after applying the proposed receiver.	116
Figure 5-10. ANN system behaviour over time to calculate the faster convergence of different training algorithms for hyperbolic tangent sigmoid activation function.....	117
Figure 6-1. Defining flicker index [261], [262].	123
Figure 6-2. An example of a generated packet signal with f_{Tx} of 220 Hz.....	123
Figure 6-3. A structure of the k^{th} neuron in the layer m	125
Figure 6-4. The CP 4-PAM OCC scheme: (a) system block diagram, and (b) photograph of the experimental setup.	127
Figure 6-5. An example of the received Q^{th} Tx packet signal at a T_{exp} of 2 ms: (a) without DC gain normalization, and (b) with normalization.	128
Figure 6-6. Measured and estimated bandwidth of the for IS with T_{exp} of 2 ms.....	132
Figure 6-7. Examples of the frame acquisition based on CIS for CP 4-PAM and f_{Tx} of: (a) 220 Hz, (b) 320 Hz, (c) 420 Hz, (d) 520 Hz, (e) 1120 Hz, and (f) 1520 Hz.	133
Figure 6-8. Examples of the captured eye diagrams of the CIS received signal for CP 4-PAM with f_{Tx} of: (a) 220 Hz, (b) 320 Hz, (c) 420 Hz, (d) 520 Hz, (e) 1120 Hz, and (f) 1520 Hz.	134

List of Figures

Figure 6-9. An example of the transmitted and received signal with and without equalization for CP 4-PAM and N_{pps} of 18.5 row pixels/symbol: (a) training sets, and (b) testing sets.	135
Figure 6-10. The eye linearity against N_{pps} for the proposed system with and without equalization and for T_{exp} of 2 ms.....	136
Figure 6-11. The BER measurements as a function of N_{pps} for the proposed system with and without equalization and for T_{exp} of 2 ms.....	137

List of Tables

Table 2.1 Comparison of existing IPS technologies	37
Table 2.2 Comparison of existing fingerprinting based VLP.	41
Table 2.3 Comparison of existing rang-free based VLPs.	44
Table 2.4 Comparison of existing AoA range-based VLPs.	47
Table 2.5 Comparison of existing ToA or TDoA range-based VLPs.	49
Table 2.6 Comparison of existing RSS range-based VLPs.	52
Table 2.7 Listed studies of sensor-assisted based VLPs.	56
Table 3.1 The key system parameters.	71
Table 3.2 The values of tilted Tx normal for all Txs.	74
Table 3.3 The coefficients of the polynomial fitted curve for the scenario S2.	76
Table 4.1 Key system parameters.	83
Table 4.2 System parameters.	93
Table 4.3 The data for the detected ROI from Figure 4-4.	94
Table 5.1 System parameters.	111
Table 6.1 Proposed CP 4-PAM levels.	123
Table 6.2 System parameters.	131
Table 6.3 Results with Rf of 30 fps and CIS width of 1024 px.	134
Table 6.4 Effective R_b at different ISs resolutions at the FEC limits.	137

List of Abbreviations

Short Form	Description
ADT	Angle diversity transmitter
AoA	Angle of arrival
ANN	Artificial neural network
ANN	Artificial neural network
BP	Back-propagation
BER	Bit error rate
CHT	Circular Hough transform
CSK	Colour-shift keying
CMOS	Complementary metal oxide-semiconductor
CNN	Convolution neural network
COVID-19	Coronavirus disease 2019
CDF	Cumulative distribution function
D2D	Device-to-device
FoV	Field of view
FPS	Frames-per-second
FM	Frequency modulation
GPS	Global positioning system
IS	Image sensor
Rx	Integrated receiver
ITS	Intelligent transport systems
IoT	Internet of thing
LEDs	Light-emitting diodes
LoS	Line of sight
LLS	Linear least square
LPF	Low-pass filter
MLC	Manchester line code
MSE	Mean square error
MLP	Multi-layer perceptron
MIMO	Multiple-input multiple-output
NLoS	Non-line of sight

List of Abbreviations

NLLS	Nonlinear least square
NRZ	Non-return to zero
OOK	On-off keying
OCC	Optical camera communication
OWC	Optical wireless communications
PD	Photodiode
PR	Polynomial regression
PA	Positioning accuracy
PRBS	Pseudorandom binary sequence
PAM	Pulse amplitude modulation
RF	Radio frequency
RSS	Received signal strength
RSSI	Received signal strength indicator
Rx	Receiver
RGB	Red-green-blue
RBP	Resilient back-propagation
RS	Rolling shutter
RMS	Root mean square
RMSE	Root mean square error
3D	Three-dimensional
TDoA	Time difference of arrival
ToA	Time of arrival
Tx	Transmitter
2D	Two-dimensional
UFSOOK	Under-sampled frequency shift on-off keying
UPSOOK	Under-sampled phase shift on-off keying
VLC	Visible light communication
VLP	Visible light positioning
AWGN	White Gaussian noise
WCS	World coordinate system

Glossary of Symbols

Parameter	Description
I_S	1 st chip for the intensity of the PAM symbol
z_i^Q	Accumulated intensities for all pixels at each row
N_{row}	Acquired number of samples
y_k	Actual received symbol
θ_{AoA}	Angle of arrival on the IS
I_{Rx}	Average pixel values for the received symbols
f_{Tx}	Bandwidth of the transmitted signal
$F_{U \times V}$	Captured frame
$G_{U \times V \times 3}$	Captured frames of illumination gain (DC signal only)
$H_{U \times V}^{total}$	Channel impulse response
$h(u, v)$	Channel response of a single pixel (u, v) ,
$g(\varphi)$	Concentrator at the Rx
Rb	Data rate
$\delta(t)$	Dirac delta function
a_{FoV}	Distance between the LED projection centre and the centre of IS plane
$d_{w,r}$	Distances between the reflective area and the Rx
$M_{U \times V}$	Ellipse-shaped mask
A_r	Entrance pupil of the lens
C_{PD}	Equivalent capacitance
E_n	Error cost function
$\ \cdot\ $	Euclidean norm

Glossary of Symbols

T_{exp}	Exposure time
F	Focal length
f	Focal length
R_f	Frame rate
Rf	Frame rate
Δf	Frequency resolution
$T_s(\varphi)$	Gains of the optical filter
b_{FoV}	Half FoV of the vertical frame resolution
u	Horizontal pixels in the image plane
d_k	Ideal symbols
$n(t)$	Induced noise
$\omega_{w,r}$	Irradiance angle between the reflective area and the Rx
A	IS gain
H_{CoC}	Kernel of the circle of confusion
m	Layer number
η	Learning rate parameter.
R_t	LED's Lambertian pattern
$\theta_{\frac{1}{2}}$	Light source irradiance half-power angle
I_{max}	Maximum possible pixel value on the captured frame
I_{ave}	Mean intensity value of all symbols
N_{bit}	Number of bit per frame
N_{pps}	Number of row pixels per symbol
n	Number of rows
n_{samp}	Number of samples per symbol

Glossary of Symbols

$o_k^{(m)}$	Output of the k^{th} neuron
Qth	Packet number
A_r	PD area
R	PD Responsivity
V	Pixel row
I_{Tx}	Pixel values for transmitted symbols
ε_p	Positioning error
$s(t)$	Pseudorandom binary sequence
$x(t)$	Received optical signal at the pixel (U, V) at time t
PR	Received power
$P_r(u, v)$	Received power at a single pixel (u, v)
P_{R-LoS}	Received power for LoS
P_{R-NLoS}	Received power for NLoS
φ	Receiving incident angle
$\varphi_{w,r}$	Receiving incident angle between the reflective area and the Rx
ρ	Reflection coefficient
L	Required distance between the LED and the Rx
F_s	Rolling rate of IS
T_{sample}	Sampling duration
Dr	Side length
(a_c, b_c)	Simple light source located at a center point of with respect to image coordinate system
β	Slope factor
P_{bit}	Symbol per packet
T_{sym}	Symbol period

Glossary of Symbols

$h(t)$	System response
N_{m-1}	Tapped delay
$o(m-1)$	Tapped delay line
$P_{U \times V \times 3}^Q$	The captured frames
$H_{U \times V}$	The channel impulse response of the captured frame (U, V) .
j	The pixel's row index number
$v_k^{(m)}$	Threshold factor
ω_k^{tilt}	Tilted irradiance angle from the k^{th} Tx to the Rx
\hat{t}_k	Tilted Tx normal
P_t	Transmitted power
(x_c, y_c)	Tx centre coordinates
r_c	Tx Radius
$w_{kn}(t+1)$	Updated weight
$\overrightarrow{(T_k)}$	Vector that represents the difference between the coordinates of the k^{th} Tx and point F (x_F, y_F, z_F) ,
v	Vertical pixels in the image plane
w_{kn}	Weight between the junction point of x_k and k^{th}
ξ	Weighted input
$w_{kn}^{(m)}$	Weights of the n^{th} input to the k^{th} neuron

Chapter 1

Introduction

1.1 Background

Precise localization and tracking technologies for use in indoor and outdoor environments have attracted a considerable amount of attention for centuries. For millennia, humans have developed various tools to determine their accurate location, some include tracking the movements of the sun with sundials, the use of water clocks, candle clocks, sextants, hourglasses, clocks, accelerometers, maps, etc. The advent of the global positioning system (GPS) has facilitated position estimation in outdoor environments and is considered as one of the major successes of modern human civilization. Unfortunately, GPS and similar satellite navigation systems cease its operation in indoor environments due to the lack of line-of-sight (LoS) links to satellites. Indoor positioning systems (IPSs) have a prominent contribution to day-to-day activities in applications including health care centres, airports, shopping malls, manufacturing, underground locations, etc. Alternatively, both radio frequency (RF) and optical wireless-based technologies could be adopted for localization [1], [2]. It may include the use of Bluetooth [3], [4], ultrasound [5], wireless local area network [6], the ultra-wide band [6], [7], and RF identification [8], [9]. The accuracy of IPSs using low frequencies RF technology is relatively low due to the high multipath fading as compared with optical signals. For instance, existing localization research proved its ability to provide a degree of accuracy measured in meters using different technologies such as geo-magnetism [10], WiFi [11], and frequency modulation (FM) broadcast technology [12]. Although the RF-based global positioning system offer higher penetration rates with reduced accuracy (i.e., in the range of a few meters), it does not work well in indoor environments (and not at all in certain cases such as tunnels, mines, etc.) due to the very weak signal and no direct access to the satellites [1], [2], [9].

Many researchers have attempted to provide a standard solution for indoor positioning, however, diverse technologies have been pursued based on the accuracy and cost trade-offs. Light-emitting diodes (LEDs)-based visible light communication (VLC) systems

have been introduced in recent years, which have shown great potential in achieving high-precision indoor positioning due to the use of optical signals. These systems are known as visible light positioning (VLP), in which VLC signals are utilized to broadcast anchor locations prior to detecting these signals using off-the-shelf resource-constrained smart devices to enable the internet of things (IoT) [13], [14]. VLP technologies have gained increasing attention due to its robustness to RF interference, operate on a free license, and attain cost-effectiveness and directive propagation [1]. In addition, the local character of light reduces the impact of reflections, which leads to high accuracy and low overhead costs.

Most research reported on VLP has focused on the investigation of geometrical properties using triangulation/trilateration, fingerprinting, or proximity methods to determine the transmission distance based on establishing a one-to-one relationship between the target location and its received signal strength (RSS). In such works, the use of well-developed algorithms, which have been developed for other technologies was leveraged [15], including the angle of arrival (AoA) [16], time of arrival (ToA) [17], [18], proximity, scene analysis, and RSS [19]. RSS, AoA, and ToA have been explored in VLP systems with the positioning error of 10 to 40 centimeters [20]. Proximity and scene analysis (i.e., fingerprinting) are considered the simplest methods with relatively low positioning errors i.e., typically in a range of 10 to 45 cm, depending on the fingerprint database [16], [17], [21]. Furthermore, the recent advent of machine learning (ML) technology has resulted in increased localization performance using the fingerprinting method. In [22]–[24], the authors showed an ML-based RSSI fingerprinting with a few centimetres of precision and decreased latency at the cost of increased system complexity.

In the scene analysis technique, the estimation process of the relative position can be obtained by comparing the measured value with a pre-measured location of each position and then matching it to determine the real position. However, the measurement can be affected by the distributions of base stations, i.e., transmitters (Tx), shadowing and blocking, as well as the absolute location (i.e., probabilistic and correlation) dependency on pattern recognition techniques [16].

In VLC-based IPSs LEDs are used as Tx while a single photodiode (PD) or an array of PDs forming a CIS PDs or image sensors (ISs) (i.e., cameras) are used as the receiver (Rx). Compared to PDs, ISs-based IPSs offer several key features such as (i) providing much more useful information on the location of LEDs for use in vision processing based

algorithms; (ii) the ability to separate light sources, thus no need for complex multiplexing mechanisms; (iii) offer parallel transmission capabilities; and (iv) offering significantly high accuracy which may be utilized in autonomous navigation system where accuracy plays a crucial factor in intelligent transportation systems (ITS) to ensure the safety of the pedestrians.

A VLP using two PDs and an IS was proposed in [21], [25], [26]. Note, VLC with IS (composed of a large PD array) naturally fits well with multiple inputs multiple-output systems in indoor and outdoor applications. In IS-based VLP, image-processing techniques can be used to determine the position but at the cost of increased complexity [27]. Note that, in VLP the transmission speeds (i.e., data rates) of the PD and IS are not critical at all since the aim is to achieve positioning with high accuracy [28]. Likewise, the IS deployment enables range imaging to resolve the distance between the IS and the subject for each point of the image based on the time-of-flight, which can be obtained through measuring the round trip time of an artificial light signal provided by a laser or an LED [29]. Furthermore, the usage of IS may be used to generate the illusion of a three-dimensional picture. The illusion of depth is achieved in images or movies by providing a separate image to each eye [30]. In this Chapter indoor positioning systems (IPS) based VLC system, its merits and challenges were outlined. The aims, objectives and the original contributions of this research are also presented. Likewise, the structure of this thesis, a list of publications generated during the PhD research and awards are presented.

1.2 Problem Statement

1.2.1 Impact of The Tx Tilting Angles

Most of the research on VLC-based IPS reported are on the investigation of geometrical properties based on triangulation/trilateration, fingerprinting or proximity methods to determine the transmission distance via the received signal strength (RSSI) based on intensity modulation, AoA [8], or ToA [9]. In most of these methods, it is often assumed that power from two or more different light sources can be easily separated. In addition, to remove angular dependency in RSS based localization, it is also assumed that the height of the receiver is fixed, and the receiver is in a parallel plane to the transmitters [31]. However, the assumptions of fixing the angle, height, and the Rx pose cannot be accommodated easily in a physical environment. Likewise, additional problems such as

the computational and the implementation costs and system complexity needs to be further investigated.

1.2.2 Multipath Reflection Impact

The multipath effects on the accuracy of the VLP system were not fully and consistently considered. For example, the works reported in [23], [24] considered only LoS paths in the analysis of positioning performance without taking into account the multipath nature of the channel. Note, for systems using TxS and RxS with a wide beam and a field of view (FOV), respectively the impact of multipath reflections is inevitable and therefore must be considered as was reported in [34]. The results showed that, the positioning errors of 0.4 and 46.4 cm were achieved for the entire room without and with multipath reflections, respectively.

1.2.3 IS-VLP Utilization

Advances made in optical systems have triggered image-based positioning methods to become an attractive solution for indoor navigation systems. In which, the camera can either utilise its received optical reflectiveness characteristics of the obtained scenes (measurements of visual features), or to receive the transmitted coordinates of LEDs by means of optical camera communications (OCCs). Moreover, from the received information, it is possible to estimate the distances between LEDs and the camera, and so, the position of the camera [35].

In addition, ISs (i.e., cameras) are now considered the key sensor for enabling the IoT applications as part of the current and future smart environments, in which complementary metal-oxide-semiconductor (CMOS) ISs have been the most widely used devices in many applications in the last decade, with a revenue quadrupling between 2010 and 2019 to reach over \$18 billion [36]. As a result, the ability to construct an IS-based VLC link to enable various applications like as location and sensing to supplement vision might be regarded as an emerging technology. However, VLC systems using LEDs and either a single PD or camera for localization and communication purposes are still in the preliminary stages. Several factors need to be taken into account when establishing these systems as:

1.2.3.1 Limited frame rate

The drawbacks of ISs-based Rx are low transmission bandwidth due to the camera frame rate R_f limitations and higher costs compared with PDs [35]. The maximum data rates of conventional commercial cameras are relatively low within a range of a few kbps [37]–[44]. Different approaches can be adopted to improve the data rates in OCC with CMOS-based ISs including (i) high-speed cameras, which are highly costly and with limited applications; (ii) multiple transmitters, which may suffer from flickering [45]; and (iii) a special IS with a built-in PIN PD array has been used to increase the data rate to 55 Mbps using an optical orthogonal frequency division multiplexing [46]. However, the fabrication process of this IS is too complex and not commercially available. Limited bandwidth

The IS requires a higher sampling duration and lower number of quantization levels compared with the PDs due to the light integration time (known as the exposure time T_{exp}), and the built-in analog to digital converter circuit [2]. The sequential-readout nature of CMOS IS-based Rx allows each pixel-row to capture the incident light at a different time, thus resulting in the so-called rolling shutter (RS) effect [2]. Note that, the performance of VLC with IS-based Rx is limited mainly by the camera capabilities, i.e., the frame rate R_f , T_{exp} , and FoV. As a result, in OCC, the transmission bandwidth is rather low and limited to a few tens of kHz compared to the PD-based VLC systems [35].

1.2.3.2 Flickering issue

In OCC, lower R_b may result in the flickering effect at the Tx [3, 4]. In IEEE 802.15.7m standard [5], different schemes have been proposed for OCC to mitigate flickering and to increase R_b [6]. For example, in [7], an optical orthogonal frequency division multiplexing VLC with a special IS-based Rx with a built-in PD-array was used to achieve a very high R_b of 55 Mbps. However, the fabrication process of the IS was too complex and, therefore, not commercially available.

1.2.3.3 Number of TxS

The majority of the studies in the IS-based VLP literature reviews used either multiple LEDs for positioning or an extra sensor to determine the location. However, in most scenarios, the narrow FoV of the front-facing camera receiver restricts the number of TxS

being captured at the IS, thus making bilateration or trilateration impractical. In addition, unilateration allows less complex and low-cost implementation of the VLC system. Also, the deployment of more LEDs will certainly add some constraints to the implementation of VLP.

1.3 Research Aims and Objectives

The aim of this research is to carry out comprehensive mathematical analysis, model development and experimental investigations of VLC system using LEDs and either a single PD or a camera for localization and communication purposes. To achieve the aim of this thesis, the key objectives of the study are:

- Carry out in-depth literature surveys and analytical studies on indoor localization-related works.
- System design and performance evaluation of VLP system with multipath induced reflections. Furthermore, to develop and simulate a novel approach to investigate and mitigate the influence of LED tilting on positioning accuracy.
- Experimental implementation of novel IS based VLPs to mitigate the impact of the exposure times and reduce the induced positioning errors.
- Develop an artificial neural network-based equalizer to ameliorate the low-pass filtering effect of the camera sampling duration of the RS-based communication system to overcome the bandwidth limitation of the camera receiver.
- To establish a flickering-free OCC system with improved data rates using a single LED and an artificial neural network (ANN)-based equalizer. Furthermore, to develop an efficient signal extraction algorithm for the proposed system.

1.4 Original Contributions to Knowledge

As outcomes of the conducted research, the following original contributions to the research field have been made:

1. In Chapter 3, the use of the Tx titling angles is leveraged to improve the IPS accuracy. The proposed scheme offers a significant accuracy improvement of up to ~66% compared with a typical non-tilted Tx VLP at a dedicated location within a room using a low complex linear least square algorithm with polynomial regression. The effect of tilting the Tx on the lighting uniformity is also investigated (see research output J3).
2. In Chapter 4, the usage of a visible light positioning system in an indoor environment was investigated to deliver a three-dimensional (3D) high-accuracy solution.. A novel method was proposed and experimentally tested to mitigate the error induced by the lens at the receiving side (see research output J1).
3. In Chapter 5, An ANN-based equaliser with the adaptive algorithm is employed for the first time in the field of OCC to mitigate ISI and therefore increase the data rate. Experimental test-bed for the proposed system was developed to evaluate the system performance in terms of the data rate, bit error rates (BER) and eye diagrams (see research output J10).
4. In Chapter 6, comprehensive and systematical investigation of the applicability of constant power 4-level pulse amplitude modulation for the LED- and camera-based VLC is presented. Furthermore, an experimental testbed of a non-flickering system using a single light-emitting diode is developed. The performance of the proposed system is evaluated in terms of the Tx's frequency, eye diagrams, and

the BER with and without the ANNs-based equalizer (see research output J6, and C21).

The summary of the contributions of this thesis is illustrated in Figure 1.1 where the coloured blocks show the research works carried out (with brief descriptions below) and their respective Chapter locations.

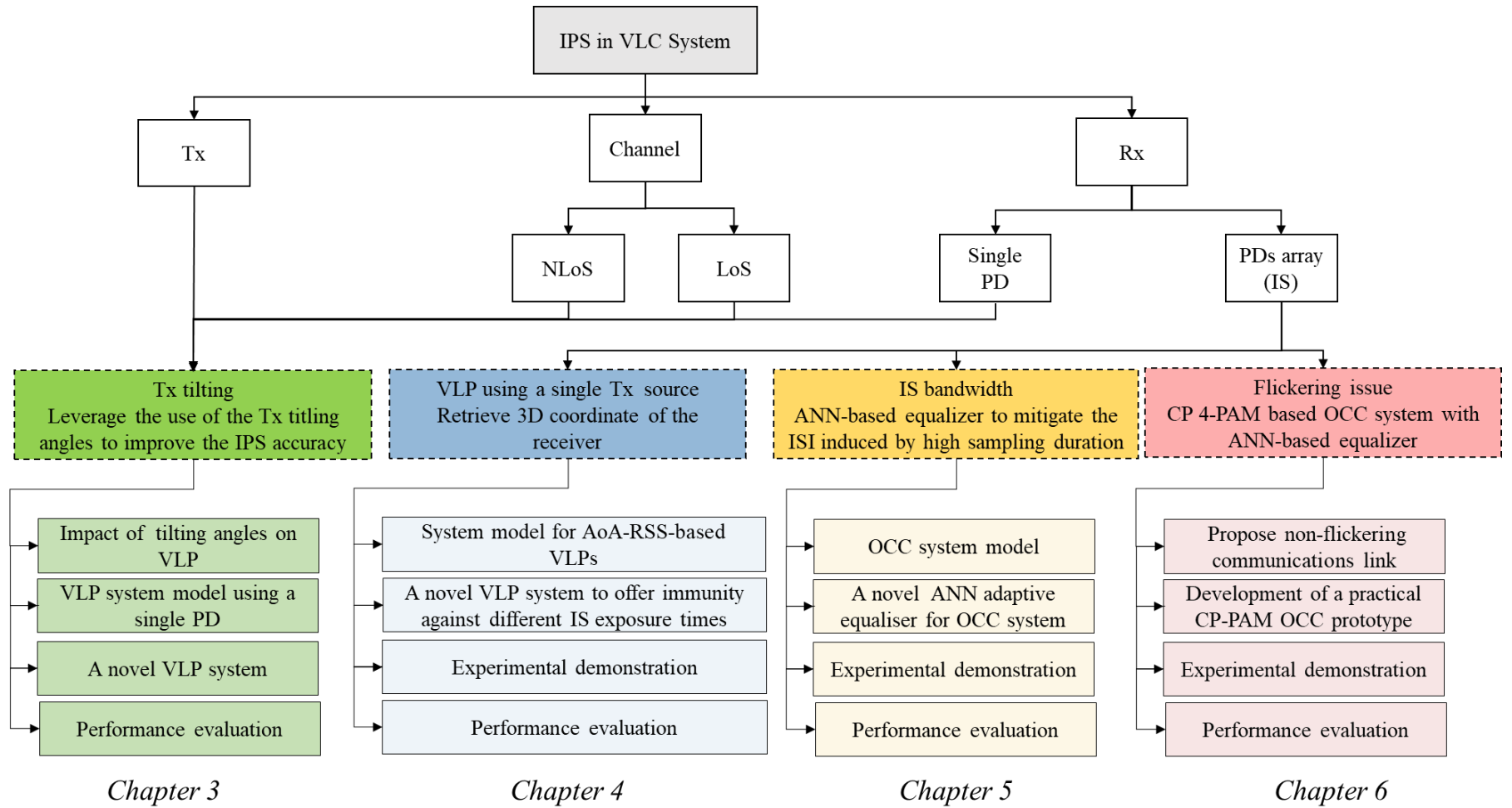


Figure 1-1. Summary of original contributions.

1.5 Thesis Structure

This thesis is organized into seven chapters. Chapter 1 introduces IPS based VLC system, its merits and challenges. The aims, objectives and the original contributions of this research are also presented. Chapter 2 provides an in-depth review of several IPS technologies, with a focus on the application of VLP in the indoor environment. It also includes a thorough examination of major characteristics of VLPs in terms of their complexity, accuracy, and cost of implementation. Chapter 3 presents the first original contribution to knowledge, in which the systematic analysis showed that the accuracy of RSS-based VLP is primarily limited by the tilting angles of both Tx and Rx as well as the multipath reflections. Subsequently, a novel approach was proposed to demonstrate that Tx tilting may improve the VLP accuracy as compared with a conventional non-tilting Tx case, and hence achieve a highly accurate indoor VLP system. In Chapter 4, an overview of the merits/application, as well as the experimental reports on IS based VLPs were outlined where details of utilized technology, the number of Tx and Rx, test conditions and the accuracy achieved so far reported in literature were highlighted. The 2nd contribution of thesis was presented in this chapter, in which a novel technique was also proposed to mitigate the error induced by the lens at the receiving side, hence, leading to reduced positioning errors. The experimental results showed that, the proposed method offers immunity against different exposure times within the standard range of 250 μ s to 4 ms. In Chapter 5, an overview of the OCC link capabilities reported in the literature was initially explored. The standard IS-based Rx was modelled and a trade-off between the gain and the required bandwidth was outlined. Furthermore, a 3rd contribution of the work was done in this chapter, in which a novel OCC system with an ANN adaptive equaliser was proposed to mitigate ISI and therefore increase the data rate. The proposed system is theoretically investigated and experimentally evaluated. In Chapter 6, the last contribution was presented in this chapter, in which an experimental setup was developed to demonstrate non-flickering communications using a single light-emitting diode. An ANN-based equalization technique was proposed for a CP 4-pulse amplitude modulation (PAM) based OCC system. The ability to mitigate the intersymbol interference was demonstrated and hence to transmit a signal with an acceptable BER (below the FEC limit) for unequalized and equalized systems, respectively. The limitation of the proposed system was assessed by the system complexity, including the associative memories

needed for the look-up table training data as well as the IS resolution, gap-time and exposure time, and reading time. Finally, in Chapter 7, conclusions are given and recommendations for future work.

1.6 List of Publications and Awards

This section includes the list of the published work related in chronological order as follows:

1.6.1 Peer Reviewed Journal Papers

1. **O. I. Younus**, N. Chaudhary, Z. Ghassemlooy, N. B. Hassan, L. N. Alves, and S. Zvánovec" A Unilateral 3D Indoor Positioning System Employing Optical Camera Communications," *Opt. Express* [submitted]
2. N. Jiang, B. Lin, Q. Lai, T. Huang, Z. Ghassemlooy, **O. I. Younus**, J. Luo, Y. Xie, L. Dai, and Z. Huang, "Non-line-of-sight WDM-MIMO optical camera communications with the DBPWR algorithm," *Optics Communications*, p. 128371, 2022/04/27/ 2022.
3. N. Chaudhary, **O. I. Younus**, L. N. Alves, Z. Ghassemlooy, and S. Zvanovec, "The Usage of ANN for Regression Analysis in Visible Light Positioning Systems," *Sensors*, vol. 22, no. 8, 2022.
4. N. Chaudhary, **O. I. Younus**, L. N. Alves, Z. Ghassemlooy, S. Zvanovec, and H. Le-Minh, "An Indoor Visible Light Positioning System Using Tilted LEDs with High Accuracy," *Sensors*, vol. 21, no. 3, 2021.
5. E. Eso, Z. Ghassemlooy, S. Zvanovec, J. Sathian, M. M. Abadi, and **O. I. Younus**, "Performance of Vehicular Visible Light Communications under the Effects of Atmospheric Turbulence with Aperture Averaging," *Sensors*, vol. 21, no. 8, 2021.
6. **O. I. Younus**, N. B. Hassan, Z. Ghassemlooy, S. Zvanovec, L. N. Alves, and H. Le-Minh, "The Utilization of Artificial Neural Network Equalizer in Optical Camera Communications," *Sensors*, vol. 21, no. 8, 2021.
7. M. Hulea, Z. Ghassemlooy, S. Rajbhandari, **O. I. Younus**, and A. Barleanu, "Optical Axons for Electro-Optical Neural Networks," *Sensors*, vol. 20, no. 21, p. 6119, 2020.
8. P. Pešek, P. A. Haigh, **O. I. Younus**, P. Chvojka, Z. Ghassemlooy, and S. Zvánovec, "Experimental multi-user VLC system using non-orthogonal multi-band CAP modulation," *Opt. Express*, vol. 28, no. 12, pp. 18241-18250, 2020/06/08 2020.

9. **O. I. Younus**, H. L. Minh, P. T. Dat, N. Yamamoto, A. T. Pham, and Z. Ghassemlooy, "Dynamic Physical-Layer Secured Link in a Mobile MIMO VLC System," *IEEE Photonics Journal*, pp. 1-1, 2020.
10. **O. I. Younus**, N. B. Hassan, Z. Ghassemlooy, P. A. Haigh, S. Zvanovec, L. N. Alves, and H. L. Minh, "Data Rate Enhancement in Optical Camera Communications Using an Artificial Neural Network Equaliser," *IEEE Access*, vol. 8, pp. 42656-42665, 2020.

1.6.2 Peer Reviewed Conference Papers

1. Y. Chen, D. Lymberopoulos, J. Liu, and B. Priyantha, "FM-based indoor localization," in *Proceedings of the 10th international conference on Mobile systems, applications, and services*, 2012, pp. 169-182.
2. S. Lauxtermann, A. Lee, J. Stevens, and A. Joshi, "Comparison of global shutter pixels for CMOS image sensors," in *2007 International Image Sensor Workshop*, 2007, p. 8.
3. X. Li, N. B. Hassan, A. Burton, Z. Ghassemlooy, S. Zvanovec, and R. Perez-Jimenez, "A Simplified Model for the Rolling Shutter Based Camera in Optical Camera Communications," in *2019 15th International Conference on Telecommunications (ConTEL)*, 2019, pp. 1-5.
4. A. Sturniolo, G. Cossu, E. Ciaramella, N. B. Hassan, Z. Shou, Y. Huang, and Z. Ghassemlooy, "ROI Assisted Digital Signal Processing for Rolling Shutter Optical Camera Communications," in *2018 11th International Symposium on Communication Systems, Networks & Digital Signal Processing (CSNDSP)*, 2018, pp. 1-6.
5. T. Nguyen, A. Islam, T. Yamazato, and Y. M. Jang, "Technical Issues on IEEE 802.15.7m Image Sensor Communication Standardization," *IEEE Communications Magazine*, vol. 56, no. 2, pp. 213-218, 2018.
6. W. A. Cahyadi, Y. H. Chung, Z. Ghassemlooy, and N. B. Hassan, "Optical Camera Communications: Principles, Modulations, Potential and Challenges," *Electronics*, vol. 9, no. 9, p. 1339, 2020.
7. Y. Goto, I. Takai, T. Yamazato, H. Okada, T. Fujii, S. Kawahito, S. Arai, T. Yendo, and K. Kamakura, "A New Automotive VLC System Using Optical Communication Image Sensor," *IEEE Photonics Journal*, vol. 8, no. 3, pp. 1-17, 2016.
8. F. Dou, J. Lu, Z. Wang, X. Xiao, J. Bi, and C. H. Huang, "Top-Down Indoor Localization with Wi-Fi Fingerprints Using Deep Q-Network," in *2018 IEEE 15th International Conference on Mobile Ad Hoc and Sensor Systems (MASS)*, 2018, pp. 166-174.
9. S. Zhang, J. Guo, N. Luo, L. Wang, W. Wang, and K. Wen, "Improving Wi-Fi Fingerprint Positioning with a Pose Recognition-Assisted SVM Algorithm," *Remote Sensing*, vol. 11, no. 6, p. 652, 2019.
10. C. Liu, C. Wang, and J. Luo, "Large-Scale Deep Learning Framework on FPGA for Fingerprint-Based Indoor Localization," *IEEE Access*, vol. 8, pp. 65609-65617, 2020.

1.6.3 Posters

11. **O. I. Younus**, Z. Ghassemlooy, P. A. Haigh, S. Zvanovec, L. N. Alves, and H. Le Minh (2019), "Data Rates Enhancement Using an Artificial Neural Network Equaliser in Optical Camera Communications," in *PGCon Edinburgh Postgraduate Conference*, 2019, Edinburgh, United Kingdom.

1.6.4 Invited Keynote Speaker

12. Z. Ghassemlooy, **O. I. Younus**, and N. Chaudhary, "Optical Wireless Communications **for the Access Networks**," in the **26th Optoelectronics and Communications Conference (OECC)**, 2021, Hong Kong. [*The Conference is organized by The Hong Kong Polytechnic University and co-sponsored by the Optical Society of America and IEEE Photonics Society*].

1.6.5 Training School

13. **O. I. Younus**, and N. Chaudhary, "Visible Light Positioning System Modelling," in online platform 2021. [*European Network on Future Generation Optical Wireless Communication Technologies*].
14. S. Teli, V. Matus, and **O. I. Younus**, "Principles of Optical Camera Communications," in online platform 2021. [*European Network on Future Generation Optical Wireless Communication Technologies*].

1.6.6 Awards

- Fully Paid PhD. Research Grant (Northumbria University, 2019)
- Editor's Choice Article (MDPI, 2022)
- Best Poster Presentation of PGCon Postgraduate Conference (Edinburgh University, 2019)
- European Network on Future Generation Optical Wireless Communication Technologies – Research Grant Short Term Scientific Mission-CA19111-48850 (European Cooperation in Science & Technology, 2021)

Chapter 2

Overview of Indoor Positioning Systems

2.1 Introduction

This Chapter provides an overview of various indoor positioning systems IPSs and technologies. IPSs are identified based on the (i) positioning technology, which signifies the method in which the localization information is gathered; and (ii) positioning technique, which describes the way the position is obtained based on the available light information [47]. The chapter presents the advancements in the domain of IPS, and how the current research addresses the gaps in the existing positioning methods to achieve its foremost goal of facilitating the design of a low-cost, accurate and less complex IPS.

2.2 Indoor Positioning System

With the evolution of the IoT, there has been an exponential growth in the production and utilization of smart devices. Examples of this are a sharp increase in the volume of IoT connected devices such as smart light bulbs, connected vehicles, smart home devices, and connected industrial equipment that are more than 16 billion units for 2022. The total installed IoT-based connected devices worldwide is projected to step over 30 billion by 2025 [48], which presented a vast network supporting large devices, different latency requirements, low power consumption, and low costs per unit. Establishing a reliable communication channel between these devices requires prior information about their locations. The use of GPS can facilitate positioning estimation in outdoor environments, but GPS and similar satellite navigation systems have major issues when operating in indoor environments due to the lack of line-of-sight paths to satellites.

IPS, also known as an indoor localization system, is seen as an essential technology to enable location-based services in numerous applications including location tracking, navigation, ITs, shelf-level advertising in supermarkets and shopping malls, robot movement control, manufacturing, medical surveillance, etc [49]–[51]. The positioning systems can be used in both indoor and outdoor settings. In indoor environments, there is

a range of positioning systems that could be utilised to ensure availability and the quality of service [52].

Although the classification of the positioning systems presented is based on techniques/technologies/topologies, other classifications and taxonomies are also used. For instance, in [53], the authors classified the IPSs into (i) device-based systems, in which the tracked entities have a specific device used for localization purposes; and (ii) device-free systems, where the infrastructure can provide the localization services without any hardware on the tracking targets. An example of such a system is a vision-based IPS that identifies the presence of humans in an indoor scenario. This classification is also known as active vs. passive placement [54]. Further classification distinguish IPSs in terms of the infrastructure-based or infrastructure-free systems [55]. The former involves the installation of specific Tx's or other infrastructure, whilst the latter does not require any changes to the indoor environment. Compared to the infrastructure-free systems, which offer a low installation cost, the interest in infrastructure-based solutions have substantially increased since they provide greater accuracy and robustness. An IPS that uses the earth's magnetic field to identify the users' position is an example of an infrastructure-free system. Lastly, due to the increased use of smartphone-friendly technology, in [56], the authors distinguished IPSs based on the smartphones compatibilities.

The general overview of technologies utilized in IPS is discussed in the following section, in which a brief introduction outlining the main characteristics, advantages and drawbacks of each category is highlighted.

2.3 Indoor Positioning Technologies

The necessity for indoor location-based services has been growing over the past decades because of its significance in the development of various applications, such as smart home appliances, robots, supermarkets, shopping malls, hospitals, etc. IPS with high precision and low cost has become one of the most exciting features of next-generation indoor optical wireless communication systems [57]. The deployment of IPS may differentiate based on the technology that is used to obtain the information related to localization. This classification is used most often in literature to differentiate between IPS.

Various conventional indoor positioning technologies are based on RF technologies [1], [2], for instance, wireless local area network [6], Wi-Fi [58], ultrasound [5], [59], radio frequency identification (RFID) [8], [9], ultra-wideband (UWB) [6], [7], Bluetooth [3], [4], amongst others. The low frequencies RF-based approaches suffer from the influence of reflections, which may severely affect positioning accuracy (PA) [60]. Likewise, the accuracy of IPSs using RF technologies with low frequencies is relatively low. For instance, existing localization research proved its ability to provide a degree of accuracy measured in meters using different technologies such as geo-magnetism [10], Wi-Fi [11], and FM broadcast technology [12]. Note that, RF signals suffer from additional interference due to the high penetration rate of the RF compared with light-based signals.

OWC-based IPS have been introduced in recent years, which have shown great potential in achieving high-precision indoor positioning due to the use of optical signals (i.e., infra-red, ultraviolet, and visible light). The electromagnetic spectrum is shown in Figure 2-1, in which, the optical spectrum is three orders of magnitude larger than the entire RF spectrum [61].

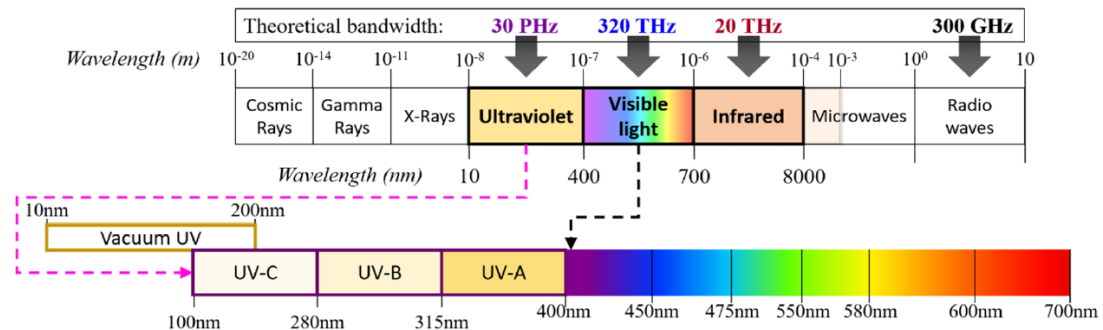


Figure 2-1. The entire electromagnetic spectrum. The combined infrared and visible light spectra are 2600 times larger than the entire RF spectrum [62].

Note, at low levels, all light sources are harmless to humans and depending on the wavelength have different use in many applications [63]. Remarkably, even though IR technology is rather a niche, their implementations vary widely. IR signals are used mainly to provide positioning services [64]. For instance, active beacon systems have fixed infrared Rx or Tx placed at known locations in indoor environments, and mobile Tx or Rx whose positions are unknown. IR pulses sent from the Tx are used to determine the location of the mobile nodes. An example of this technology is the HTC VIVE [65], a virtual reality system that uses two infrared base stations to determine the 6 degrees of freedom position of the headset and the controller. Another example is Microsoft Kinect, which uses a continuously projected IR structured light to detect the environment with an infrared camera [66].

Alternatively, visible light-based IPS, known as a VLP, has attracted significant attention over the past decade [14]. In VLP, the LEDs-based lighting infrastructures are utilized for positioning in addition to illumination and data communications, hence considered an energy efficient and low cost solution compared to other technologies reported previously [39][40]. In addition, VLP offers inherent security at the physical layer since lights emitted from the sources and reflected surfaces are maintained within a confined space.

VLP can be used in numerous applications including location tracking, navigation, ITS, shelf-label advertising in supermarkets and shopping malls, robot movement control, manufacturing, medical surveillance, street advertising, etc. [50], [51], [60]. In indoor VLP systems, LEDs are used as Tx, and a PD, or an array of PDs in the form of a single IS are used as the Rx. Table 2.1 summarises the existing positioning technologies along with their advantages and drawbacks.

Table 2.1 Comparison of existing IPS technologies

Ref.	IPS technologies	Accuracy (m)	Advantages	Constraints	Re-use of existing infrastructure
[15], [68]	GPS	6-20	Complete earth coverage	Suitable for outdoor only, requires expensive infrastructure	Yes
[69], [70]	Wi-Fi	1-5	Re-use of existing infrastructure	Highly environment dependant when fingerprinting method is employed, involves high deployment cost for building database	Yes
[71], [72]	Bluetooth	1-5	Low cost, low power consumption	Limited coverage range, low accuracy, susceptible to noise, limited user mobility	No
[73], [74] [7]	UWB and Ultrasound	0.1-1	Good positioning accuracy, immune to interference	Expensive, limited coverage range	No
[75], [76]	RFID	1-2	Low power consumption, wide coverage range	High response time, low accuracy, limited user mobility	No
[77], [78]	Infrared	1-2	low power consumption	Short-range and requires special IR LEDs	No
[79], [80]	VLC	0.01-0.35	Low cost, high accuracy, allows dual usage of LEDs	Need to modify the existing infrastructure for the dual purposes, range might be affected by obstacles	Yes

2.4 VLC-based-IPs Techniques

Various wireless technologies were explored in the previous section, in which VLC-based IPs have shown the capability to provide high accuracy with low implementation costs. However, these factors may vary depending on the state-of-the-art of proposed VLC-based-IPs. This section introduces a taxonomy to evaluate the VLC IPs based on the research works reported in the literature. Various localization techniques are studied and analyzed based on their common characteristics. The VLC IPs are categorized based on three key characteristics: mathematical, sensor-assisted, and positioning optimization methods. Three distinctive categories of fingerprinting, range-free and range-based methods are grouped into a mathematical approach based on the VLP class. The detailed descriptions of the VLP techniques and the background studies are outlined in the following subsections. The sensor-assisted technique highlights the VLC-based-IPs works done with the aid of additional sensors. Here, the image sensor and sensor fusion categories are discussed. The positioning optimization methods are then introduced in the following subsection.

2.4.1 Mathematical Method

2.4.1.1 Fingerprinting Technique

The fingerprinting approach, also known as scene analysis, relies on a distinct feature or characteristic of signals to estimate the position of the Rx. It correlates the real-time measurement data to fingerprints of pre-measured signal properties at all points in a confined indoor environment. The signal characteristics leverage the use of all available positioning techniques stated previously, such as AoA, ToA, time difference of arrival (TDoA), and RSS [14]. Because of its simplicity, RSS-based fingerprinting is the most widely used fingerprinting technology. However, the existence of diffraction and reflection might substantially impact the accuracy of the VLP system. Typical fingerprinting methods can be categorized into a radio-map and map-free based localization. The map-based fingerprint localization consists of two stages, the offline training stage, in which the database is generated based on pre-measured signal characteristics, and the online stage, where the real-time position is estimated based on the comparison between the measured values at an unknown position with the pre-

measured values. The accuracy of this approach is mainly dependent on the utilised signal characteristics [20].

Numerous studies that employ fingerprint technology in VLP systems were introduced. For instance, in [81] the information signal with a unique address was transmitted via the LED-based Tx, whereas the NRZ- on-off keying (OOK) modulation technique was used for data communication. The fingerprint and combination of correlation values techniques were applied to estimate the position based on the RSS information. An accuracy of 4.38 cm for the mean distance error was achieved among 36 points with dimensions of $1 \times 1 \times 1.2 \text{ m}^3$. Moreover, an iterative ML approach for positioning systems based on RSS measurements was proposed in [82]. Using the proposed system; mean square error (MSE) performance similar to that of Cramer-Rao bound could be obtained at the cost of higher complexity (i.e., the longer time and higher computational analysis). In [83], a self-localization technique was deployed to attain high robustness VLP system. A Bayesian signal model was utilized, and LEDs were detected using the proposed inherent sparsity to deliver a fully autonomous system. A probabilistic model was used to estimate the position and an approximate accuracy of 0.81 cm were achieved. Furthermore, the LED-based Txs were modulated in different frequencies in [84], and the received power spectral density was detected and utilised to create the fingerprinting map at the Rx side. The simulation and experimental results showed that the proposed system could achieve an accuracy of 15-20 cm.

Similarly, a LAT (localization, access and transmission) indoor multiple-input multiple-output (MIMO)-VLC system was introduced in [85], which consisted of (i) RSS measurements to build the fingerprinting database for positioning; (ii) MIMO system for adaptive pulse position modulation to provide higher data rates; and (iii) time division multiple access for VLC accesses links. The proposed system was simulated and experimentally established in an open office with a dimension of $10 \times 9 \times 3 \text{ m}^3$. Furthermore, [86] introduced a VLP system that utilizes a correlation approach to match the pre-estimated address for each LED light with the detected signals at the Rx. The experiment was conducted in an indoor environment with dimensions of $30 \times 30 \times 50 \text{ cm}^3$, and positioning error ε_p of 1.495 and 0.651 cm were evidenced for the maximum and mean values, respectively.

In [87], and [88], time division multiplexing (TDM) was deployed to mitigate the impact of interferences that occurred at the transmitted signals, and an average ε_p of 1.68

cm was obtained for the proposed systems. A fingerprint-based VLP system has also been investigated for indoor environment, in which an infrared LED was used to localize the Rx position. A map-based fingerprinting was used by exploiting the Tx characteristics, including the impulse responses and the uniform deployment of LED-based TxS [89].

Furthermore, the recent advent of machine learning (ML) technology has resulted in increased localization performance using the fingerprinting method. In [22]–[24], the authors showed an ML-based RSSI fingerprinting with a few centimetres of precision and decreased latency at the cost of increased system complexity.

Likewise, The VLC-based positioning using fingerprint technology and the image sensor was introduced in [90]–[95], and the obtained accuracies were reported in Table 2.2. The performance of the fingerprint-based VLP systems is highlighted in Table 2.2, in which the system metrics are evaluated in terms of cost, complexity, significant features, and accuracy.

Table 2.2 Comparison of existing fingerprinting based VLP.

Ref.	Algorithm	ε_p (cm)		Test condition(m)	Cost	Complexity	Note
		Experimental	Simulation		(L: Low, M: Medium, H: High)		
[81]	Fingerprint	< 5		$1 \times 1 \times 1.2$	L	L	-
[82]		-	< 10	$6 \times 6 \times 4$	L	M	-
[83]		-		$30 \times 30 \times 0.25$	L	L	-
[84]		15-20		$1.8 \times 1.2 \times 1$	L	M	-
[85]		-	1-2	$10 \times 9 \times 3$	M	M	PPM technique
[89]		-	20-80	$10 \times 9 \times 3.1$	L	L	Infrared LED
[86]		-	< 10	$0.3 \times 0.3 \times 0.5$	L	L	
[87]		-	1.69	$0.9 \times 0.9 \times 1.5$	L	M	TDM scheme
[88]		< 5		$0.6 \times 0.6 \times 1$	L	L	
[90]		-	7	-	L	L	Image sensor
[91]		5		$1.5 \times 1.5 \times 1.95$	L	M	Image sensor
[96]		-	<10	$1.8 \times 1.8 \times 3.5$	M	M	Two image sensors
[93]		-	85	$2 \times 2 \times 2.7$	M	M	Two image sensors
[94]		-	<10	-	L	M	
[95]		-		-	M	M	Two image sensors, and extended kalman filter

2.4.1.2 Range-free Technique

Range-free solutions (also known as proximity-based or coverage solutions) deliver semantic location information (i.e., identify the position based on the range of a recognised station or a nearby reference). The simplicity of range-free techniques is their major advantage. However, the precision is limited by the amount of Tx reference nodes available and the configuration of lighting fixtures [15], [20]. The positioning accuracy can be enhanced by increasing the number of deployed Tx anchors, which may impose additional system costs [97]. As a result, range-free positioning is best suited for less demanding applications (e.g., to display location-specific content in a museum). Various investigations were performed on range-free based VLP systems [98]–[104]. For example, a VLP preliminary design and implementation were done in [100], in which the system comprises of a mobile phone and LED lights, which consistently transmit its ID or coordinates, allowing the mobile phone to calculate the precise location using the data received. Both passive and active beacons were investigated, and the demonstrated error-free range was up to 4.5 m. Furthermore, a range-free based VLP was experimentally investigated in [98], in which a frequency-shift-keying modulation scheme was used to transmit the unique positions of up to 29 Tx sources. The relative Rx position was assigned to the region where the Tx is situated.

In [99], a VLP system was proposed to mainly provide a solution to visually impaired individuals, in which the accurate position and travel directions were estimated using LED light sources and a geomagnetic sensor. An approximate positioning error ε_p of 1-2 m was obtained without considering the azimuth accuracy. In [101], a hybrid system that combines VLC and ad-hoc wireless network architecture was investigated. Non-carrier and 4 MHz carrier VLC-based hybrid designs were demonstrated in two configurations for the proposed VLP system. The recorded error-free communication range for a low data rate situation was between 33-40 cm. However, an approximate range between 0.57-47.9 cm was deployed in a high data rate and wide-range reception situation.

Moreover, the accuracy of a system that employs VLC plus a 6-axis sensor (geomagnetic and gravity acceleration sensors) is greater than that of a basic VLC-based positioning system [102]. It shows that more than 30% improvement can be achieved using a switching estimated receiver position (SERP) technique. In [103], the rotation matrix and support vector machines (SVMs) were utilized to determine the precise field of view (FOV) limit as well as the potential azimuth and tilt angulations. Thus, this model

could save at least 80% of computations compared with conventional geometric optics calculations. Alternatively, a long-range VLP solution was described in [104], in which a hybrid system combines a five-hop ZigBee wireless network with VLC to provide positioning. The proposed system provides minimal power consumption, robust security, and a large coverage area. Table 2.3 summarises the performance work implemented on the range-free-based VLP systems.

Table 2.3 Comparison of existing rang-free based VLPs.

Ref.	Algorithm	\mathcal{E}_p (cm)		Test condition(m)	Cost	Complexity	Note
		Experimental	Simulation		(L: Low, M: Medium, H: High)		
[98]	Range-free	< 200		$8 \times 3.88 \times 1.2$	L	L	binary frequency shift keying modulation scheme
[99]		100-200		A walk of distance 50 m and a height of 2.7 m	L	L	Voice navigation for visually impaired individuals
[100]		450		-	L	L	
[101]		< 480		$1.8 \times 1.2 \times 1$	M	M	Hybrid system VLC and ad-hoc wireless system
[102]		-	30-60	$10 \times 9 \times 3$	L	L	6-axes sensor and SERP technique
[103]		-	30-60	$10 \times 9 \times 3.1$	L	L	rotation matrix and Support Vector Machines
[104]		-	40	$0.3 \times 0.3 \times 0.5$	M	M	Hybrid system VLC and ZigBee wireless network

2.4.1.3 Range-based Technique

In comparison to range-free approaches, the geometrical properties of circles, spheres or triangles are employed to estimate the Rx position. It may require a pre-knowledge about the direct (shortest LOS) path for the transmitted signal, which can be obtained either through lateration, which relies on distance measurements between the known reference points (fixed lights, also known as landmarks) and the unknown position, or angulation, which locates the position based on the angle of the information arrival with respect to the reference point. The lateration approach requires a minimum of three non-collinear reference points that are measured using a PD or an IS to locate the 2D Rx position. The distance information from light landmarks can be calculated using different measurements such as the ToA, TDoA [18], RSS [19], and direct detection [97], [105], and ϵ_p of 10 to 40 cm could be achieved using these methods [20]. The implementation detail of each approach is presented subsequently.

I. AoA

AoA-based VLP systems determine the angle of arrival of the received signals, and the position is measured using geometrical relationships by intersecting several directions of wireless received signals from different stations [106]. It is also noted that at least two reference stations are required to establish the AoA technique. AoA is not utilized widely in radio-based systems that are not usually reliant to LoS, such as Wi-Fi and Bluetooth. However, this is not the case in VLP systems wherein the direct light of sight carries a significant amount of transmitted power. Although AoA is susceptible to the external environment and has a lower accuracy than ToA, it does not require any time synchronization between the Tx and the Rx. Furthermore, there is no need to consider path loss and disturbance from background illumination sources reflected components for image transformation approaches [107]–[118]. Next, AoA-based VLP was referenced in various studies, see Table 2.4. For instance, [114] demonstrated a high-precision system based on AoA with an accuracy of 10 cm. Likewise, [119] adopted AoA for wearables devices, in which a flicker-free with polarization-based modulation was deployed, and the results show an accuracy of < 40 cm can be obtained using smartphones and Google Glass.

Besides, a light sensor and accelerometer were deployed to estimate the position of the Rx [120] [121]. The intensity of the received light, as well as the Rx orientation, were measured in both works and the experimental demonstration showed that the system is capable of achieving an accuracy of 0.5 cm. Similarly, [122] presented a truncated weighting approach for an AoA-based VLP system, with simulation results indicating that truncated weighting can outperform traditional VLP methods and achieve an accuracy of 5-30 cm. Furthermore, the AoA-based VLP system was introduced in [123], in which the authors derived Cramer-Rao bound (CRB) mathematical bounds and showed that, with a simulation accuracy of 8 cm could be achieved. To achieve differential photocurrent detection of the incident light AoA, the system [106] demonstrated that the RSS approach had a four times higher accuracy than AoA, which may reach 5 cm by employing three PDs at the Rx. The authors also stated that systematic errors, angular precision, and geometry are the main factors that may impact the accuracy of AoA-based VLP systems.

Table 2.4 Comparison of existing AoA range-based VLPs.

Ref.	Algorithm	ε_p (cm)		Test condition(m)	Cost	Complexity	Note
		Experimental	Simulation		(L: Low, M: Medium, H: High)		
[121]	AoA	50	-	$5 \times 3 \times 3$	M	M	Accelerometer
[124]		-	< 15	4×6	L	L	-
[125]		29.8		$5 \times 1 \times 1.5$	L	M	Inertial sensor
[126]		-	13.95	$4 \times 4 \times 3.5$	L	M	Inertial sensor
[127]		8.2 mm		$8 \times 8 \times 0.4$	H	M	Aspherical lens on LED
[128]		-	12.9	$5 \times 3 \times 3$	H	M	Biconvex Lens on LED
[129]		100-200		4×6	M	M	Data rate between 300-400Mb/s
[114]		~10	-	$0.71 \times 0.73 \times 2.46$	M	M	Uses roller shutter effect of image sensor
[119]		< 40	-	$2.4 \times 1.8 \times 3$	M	M	
[120]		25	-	$5 \times 3 \times 3$	M	M	Accelerometer
[122]		-	5-30	$5 \times 3 \times 3$	H	H	Truncated-weight method
[130]		10		-	H	H	-
[123]		-	8	$- \times - \times 1-3$	H	H	-
[106]		-	5	-	M	M	-

II. ToA and TDoA

Time of arrival is the most popular ranging technique utilized mainly in the GPS [68]. This approach relies on knowing the signal propagation time t_p (i.e., the precise time for the signal to travel from a reference location to the target position) and the signal's speed (typically the speed of light c). Hence, the distance is computed as $c \times t_p$, and the set of possible location is determined using the trilateration method. ToA requires few references points (at least three for two-dimensional (2D) or at least four for 3D) and exact synchronization between the Tx and the Rx to estimate the position [131], [132]. The theoretical boundaries of the ToA-based VLP system were investigated in [133], [134], a Cramer-Rao bound was derived based on various factors that consist of a perfect synchronization based on the geometrical room dimensions, the power and frequency of the propagated signal, and the characteristics of both Tx's (i.e., LEDs) and the Rx (i.e., a PD). The evaluation showed that an average ε_p ranging between 2 and 6 cm could be achieved [89] [135]. Likewise, the ToA based VLP approach was developed in [134]. The Tx and the Rx were assumed to be perfectly synchronized, and white LEDs were employed for illumination and signal transmission at the Tx side. The emitted signals were captured at the Rx, and the range was determined based on the ToA signal measurements. Thus, ε_p of 5 cm was demonstrated for the proposed system.

Alternatively, the TDoA method was proposed to overcome the need for time-critical synchronization between the reference points and target, yet it still requires time synchronization between the reference points involved in positioning [136], [137]. Like the ToA, the estimated time is converted into the distance by multiplying the speed of propagation. In [138], the use of TDoA based VLP system was proposed, in which the use of TDoA and phase difference algorithms were deployed for localization purposes. The VLP system performance was evaluated by computer simulation, and indoor location accuracy of ≤ 1 cm was obtained in a room dimension of $5 \times 5 \times 3$ m³. Moreover, the use of the intensity modulation/ direct detection (IM/DD) and subcarrier BPSK schemes for optical signal modulation was investigated in [139]. The TDOA and nonlinear recursive least square algorithm were deployed to estimate the Rx position. Similarly, mathematical modelling of a VLP system was introduced in [140]. The received signal was assumed to be contaminated with Gaussian noise, and the TDOA based position estimation process involved three steps: distance estimation, position estimation, and error minimization.

Similarly, a measurement scheme based on a TDoA technique employing a dual optical-ultrasound system was adopted in [59]. The proposed system utilised the same principle as the cricket technology with a few modifications to provide distance estimation between both the base station and mobile node at the same time. The results reveal that both base station and mobile node devices can determine distance with equal precision (around 2% error).

The VLP system was simulated using Matlab[®], and ε_p was minimized using the two-step approximate maximum likelihood algorithm. Hence, an accuracy of ≤ 2 cm was obtained in the room space of $5 \times 5 \times 3$ m³. Table 2.5 summarises the existing ToA or TDoA range-based VLPs.

Table 2.5 Comparison of existing ToA or TDoA range-based VLPs.

Ref.	Algorithm	ε_p (cm)		Test condition(m)	Cost	Complexity	Note
		Experimental	Simulation		(L: Low, M: Medium, H: High)		
[141]	ToA or TDoA		2-5	- × - × 2.5	H	H	
[138]			1	5 × 5 × 3	M	H	
[136]			3.9	5 × 5 × 3	L	M	No ID information was transmitted through the pilot signal
[139]			< 30	-	M	M	
[140]			2	-× -×3	H	H	KF and Maximum Likelihood were compared with the conventional system

III. RSS

RSS-based trilateration is widely utilized in VLPs, which requires a minimum of three lighting sources to estimate the Rx position. It relies on the propagation loss measurements of the emitted signal based on the received signal strength. The range can be estimated using a standardized path loss model [15]. The implementation of RSS-based systems is also simpler compared with ToA and AoA-based positioning systems since (i) they do not require highly accurate transceiver synchronization or an Rx with efficient detection of the incidence angle [142]; and (ii) it may deliver a relatively good positioning accuracy due to the availability of LoS channels for most indoor environments. Table 2.6 shows most of the previous studies have been focused on RSS-based VLP systems [67], [143]–[146], where the strength of the received power P_r is used to estimate the Rx's position [19].

Although designing an RSS-based IPS using this technique is relatively simple, there are still several challenges to be addressed when designing this system in an indoor environment. For instance, the concurrent transmission of the optical signals using multiple light sources (i.e., LEDs) may introduce complexity to recover the signals using a single PD-based Rx [147]. Different modulation techniques have been investigated. For instance, an orthogonal frequency division multiplexing (OFDM) VLP system was proposed to mitigate the multipath effects [147], in which the performance of the IM/DD as a single-carrier modulation and OFDM as a multi-carrier modulation scheme were evaluated. The results show that increasing the number of subcarriers enhances positioning performance at the cost of greater complexity and a higher peak-to-average power ratio (PAPR).

In [148], the impact of subcarrier numbers on the VLP system was investigated, in which Cramer–Rao bound analysis was utilized to assess the theoretical accuracy of the VLP system. The theoretical analysis demonstrated that the estimated accuracy of triangular LED array's is higher than the square array, and the simulated VLP system may achieve a precision accuracy of 4.78 cm. Likewise, a state estimation model was employed to study the user mobility and dynamic device orientation on the VLP system [149]. A Kalman filter (KF) recursive estimation was utilized, and the results reveal that an approximate ε_p of 5 cm can be achieved.

Alternatively, the multipath impact on the RSS-based VLP system was investigated in [150],[151],[152],[153]. A Gaussian mixture sigma-point particle filter (GM-

SPPF) was used at the Rx side to reduce ε_p [150]. Similarly, the combined deterministic and modified Monte Carlo techniques (CDMMC) were deployed to estimate the impulse response and a system accuracy of 55 cm was recorded [151]. Furthermore, OOK modulation and CDMMC methods were proposed in [152], in which the authors show that an accuracy of 80.64 cm can be obtained. Likewise, the impact of diffuse light reflection on the RSSI-based VLP system performance was investigated [153]. The proposed system was simulated using LoS and NLoS with three bounces communication channel. It shows that the diffuse reflection significantly impacts ε_p , in which ε_p of ≥ 1.46 m and 30 cm were recorded in high and low reflectivity surfaces conditions, respectively.

Another issue identified in the RSS-based VLP system is that the Rx and the Tx are often assumed to be positioned in parallel (i.e., with no tilting angle), which may increase the ε_p [154]. Various studies were conducted to overcome this challenge by combining additional information about the Rx with the trilateration approach using an auxiliary sensor, such as an accelerometer, gyroscope, or magnetometer. In [121], an accelerometer to determine the Rx orientation with an RSS-based VLP system was utilized to enhance the positioning accuracy. The irradiance angles of Tx's (i.e., LEDs) was assumed to differ from the incidence angle at the Rx, and the results demonstrated that an average ε_p of ≤ 0.25 m can be achieved using three Tx's, an accelerometer, and a single Rx. Similarly, multiple optical receivers and an accelerometer were used to establish a VLP system that supports user mobility. The experimental results show that mean ε_p of ≤ 6 cm was achieved for a mobile Rx with an average speed of 1.3 m/s [155]. Likewise, a performance analysis of a VLP system was simulated when the Rx is tilted in [156], and the results show that the error induced by the Rx tilting can be compensated using a gyroscope and a weighting factor algorithm to minimize the ε_p .

Table 2.6 Comparison of existing RSS range-based VLPs.

Ref.	Algorithm	\mathcal{E}_p (cm)		Test condition(m)	Cost	Complexity	Note
		Experimental	Simulation		(L: Low, M: Medium, H: High)		
[157]	RSS	2.4	-	$- \times - \times 2.5$	L	M	-
[158]		40	-	$5 \times 5 \times 3$	L	M	-
[159]		-	5.9	$5 \times 5 \times 3$	L	M	-
[149]		-	5	-	M	M	KF
[153]		-	30	$- \times - \times 3$	H	H	-
[150]		9	-	$6 \times 6 \times 4.2$	M	L	-
[151]		-	<90	$8 \times 8 \times 3.5$	L	L	Examine the multipath reflections
[160]		6	-	$0.6 \times 0.6 \times 0.6$	M	M	
[156]		1.66	0.74	$1 \times 1 \times 1$	L	L	Rx tilting compensation
[161]		0.05 -0.73	-	$3 \times 3 \times 3$	L	M	OOK

2.4.2 Sensor-Assisted Method

2.4.2.1 Image Positioning Camera-based VLC IPS

The use of an IS-based VLPs is usually dependent on the use of image processing to find the required position, which will require large processing resources. Advances in optical systems have triggered image-based positioning methods to become an attractive solution for indoor navigation systems. In which, the camera can either utilize its received optical reflectiveness characteristics of the obtained scenes (measurements of visual features) or to receive the transmitted coordinates of LEDs by means of OCCs. Moreover, from the received information, it is possible to estimate distances between LEDs and the camera, and so, the position of the camera [21]. The wide usage of the camera in modern handheld devices, (i.e., the IS), allows utilization in IPS. The IS-based VLPs offers many unique features compared to single PD-based systems, such as a larger FOV and the light's spatial and wavelength separation [162]. It captures the image of the light beacons in a periodic way and processes them in a positioning application in order to evaluate the location of the receiver. The information of the light beacons in the image is provided based on the image coordinates.

In a real-world environment, the complexity of the system can crucially impact the positioning accuracy and the cost of the system. Table 2.7 presents the recent works reported in IS-based VLP. For example, in [163], a distance estimation technique was implemented using photography and IS-based communication (i.e., OCC), in which average estimation ε_p of 10 cm using 3-Txs was reported. Likewise, 4-LED and IS were used at the Tx - to transmit location information simultaneously using multiple frequency-shift keying - and the Rx, respectively, with a maximum ε_p of 2 cm at a linkspan of 100 cm [164]. In [165], a hybrid IS-based VLP and pedestrian dead reckoning for indoor application was proposed. The experimental results showed that, the proposed scheme could achieve both cell recognition and three-dimensional (3D) positioning by capturing an image of a single Tx (i.e., LED) with the 2D and 3D average ε_p values of 2.46 and 13.4 cm, respectively. In [166], a VLP system with a single LED lamp and the commercial mobile phone-based Rx was investigated. A LED-based Tx detection algorithm was proposed for identifying the edge of the light source based on brightness weakening, Sobel operator, and the least-square error (LSE) fitting. The experimental results revealed confirmed ε_p of a few cm for different Rx orientations.

In most of the works reported in the literature studies, either multiple LEDs have been used for positioning or an additional sensor has been employed to obtain the position, see Table 2.7.

However, in most scenarios, the narrow FoV of the front-facing camera in smartphones restricts the number of Tx's being captured at the IS, thus making bilateration or trilateration impractical. In addition, unilateration allows less complex and low-cost implementation of the VLC system. Also, the deployment of more LEDs will certainly add some constraints to the implementation of VLP. Therefore, to overcome these issues, different technologies were investigated in [165], [167]–[170]. For example, in [169] a VLP system using a single LED-based Tx and an IS was reported, where the AoA of the transmitted light was determined using the IS and the projection model of the lens. The IS acts simultaneously as a PD for measuring the RSS. Both measurements were utilised as the fingerprint to estimate the Rx's position. The k nearest neighbours in the feature space algorithm were deployed to achieve a more accurate coordinate estimation of the Rx at the cost of increased complexity. The preliminary experimental results showed that, the proposed positioning scheme achieved a high precision where the 95th percentile accuracy was 1.97 cm. Likewise, both AoA and RSS were used in indoor VLP in [170], which was based on a particular frame reception technique designated as the bokeh effect. The system was set intentionally to generate a frame in an out-of-focus condition, thus, avoiding optical power saturation by spreading P_r to the adjacent pixels. The experimental results showed ϵ_p of < 10 cm.

2.4.2.2 Sensor Fusion

It is the process in which multiple types of sensors are merged to improve the system's performance. The evolution of the sensor market is growing significantly, with smart sensors being leveraged across industries, thanks to the Internet of Things, the digitalization of manufacturing, also known as Industry 4.0, and ever-increasing digital transformation efforts in all areas of the economy and society. For instance, magnetic compass, gyroscopes, accelerometers, and various other sensors can be incorporated into intelligent and portable devices and deployed for location and orientation estimation. For example, the use of an IMU sensor with OCC was reported in [165], [167], [168] with ϵ_p of several centimeters. In [171], a VLP method uses a single LED luminaire and a commercial off-the-shelf smartphone camera as the Tx and the Rx, respectively. Note,

the inertial measurement unit (IMU) and the IS were deployed for localization purposes, whereas projective geometry was used to calibrate the orientation measurements. The experimental results showed that an average ϵ_p of 11.2 cm was achieved. Furthermore, in [172], the visible light, IS, and IMU were fused simultaneously to provide VLPs with high accuracy. The proposed strategy showed that the average accuracy achieved was 2.1 cm for stationary localization and the average computational time was around 33 ms.

Table 2.7 Listed studies of sensor-assisted based VLPs.

Ref.	Algorithm	ε_p (cm)		Test condition(m)	Cost	Complexity	Note
		Experimental	Simulation		(L: Low, M: Medium, H: High)		
[163]	Sensor-Assisted Method	10	-	- × - × 2	L	M	OCC
[164]		2	-	- × - × 2.6	M	H	Rolling shutter and multiple frequency-shift keying
[165]		-	decimetre-level	14× 1.6 × 2.3	M	H	IMU, and pedestrian dead reckoning algorithm
[169]		1.97	-	0.7× 0.3× 0.2	H	H	Both AoA and the RSS with k nearest neighbours in feature space algorithm
[170]		<10	-	1 × 1× 2.4	H	H	AoA and RSS with a geomagnetic field sensor and an accelerometer
[166]		Average 2D/3D were 3.17/4.45	-	- × - × 1.2	M	H	Rolling shutter and piecewise fitting. LED
[171]		16	-	1.8 × 1.8 × 2	L	M	IMU
[173]		7.5	-	- × - × 2.8	M	M	OOK modulation scheme was used for ID transmission
[167]		5.44	-	2.7× 1.8× 1.8	M	M	IMU and a plane intersection-line scheme

2.4.3 Positioning Optimization Method

Previous research have shown that mathematical and sensor-assisted approaches can assist VLPs deployment with varying degrees of accuracy, cost, and complexity. Instead, the researchers are still exploring new methods to enhance VLPs performance. Various supplementary methodologies or positioning environments have been developed.

2.4.3.1 Machine Learning Techniques

The use of machine learning in RSS-based VLP systems has been explored in [174]. The authors proposed the usage of K-Means clustering algorithm to achieve a 0.31 m of PA for a room of dimension $4.3 \times 4 \times 4$ m³. Moreover, a PA of 3.65 cm along with a height tolerance of 15 cm was achieved using a backpropagation algorithm -for an indoor VLP system in [175]. Additionally, an innovative solution was proposed for indoor positioning based on the dual-function machine learning algorithms that contain machine learning classification and machine learning regression functions. in [176]. Classification algorithms, such as random forest and support vector machines (SVM), were used to obtain the highest PA of 8.6 and 10.2 cm, respectively. The results showed that, SVM is the optimal solution for VLP systems with a low ε_p .

An ANN has been utilized in RSS-based positioning systems. In [177], both RSS and ANN methods were proposed to achieve an accurate indoor VLP system with a diffuse optical channel. An accuracy of 6.4 cm was achieved with the averaged ε_p being ~ 13 times smaller than RSS-based positioning system. In addition, a low-cost indoor VLP system was proposed using a machine learning algorithm in [9], which was achieved ε_p of 3.7 cm with a height tolerance of 15 cm in LoS environment. In [178], a new 2-D ANN-based VLP system was proposed, where the LEDs were grouped into blocks, and the block coordinates were encoded using under-sampled modulation. A camera was used as an Rx to decode the block coordinate, and the system achieved a mean ε_p of 1.5 cm in LoS channel. In [33], a VLP system based on the RSS and a deep ANN-based Bayesian regularization VLP system was proposed, where only the LoS transmission was considered). The results showed that, using only 20 training points a minimum ε_p of 3.4 cm was achieved. In [32], an ANN-based approach was proposed exploiting the distortions caused by inaccurate modelling (i.e., phase and intensity models) in both phase difference of arrival (PDOA) and RSS-based positioning systems. The pre-trained models

were applied to the ANN-based VLP system for reduced complexity and enhanced robustness, showing an ε_p of 12 cm in an indoor LoS channel.

2.4.3.2 Filtering Techniques

Filtering techniques are also explored in VLPs, mainly divided into two classes: Kalman or Extended Kalman filter (KF or EKF) and particle filter (PF). [95] proposes an LED-assisted and encoder-based navigation system to estimate the location and pose of a vehicle travelling in a 2D plane. The navigation was accomplished using LEDs, a high-speed camera, and two encoders. The front wheels were fitted with a high-speed camera and encoders. The LED location and their ID were estimated using the captured frames, and the EKF was deployed to fuse measurements from the encoder and camera. Furthermore, [179] describes how to use KF to identify a robot's direction. The geomagnetic and gyro sensors were utilized, and the position was estimated using both the dead reckoning and KF. Hence, the experiment revealed that KF has the lowest ε_p of 10.5 cm with a maximum directional error of $< 6^\circ$. Alternatively, the core principle of the PF algorithm is that a posteriori probability is represented by a set of independent random samples from the proposal distribution known as particles. The posteriori probability is then updated by receiving additional observations, and the Bayes rule adjusts the weight as particles pass through in a certain way. The benefit of this technique is that it can adapt to a nonlinear Gaussian noise model without assuming that the system is linear and Gaussian [180]. In [181], a VLP system was implemented using either a single PD or an array of PD (i.e., camera), in which the PD was employed to detect the presence of the LED as well as its particular identification. Meanwhile, the camera was utilized to measure the AoA of the LED signal, and a navigation system based on this measured information was considered. The mathematical formula was also introduced for the motion model, initialization, and localization process. The results suggested that employing PF enhances trackability.

2.4.3.3 Other Estimation Techniques

Two conventional methods relying on linear least squares (LLS) and nonlinear least squares (NLLS) were used for VLPs [34]. However, NLLS and LLS achieved the minimum ε_p values of 46.42 and 55.89 cm, respectively. An efficient RSS-based VLP algorithm was proposed in [182] to estimate the 3D location, combining 2D trilateration with the NLLS. The computational time for NLLS is limited to approximately 17 ms, which is further reduced to less than 2 ms using a fast search algorithm. A new VLP system was proposed in [183], where a polynomial regression-based approach was utilized to improve the PA of the proposed system. Polynomial regression appears as a method to establish the relation between P_r and d , suitable for multipath environments. The results showed that, the minimum ε_p achieved was 0.6 m by employing a NLLS with polynomial regression model.

The influence of non-line of sight (NLoS) paths in a VLC system implemented in a referenced empty room has been described in the literature. For instance, in [184], the impact of multipath reflections on the indoor VLP system was studied. The results proved that, the minimum ε_p achieved were 46.4 and 0.4 cm with and without multipath reflections, respectively. Therefore, reflections play an important role in estimating the PA, which needs considering. Estimating P_r versus the distance for the case of a multipath channel is a complex task, which depends strongly on the presence of corners, walls, and furniture within a room [184]. Further optimization models for VLP systems have also been employed. For instance, Tabu search as a global optimization algorithm was adopted to provide high precision VLPs [185], in which the LEDs transmit its localised ID information. The Tabu search method was utilised to estimate the position upon detecting the ID information (optical signal) from multiple LEDs.

2.5 Summary

Indoor positioning is a well-known topic that has sparked many studies in the previous decades. Initially, the literature review of this thesis began with an overview of various indoor positioning technologies, see Section 2.3. From the comprehensive analysis of the technologies deployed in IPSs, VLC-based-IPSs have shown an overall advantage based on their immunity to EM interference, license-free operation, large bandwidth, and dual-use for illumination and communication. The VLC-based- IPSs (VLPs) techniques were analyzed based on their common characteristics. The VLP positioning technique refers to the applied procedure to estimate the position based on the acquired light information. VLPs are categorized based on three key characteristics: mathematical, sensor-assisted, and positioning optimization methods. The mathematical based VLP attributes are comprised of three distinctive features of fingerprinting, range-free, and range-based methods. The geometrical properties of circles, spheres or triangles were employed to estimate the Rx position in the range-based technique, in which the signal travel path is measured either through lateration or angulation. The path information from light landmarks be calculated using ToA, TDoA, RSS, and direct detection measurements. A significant amount of research were carried out to find the appropriate implementation approach for the VLPs to achieve optimal performance. Due to their reliance on many characteristics such as the size of an indoor environment, position accuracy, the number of LED Txs, Rxs, and sensors, this chapter also introduced a quantifiable comparison in terms of cost and complexity of these techniques.

Chapter 3

An Indoor Visible Light Positioning System Using Tilted LEDs with High Accuracy

3.1 Introduction

Coronavirus disease 2019 (COVID-19) has had a major impact on the society at a global level, where social distancing, monitoring, and tracking has become effective in controlling and reducing the spread of the virus [186]. Precise localization and tracking technologies for use in indoor and outdoor environments will play a crucial role in dealing with COVID-19 and other pandemic outbreaks in the future. Nowadays, indoor positioning has a prominent contribution in day-to-day activities in organizations such as health care centers, airports, shopping malls, manufacturing, underground locations, etc., for the safe operating environments. In indoor environments, both RF and optical wireless-based technologies could be adopted for localization [187], [188]. Although the RF-based global positioning system offers higher penetration rates with reduced accuracy (i.e., in the range of a few meters), it does not work well in indoor environments (and not at all in certain cases such as tunnels, mines, etc.) due to the very weak signal and no direct access to the satellites [10]–[12]. On the other hand, the light-based system known as a VLP system, which uses LEDs-based lighting infrastructure, could be used at low cost and high accuracy compared with the RF-based system [21], [25].

VLP can be implemented using different techniques. Proximity and scene analysis (i.e., fingerprinting) are considered the simplest methods with relatively low positioning errors ϵ_p i.e., typically in a range of 10 to 45 cm, depending on the fingerprint database [16], [17], [21]. In the scene analysis technique, the estimation process of the relative position can be obtained by comparing the measured value with a pre-measured location of each position and then matching it to determine the real position. However, the measurement can be affected by the distributions of base stations, i.e., TxS, shadowing and blocking, as well as the absolute location (i.e., probabilistic and correlation) dependency on pattern recognition techniques [16]. A VLP using two PDs and an IS was proposed in [21], [25], [26]. Note, VLC with IS (composed of a large PD array) naturally fits well with multiple

inputs multiple-output systems in indoor and outdoor applications. In IS-based VLP, image-processing techniques can be used to determine the position but at the cost of increased complexity [27]. Note that, in VLP the transmission speeds (i.e., data rates) of the PD and IS are not critical at all since the aim is to achieve positioning with high accuracy [28].

Despite the fact that the user's mobility can influence the performance of the VLP system, most research reported in the literature has focused primarily on static scenarios. The major issues of shadowing and blocking affecting user's mobility were reported in [189], where the VLC system performance considering the changes in the channel conditions in different indoor scenarios (i.e., a furniture equipped office room, an empty hall, and a corridor) was investigated. It was shown that, the cumulative distribution function (CDF) of the received power distribution differs in the worst case by up to 7% in a furnished office (people density > 0.16 people/m²). Alternatively, the highest root mean square (RMS) delay spread of 6.5% in comparison with the case with no people was observed for an empty hall. The results also revealed that, the corridor with the maximum RMS delay of 2% at the people density > 0.16 people/m² is the most robust against the people's movement compared with the other two where the problem of shadowing or blockage could be readily avoided. Another concern with the user's mobility is the processing time required that needs considering with respect to the speed of movement for the Rx.

In most of the reported methods, the angular dependency was neglected in RSS-based localization with the assumption that, the Rx has a fixed height and is pointing up towards the Tx's [31]. However, computational and implementation costs are too high, and the assumptions made may not be valid in real-time application scenarios with mobile Rx's, which needs further investigation. Recent works have focused on the impact of multipath induced reflections on the performance of VLP without considering the tilting angles [190]–[192], where it was shown that, multipath reflections considerably increase ε_p ; whereas in [193], it was shown that, the channel capacity can be significantly improved by carefully selecting the Rx's tilting angle θ_{Rx} . However, the initial research demonstrated that in VLP θ_{Rx} usually results in increased ε_p (i.e., lower accuracy).

The widely used commercially available LED spotlights in building facilitates the concept of using Tx's with tilting features. For instance, the impact of the Tx's (i.e., LED)

tilting angle θ_{Tx} on the accuracy of RSS-based VLP was studied in [194], where it was shown that ε_p increased (i.e., in the order of centimeters) with θ_{Tx} . In [195], a 4-LED VLP system using an ANN was proposed to improve the positioning accuracy, which is impacted by the random and unknown static Tx tilt angle with a maximum variation of 2° . It was shown that ANN offered improved performance compared with standard trilateration, achieving localization errors below 1 cm for the LoS channel. In Addition, an RSS-based localization algorithm with multidimensional LED array was proposed in [196], where the design of the lamp structure was introduced to exploit the direction of the LED in a LoS environment. The authors showed that the proposed system achieved a RMS error of 0.04 and 0.06 m in 2- and 3-dimensional localization, respectively for the LED with a tilt angle of 15° . While in [197], an angle diversity Tx (ADT) together with accelerometers was proposed for uplink three-dimensional localization in a LoS environment. ADT was a combination of 19 or 37 LEDs (LEDs array), which were placed on the ground, and PDs located on the ceiling. The results showed that, an average localization error of less than 0.15 m.

The impact of NLoS path in a VLC system deployed in a referenced empty room has been reported in the literature. In [198], the impact of the power levels from NLoS paths on the performance of VLP for different Rx positions and their orientations was reported. It provided a theoretical framework for the design of VLP resource allocation methods to improve the performance of the non-tilted Tx. Channel modeling and its characterisation with the existence of reflections from objects and surfaces were investigated in [199]. Considering the delay spread and the channel gain in a typical room, it was shown that it is not required to consider all objects within rooms [199], [200]. Moreover, the use of flexible organic LED-based VLC in indoor environments (i.e., offices, corridors, semi-open corridors in shopping malls, etc.) was investigated in [201], where it was shown that the channel gain in an empty room is higher by 4.8 and 5.2 dB compared with the fully furnished room and a semi-open corridor, respectively [201].

Unlike previous works, in this chapter the LED tilting is investigated for the first time and show that it can be beneficial in VLPs in improving the PA. The impact of reflections on the accuracy is showed by means of the received power from both LoS and NLoS transmission paths, the positioning algorithm utilized, and the accuracy of the VLP system for a single PD-based static Rx (i.e., putting the Rx at fixed locations) where the user movement has not been considered. In this approach, the Txs are oriented towards

the pointing center F with the (x_F, y_F, z_F) coordinates without violating the acceptable uniformity range of the light distribution in the illuminated region. Note, F is selected at the center of the receiving plane in this work, and alignment is achieved with respect to the Tx normal $\hat{\mathbf{t}}_k$. Fitting using the received power P_R points at various Rx locations for two different circumstances is used to analyse the regression. Note, the Rx locations are within a squared shape region centered at F with a side length D_r . The polynomial regressions (PRs) are fitted with the PR points for the full and half rooms of areas of 6×6 and $3 \times 3 \text{ m}^2$, which is termed as scenarios S1 and S2, respectively-. The study is carried out using the LLS algorithm for position estimation, which is a low complexity solution. Hence, we offer a significant accuracy improvement by up to ~66% compared with a link without Tx's tilt. We show ε_p of 1.7 and 1.3 cm for S1 and S2, respectively, and for z_F of 0 m (i.e., the height of F from the floor level). Furthermore, we investigate z_F with respect to ε_p and we show that, the lowest ε_p of 1.3 and 0.8 cm were for S1 and S2, respectively.

The remainder of this chapter is structured as follows. Section 0 presents the VLC system model used in the positioning algorithm. The positioning algorithm is briefly explained in Section 3.3. The results and discussion are included in Section 3.4. Finally, Section 0 provides the conclusion of the chapter.

3.2 Proposed VLP System Model

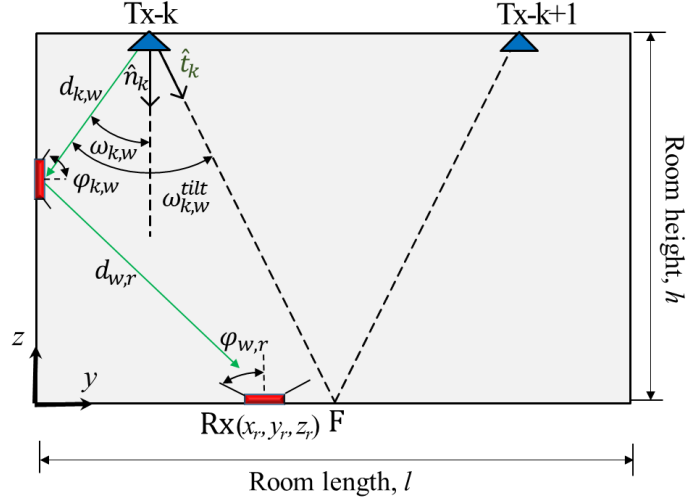
In RSS-based localization systems, positioning accuracy depends mainly on P_R . For NLoS links, reflection from near and far walls should be considered, which contributes to the degradation of PA. For example, Figure 3-1 illustrates a system with two TxS aligned with respect to F (i.e., shown as the tilted Tx normal $\hat{\mathbf{t}}_k$), which is used to investigate the impact of reflections from walls on the accuracy of VLP). Here, the aim is to maximize P_R from LoS paths to improve the accuracy at F, which is initially set at the center of the receiving plane (i.e., x_F, y_F , and z_F are all set to zero). The tilting orientation is estimated based on the position of F, which is given by:

$$\hat{\mathbf{t}}_k = \frac{\overrightarrow{T_k}}{\|\overrightarrow{T_k}\|}, \quad (3.1)$$

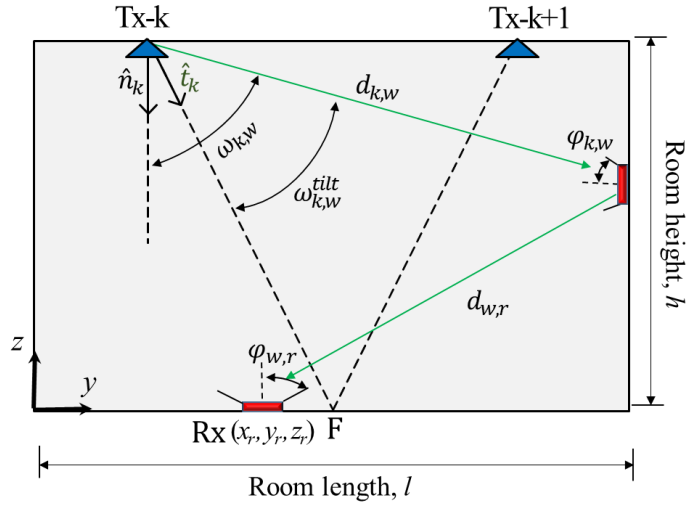
where $\overrightarrow{T_k}$ is a vector that represents the difference between the coordinates of the k^{th} Tx and point F (x_F, y_F, z_F) , and $\|\cdot\|$ is the Euclidean norm. The tilted irradiance angle $\omega_{k,w}^{\text{tilt}}$ is given by:

$$\cos(\omega_{k,w}^{\text{tilt}}) = \frac{d_{k,w} \cdot \hat{\mathbf{t}}_k}{\|d_{k,w}\| \cdot \|\hat{\mathbf{t}}_k\|}, \quad (3.2)$$

where $d_{k,w}$ is the distance between the k^{th} Tx and the reflective area, and \cdot represents the product dot operation.



(a)



(b)

Figure 3-1. An example of a reflected light ray in case of LED tilt: (a) near-wall reflections case, and (b) far wall reflections case.

The NLoS power contributions from the near-wall reflections represented by the Tx's cosine terms expressed in (3.2) can be reduced by tilting the Txs towards F (i.e., $\hat{\mathbf{t}}_k$ is directed towards F) that implies $\omega_{k,w}^{\text{tilt}} > \omega_{k,w}$, where $\omega_{k,w}$ is the irradiance angle with no

tilted Tx, see Figure 3-1(a). Even though the Tx's cosine terms of NLoS signals will increase for the far-wall reflections, which is implied by $\omega_{k,w}^{\text{tilt}} < \omega_{k,w}$, the link experience a higher path loss due to the longer transmission range, see Figure 3-1(b). Having these observations in mind, we can infer that tilting the Txs can be beneficial in VLP by leveraging the effect of reflections from both near- and far-walls. Under this perspective, it reasonable to explore tilting based on F at the center of the receiving plane and investigate how this can improve PA. These observations remain valid for the entire area of the walls when concerning the first reflection. Higher-order reflections also have an impact on positioning accuracy. However, due to the fact that these higher-order reflections have reduced power levels when compared with the LoS and 1st order case in regions near the center of the room, the previous discussion is still valid, and LoS power can be maximized by tilting towards the center.

Figure 3-2 shows the geometrical set-up diagram of the proposed indoor VLP system, which is composed of 4 Txs (i.e., LEDs) and an Rx (i.e., a PD) positioned on the ceiling and the floor level, respectively. Each k^{th} Tx has a known set of coordinates (x_k, y_k, z_k) , which is associated with the world coordinate system (WCS), with $\hat{\mathbf{t}}_k$ of $[\sin\theta_{\text{Tx},k} \cos\alpha_k, \sin\theta_{\text{Tx},k} \sin\alpha_k, -\cos\theta_{\text{Tx},k}]$ where $\theta_{\text{Tx},k}, \alpha_k$ are the tilting and azimuth angles, respectively and k is 1, ..., 4. Note that, in this work, as a reference, an empty room is considered to study the impact of Tx's tilting on the positioning accuracy. The proposed system can be utilized for positioning purposes where the positioning accuracy is a major concern. However, if indoor positioning system uses the already existing wireless communication network architectures, then high accuracy may no longer be critical. Therefore, there exists always a trade-off between the accuracy and other system requirements including scalability, complexity, coverage, etc.

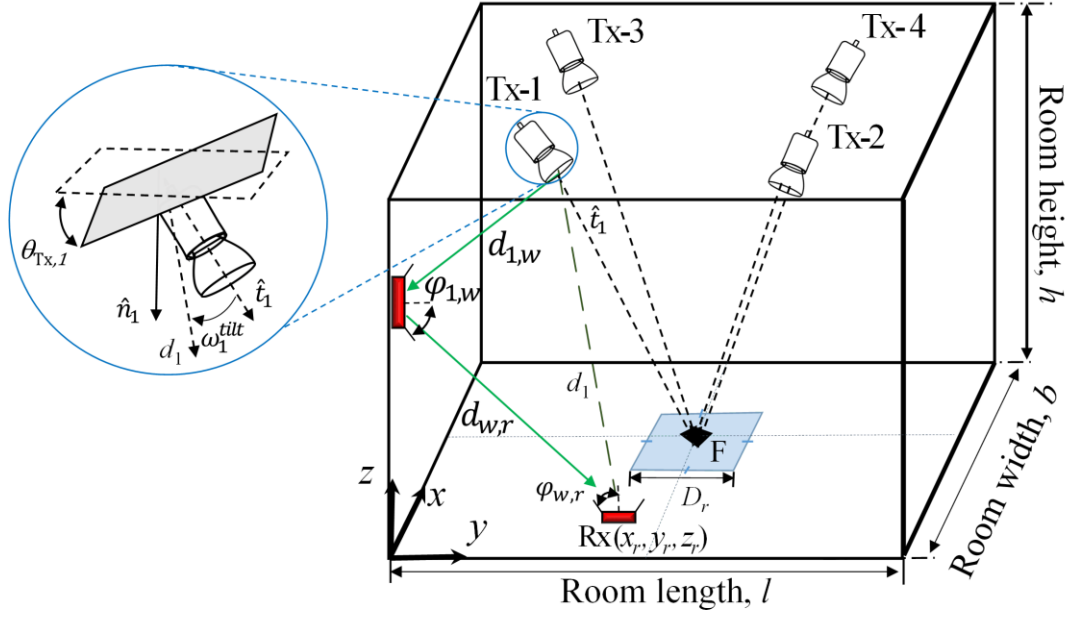


Figure 3-2. The proposed indoor VLP system with the tilted Tx.

Each Tx broadcast unique ID information of 2 bits, which is encoded and modulated using OOK, which allows separation at the Rx using a correlation method that can be received at the Rx in advance of location identification. The Tx identifying bits are given after the header signal and prior to the payload data is transferred in a designated packet for signal broadcasting. The broadcasting process and the proposed model are depicted in Figure 3-3.

Considering the 1st order reflections, the received total power is given by:

$$P_R = \sum P_{R-\text{LoS}} + \sum P_{R-\text{NLoS}}, \quad (3.3)$$

where $P_{R-\text{LoS}}$ and $P_{R-\text{NLoS}}$ represent the received power for LoS and NLoS, respectively. Typically, the signal-to-noise ratio in standard VLC will be high (> 20 dB [202]), which would be considered noise-free in common cases). Moreover, noise sources (mostly dominated by the background lights) [202] will have a similar effect on the VLP system with and without the tilting Tx. Thus, a noise-free system is considered in this work. The conventional trilateration technique based on a range of three minimum observation points offers the advantage of simple geometrical solutions [18]. Using the RSS algorithm and 4-Tx (i.e., LEDs), the $P_{R-\text{LoS}}$ for the LoS path is given as [203], [204] :

$$\sum P_{R-LoS} = \sum_{k=1}^K C_o P_t \frac{\cos^m(\omega_k^{\text{tilt}}) \cos(\varphi)}{\|d_k\|^2} T_s(\varphi) g(\varphi), \quad (3.4)$$

where

$$C_o = \frac{m+1}{2\pi} \mathcal{R} A_r, \quad (3.5)$$

and

$$m = -\frac{\ln(2)}{\ln\left(\cos\left(\frac{\Theta_1}{2}\right)\right)}, \quad (3.6)$$

where K is the total number of Tx's and $\Theta_{\frac{1}{2}}$ denotes the light source irradiance half-power angle, which varies depending on the emitter and reflecting surfaces. There are several models for reflection surfaces accessible in the literature, such as Blinn's or Lafortune's models, which are often used in 3D image rendering and are utilised for high-level specular reflection components and are based on bidirectional reflectance distribution function theories. Typically, the ideal diffuse reflector (Lambertian model) or Phong's reflection scheme are used [205]. ω_k^{tilt} and φ are the tilted irradiance angle from the k^{th} Tx to the Rx and the receiving incident angle, respectively. d_k is the distance between k^{th} Tx and Rx. A_r represents the PD's active area, which is set with a large semi-angle characteristic of 10^{-4} m^2 , and \mathcal{R} is the responsivity, which is set to unity for the sake of simplicity. $T_s(\varphi)$ and $g(\varphi)$ are the gains of the optical filter and the concentrator at the Rx, respectively. Note, the gains of the optical filter and the concentrator at the Rx impose a constant factor on the received signal, as such, they do not condition the achieved results. Hence, $T_s(\varphi)$ and $g(\varphi)$ are set to unity, $\varphi < 90^\circ$ and $d \gg \sqrt{A_r}$. A standard high power LED Chip of 1 W is set for the proposed system.

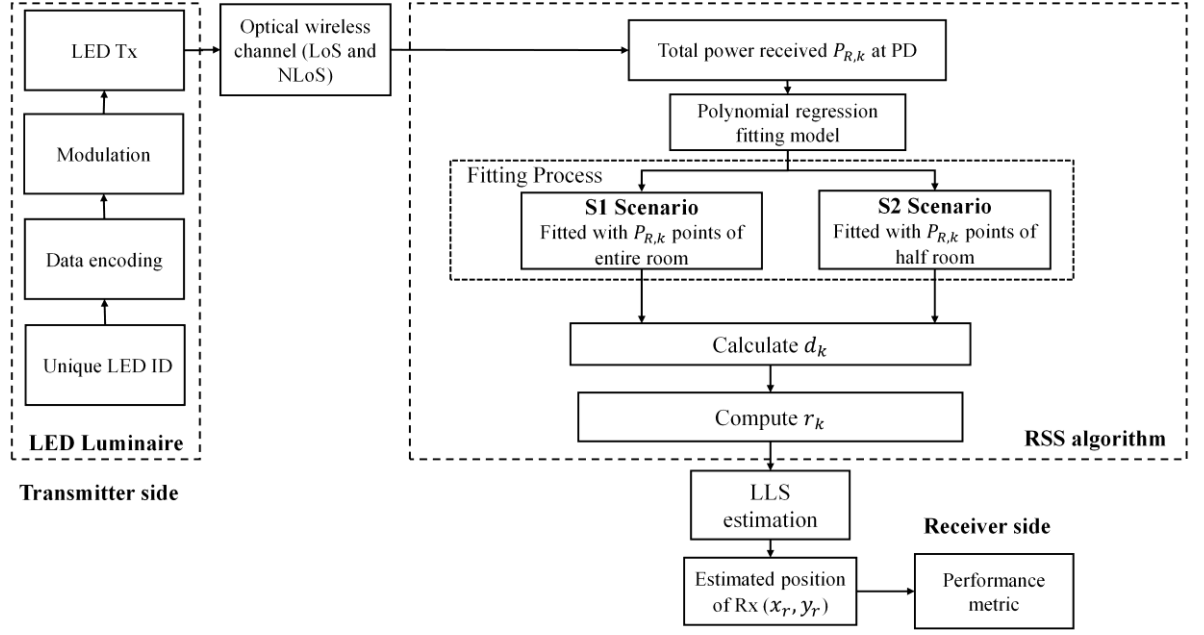


Figure 3-3. Block diagram of the proposed VLP system.

For the NLoS path and considering only the first-order reflection, the received total power can be expressed as [202]:

$$\sum P_{R-NLoS} = \sum_{k=1}^K \sum_{\text{wall}} \rho C_o P_t A_{\text{ref}} \frac{\cos^m(\omega_{k,w}^{\text{tilt}}) \cos(\varphi_{k,w})}{\pi(\|d_{k,w}\| \|d_{w,r}\|)^2} T_s(\varphi_{w,r}) g(\varphi_{w,r}) \cos(\omega_{w,r}) \cos(\varphi_{w,r}), \quad (3.7)$$

where $d_{k,w}$, $\omega_{k,w}^{\text{tilt}}$, and $\varphi_{k,w}$ are the distances, irradiance angle, and the receiving incident angle between the k^{th} Tx and the reflective area, respectively. $d_{w,r}$, $\omega_{w,r}$, and $\varphi_{w,r}$ are the distances, irradiance angle, and the receiving incident angle between the reflective area and the Rx, respectively, see Figure 3-1(a). ρ is the reflection coefficient, which depends on the material of the reflective surface and A_{ref} is the reflection area. P_{R-NLoS} for the signals from the NLoS paths is determined based on the Matlab code 3.2 from [202].

Moreover, the uniform distribution of the P_R inside the illuminated zone is essential in indoor environments [105]. To achieve uniform light distribution on the receiving plane, the same amount of optical power must be received at each place in the receiving plane. However, owing to NLoS power configuration and the effects of reflections from walls, it is difficult to maintain uniform distribution at all points in the illuminated zone.

EN 12464-1 European Commission standardised the uniformity of lighting in indoor environments by defining the minimum acceptable limit of uniformity of light distribution [206]. The uniformity of light distribution in the room (U) is represented as the ratio of the minimum to maximum power intensity at the receiving plane, which is given by:

$$U = \frac{\min(P_R)}{\max(P_R)}. \quad (3.8)$$

Here a grid size of 1 cm resolution is considered with 3600 Rx positions on the receiving plane, which is associated with WCS of (x_r, y_r, z_r) . We have also specified the dedicated region, which is a square shape centered at the point F and located at the receiving plane. The receiving positions are considered inside this region only. All the other key system parameters are given in Table 3.1.

Table 3.1 The key system parameters.

Parameter	Symbol	Value
Room size	(l, b, h)	$6 \times 6 \times 3 \text{ m}^3$
The coordinates of Tx-1 Tx-2 Tx-3 Tx-4	(x_1, y_1, z_1) (x_2, y_2, z_2) (x_3, y_3, z_3) (x_4, y_4, z_4)	$(-1.7 \text{ m}, -1.7 \text{ m}, 3 \text{ m})$ $(1.7 \text{ m}, -1.7 \text{ m}, 3 \text{ m})$ $(-1.7 \text{ m}, 1.7 \text{ m}, 3 \text{ m})$ $(1.7 \text{ m}, 1.7 \text{ m}, 3 \text{ m})$
Transmit power per Tx	P_t	1 W
Rx's field of view	FoV	75°
Half power angle	HPA	60°
PD area	A_r	10^{-4} m^2
Responsivity	\mathcal{R}	1 A/W
Reflection coefficient	ρ	0.7

3.3 Positioning Algorithm

3.3.1 Distance Estimation Using Polynomial Regression

The block diagram of the proposed VLP system is shown in Figure 3-3, in which P_R is processed to estimate the Rx position. Distance estimation is the central feature of the RSS positioning approach, and for LoS paths it is normally deducted from (4), which is estimated as:

$$\|d_k\|^2 = \|r_k\|^2 + h^2, \quad (3.9)$$

where h is the vertical distance between the Tx and the Rx. The estimated distance between the Rx and the k^{th} Tx can be estimated from (4), which is given by:

$$r_k = \sqrt{\left(\frac{P_t C_o h^{m+1}}{P_{R-\text{LoS},k}}\right)^{\frac{2}{m+3}} - h^2}, \quad (3.10)$$

where, $P_{R-\text{LoS},k}$ is the LoS received power at the Rx from the k^{th} Tx. In NLoS links, this approach results in increased errors due to reflections [207], [208], therefore the distance estimation approach using (10) is no longer valid. One possible approach would be to generate a polynomial regression fitted model for the power and distance relationship. The regression analysis is the process of determining the connection between a dependent

variable and one or more independent variables. It is one of the most essential statistical techniques, and it is often used to analyse the relationship between two or more linked variables. A relationship model is theorised, and parameter estimations are utilised to build an estimated regression equation. The relationship between the power and distance is defined by:

$$d_k = a_0 + a_1 P_{R,k} + a_2 (P_{R,k})^2 + \dots + a_j (P_{R,k})^j, \quad (3.11)$$

where a_j is the coefficient of the fitted polynomial at j^{th} degree polynomial and $P_{R,k}$ is the total received power at the Rx from the k^{th} Tx. Note, d_k is computed using (11), which is then substituted into (9) to determine r_k .

3.3.2 LLS Estimation

LLS is adopted to analyze the performance of the proposed system by considering the estimated distances of the NLoS paths, which is a low complexity solution as compared with the NLLS algorithm. Following geometric properties, a minimum of 3-Tx located at the center of the circle is required, where the estimated distance is considered as the circle radius, see Figure 3-4. The intersection point of the three circles is considered as the measured position of the Rx.

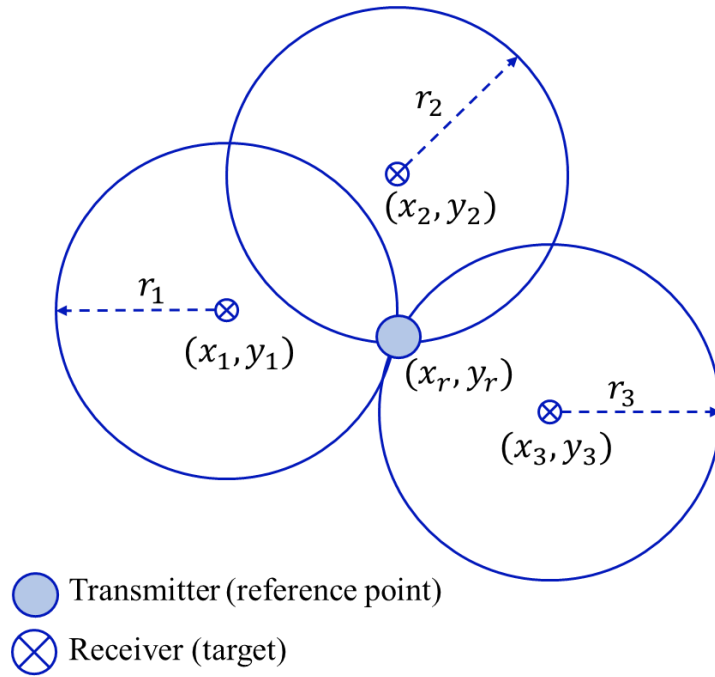


Figure 3-4. Positioning based on RSS.

For a k^{th} LED luminaire that is positioned at (x_k, y_k, z_k) and the Rx is located at (x_r, y_r, z_r) . A closed-form solution using the LLS estimation method is given by:

$$X = (A^T A)^{-1} A^T B, \quad (3.12)$$

where

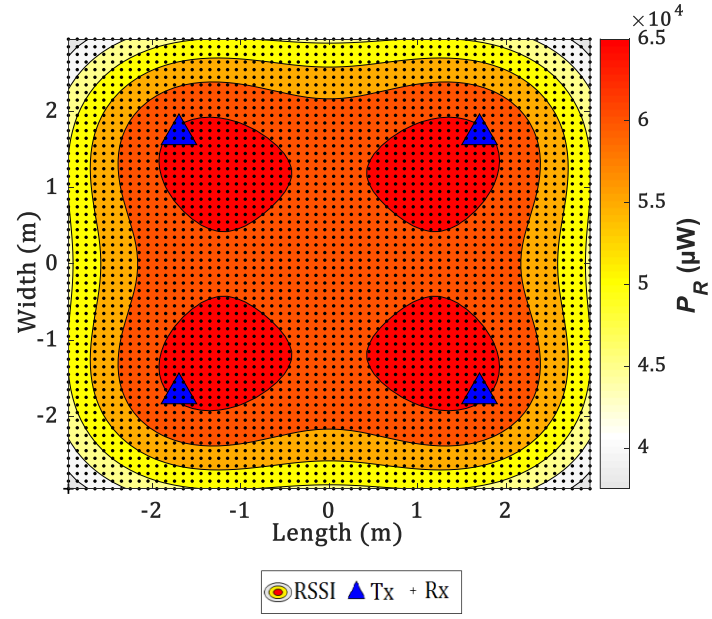
$$A = \begin{bmatrix} x_2 - x_1 & y_2 - y_1 \\ x_3 - x_1 & y_3 - y_1 \\ x_4 - x_1 & y_4 - y_1 \end{bmatrix}, \text{ and } X = \begin{bmatrix} x_r \\ y_r \end{bmatrix}, \quad (3.13)$$

$$B = 0.5 \times \begin{bmatrix} (r_1^2 - r_2^2) + (x_2^2 + y_2^2) - (x_1^2 + y_1^2) \\ (r_1^2 - r_3^2) + (x_3^2 + y_3^2) - (x_1^2 + y_1^2) \\ (r_1^2 - r_4^2) + (x_4^2 + y_4^2) - (x_1^2 + y_1^2) \end{bmatrix}. \quad (3.14)$$

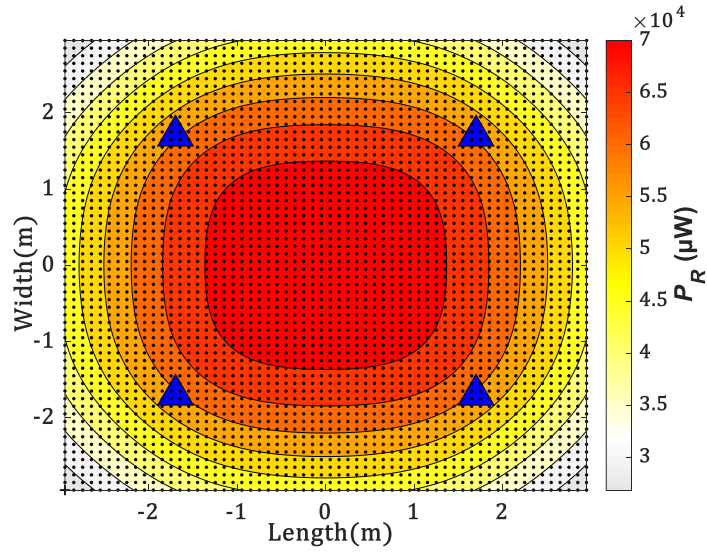
3.4 Results and Discussion

3.4.1 Impact of the Tx Tilting on the Radiation Pattern

The P_R is estimated based on equation (3.3). Figure 3-5 shows the received power distributions for the link (i.e., received signal strength indicator RSSI) with and without the tilting Tx. Note, the Tx are directed towards F following the proposed model in Section 2. As shown in Figure 3-5(b), there is a significant improvement in the power distribution with the tilting Tx (i.e., a much more uniform distribution) around the center of the receiving plane. For example, a P_R with a range of 5×10^4 to 7×10^4 μW is obtained around the center. However, P_R is reduced to a range between 6×10^4 and 6.5×10^4 for the same region. Note, that the uniformity measurements are introduced in subsection 3.4.4. All the observed tilted Tx normal $\hat{\mathbf{t}}_k$ for 4-Tx are given in Table 3.2.



(a)



(b)

Figure 3-5. The received power distributions for the proposed system for the Txs with: (a) no tilting, and (b) tilting.

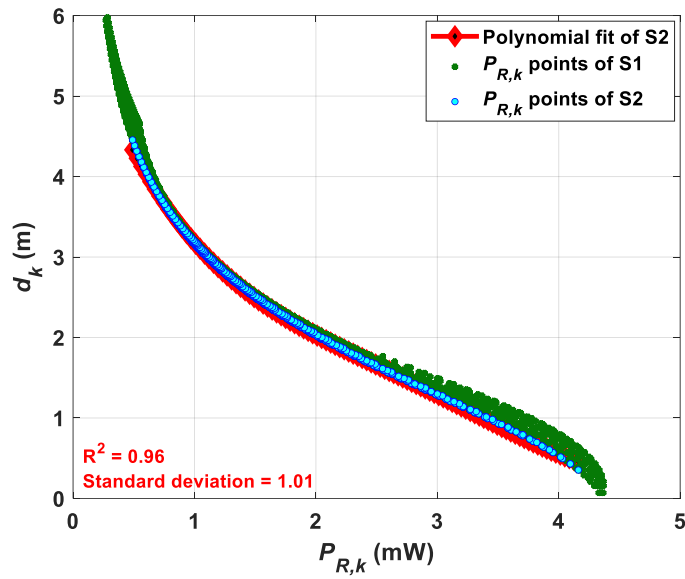
Table 3.2 The values of tilted Tx normal for all Txs.

Tx Number	Tilted LED Normal, \hat{t}_k
Tx-1	[0.4, 0.4, -0.8]
Tx-2	[-0.4, 0.4, -0.8]
Tx-3	[0.4, -0.4, -0.8]
Tx-4	[-0.4, -0.4, -0.8]

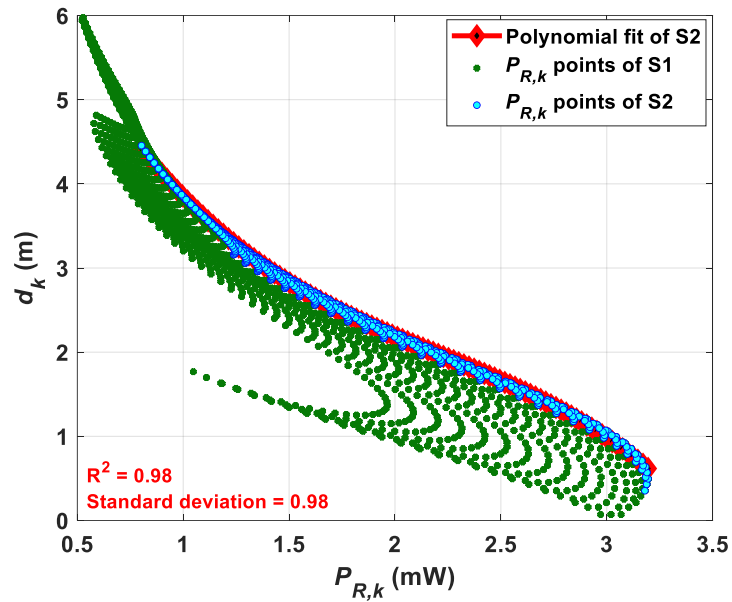
3.4.2 Polynomial Fitting

With reference to Figure 3-3, d_k is estimated based on $P_{R,k}$ and the PR (polynomial regression) method as outlined in Section 3.1. The accuracy and precision of fitting are measured by the coefficient of determination R^2 , which is a statistical measure of how close the data are to the fitted regression line, and the standard deviation. Note, PR is considered for various data points and categorized into two scenarios S1 and S2 based on the room dimensions. For scenarios S1 and S2, the PRs are fitted with $P_{R,k}$ points for the full and half rooms of areas of 6×6 and 3×3 m², respectively. The deviation of $P_{R,k}$ points is impacted mainly by the reflections wherein the data near the walls imply a larger estimation error as stated previously in the literature [31], [202]. Therefore, 3600 samples (a full room with a 1 cm grid size) are considered for the polynomial fitting for S1, while for S2 we only have considered 900 samples (an inner half room). A stabilized residual sum of squares is achieved with the polynomial order j of 4. The polynomial coefficients of the fitted curve and R^2 are estimated for both S1 and S2.

The polynomial fitted curves for VLP without and with the tilting TxS are illustrated in Figure 3-6. The green points and blue plots indicate the $P_{R,k}$ points for the full and half rooms, respectively. Figure 3-6(a) shows that, the $P_{R,k}$ points span between 0 and 4.2 mW, and are uniformly distributed for both S1 and S2. However, Figure 3-6(b) depicts that the $P_{R,k}$ points for S1 are more scattered with a smaller span of 0.5 to 3.2 mW, which corresponds to the corner of the room. In S2, the $P_{R,k}$ points are more focused towards S2 due to tilting of the Tx, thus the fitting data points are considered for S2 only. From the results obtained, both R^2 and the standard deviation are positively affected with tilting of the Tx, i.e., higher R^2 value of 0.98 and lower standard deviation of 0.98 is achieved for the tilted Tx as compared with a lower R^2 value of 0.96 and higher standard deviation of 1.01 in the case of no tilted Tx, see Figure 3-6(b). Table 3.3 shows the estimated polynomial coefficients and R^2 values for S2 with and without the tilted TxS.



(a)



(b)

Figure 3-6. The distance estimation for Tx-k using the PR method employed in S2 for the Tx with: (a) no tilting, and (b) tilting.

Table 3.3 The coefficients of the polynomial fitted curve for the scenario S2.

Cases	Estimated polynomial coefficients (no units)					R^2
	a_0	a_1	a_2	a_3	a_4	
With tilted Tx	7.38×10^4	-3.60×10^5	2.37×10^4	-6.26×10^2	8.10	0.98
Without tilted Tx	8.86×10^6	9.93×10^5	3.96×10^4	7.35×10^2	7.44	0.96

3.4.3 Impact of the Tx Tilting and the Altitude of F on VLP

In this section, we investigate ε_p for different values of D_r to realize the impact of tilted TxS near the center of the receiving plane, and further analyze the impact of changing the height of z_F on the positioning accuracy. Figure 3-7 illustrates $\text{Inv}(90\%)$ as a function of D_r for S1 and S2 with the LLS algorithm, which is applied for the case with LoS and NLoS paths to estimate the Rx's position, as described in Section 3. The quantile function $\text{Inv}(\chi)$ is used as a performance metric to observe the confidence interval of ε_p , which is given by:

$$\varepsilon_{p,\chi} = \text{Inv}(\chi) = \text{CDF}^{-1}(\chi), \quad (3.15)$$

where χ is the percentage of the confidence interval, and CDF represents the cumulative distribution function of ε_p .

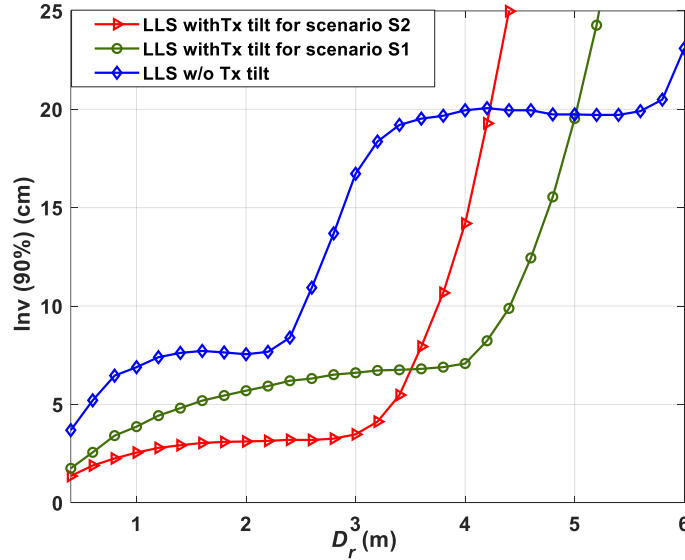
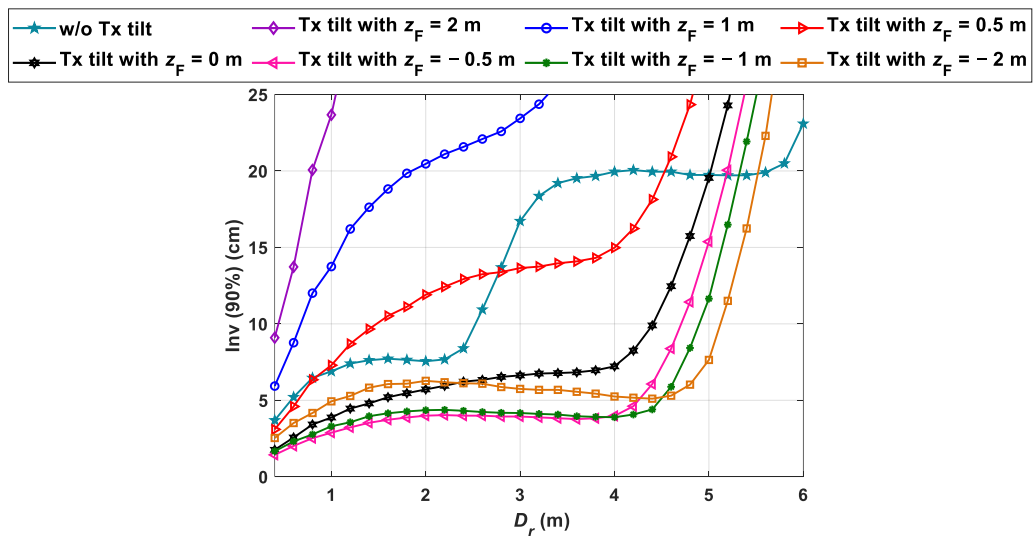


Figure 3-7. The measured quantile function at χ of 90% for various D_r for LLS with and without the tilted TxS.

To ensure a VLP link with high reliability, we have selected a 90% confidence interval for ε_p to include the majority of the measured points. Note that, the TxS' tilting angle is fixed at the point F for all values of D_r . Moreover, the error can be reduced significantly depending on S1 or S2. For instance, for S1, ε_p values of 1.7 and 3.6 cm are obtained for both tilting and non-tilting scenarios, respectively for D_r of 40 cm. In addition, we have achieved the accuracy improvement of 44, 24, 60, and 64% for D_r of 1, 2, 3, and 4 m, respectively with the maximum accuracy improvement of 66% for D_r of 3.6 m. In addition, for S2, ε_p of 1.3 cm is obtained for the observation area with D_r of 40 cm with

the tilted Tx. Hence, the Tx's tilting (LED tilting angle) can improve the positioning accuracy in both S1 and S2 with the same detection area of $5 \times 5 \text{ m}^2$ (up to D_r of 5 m) as compared with the case with non-tilting Tx. This could be explained by the fact that, for large observation areas (i.e., large D_r), the CDF of the error becomes affected by the walls and corners of the room, with no improvement in the accuracy. Hence, the NLoS paths become dominant for regions far away from the point F, which degrades the positioning accuracy. Therefore, the proposed VLP system with the tilted Tx's outperforms the system with no tilting Tx's for almost the entire room i.e., an area of $5 \times 5 \text{ m}^2$.

We further analyze the impact of changing the height of pointing center F (i.e., z_F) on the positioning accuracy, which is eventually the variation in the Tx's tilting. Figure 3-8 depict the $\text{Inv}(90\%)$ as a function of D_r for a range z_F (i.e., -2 to 2 m) with and without the tilting Tx's for S1 and S2. Note that, a high negative value of z_F implies that the Tx is pointing vertically downwards towards the Rx. For instance, $-\infty$ for z_F corresponds to the standard non-tilted case and it does not imply reception under the floor. From the Figure 3-8, it is observed that, (i) ε_p increases and decreases with the positive and negative values of z_F (i.e., $z_F > 0, < 0$), respectively for both S1 and S2; (ii) the minimum ε_p of 1.3 cm is at z_F of -0.5 m compared with 1.7 cm for z_F of 0 m for S1 with D_r of 40 cm, see Figure 3-8(a); and (iii) the lowest ε_p is achieved at $-2 < z_F < 0$ m depending on the value of D_r . The proposed VLP system can be further improved for the regions with D_r of up to 5.5 m by adjusting the negative value of z_F . For S2, the minimum ε_p of 0.8 cm is observed at z_F of -2 m and D_r of 40 cm compared with 1.3 cm at F (i.e., $z_F = 0$ m), see Figure 3-8 (b). However, the case with tilting Tx's offers the lowest ε_p for D_r up to 4.36 m.



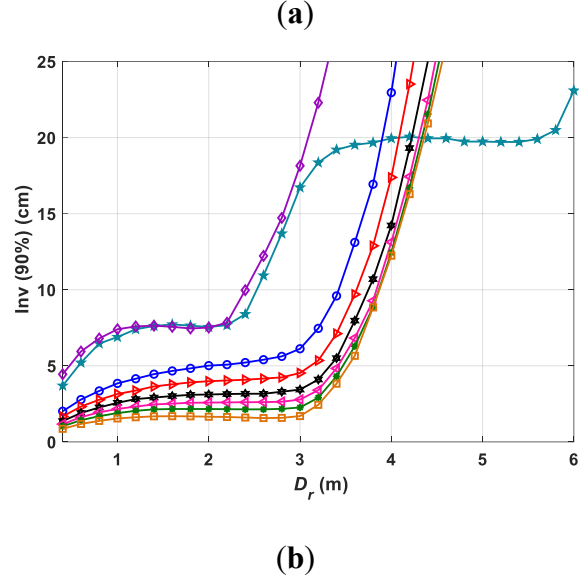


Figure 3-8. The measured quantile function at χ of 90% for various z_F values for: (a) S1, and (b) S2.

3.4.4 Uniformity

The uniformity measurement is employed based on equation (3.8). Figure 3-9 shows the uniformity of light distribution U against D_r without and with the tilting Tx and a range of z_F . The dashed line represents the EN 12464-1 European standard of lighting in an indoor environment [206], which defines the minimum acceptable ranges of uniformity of the light distribution. For $D_r < 5$ m all plots are above the EN 12464-1 line. We have shown that the proposed VLP system with the tilting Tx is capable of providing higher uniformity for the entire room for $z_F \leq -1$ m. Besides, the proposed system shows a similar response for the standard non-tilted case and z_F of $-\infty$. In addition, the uniformity values is reduced for $D_r > 4$ m in the standard non-tilted case and z_F of $-\infty$. This could be explained by the fact that, for large observation areas (i.e., large D_r), the uniformity becomes affected by the multipath reflections near walls and corners of the room.

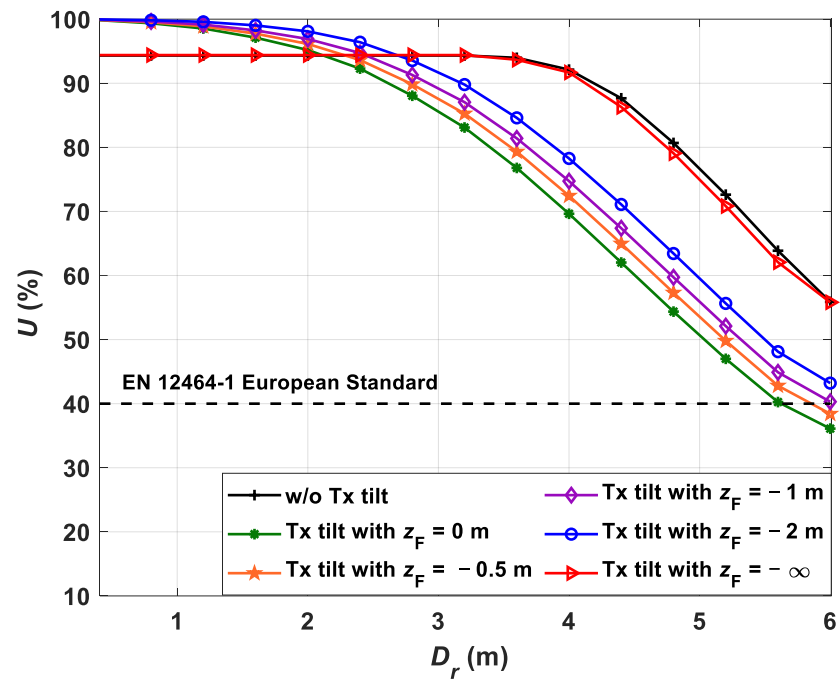


Figure 3-9. The uniformity of light distribution in different D_r w/o and with the tilting TxS.

3.5 Summary

In this chapter, a novel approach was proposed to achieve a highly accurate indoor VLP system by considering multipath reflections. Initially, the Tx was tilted towards the center of the receiving plane to achieve higher accuracy by maximizing the received power level due to contributions from the LoS paths at the pointing center F. The positioning error was estimated by using the LLS algorithm with polynomial regression. We investigated the regression fitted with the received power points for two scenarios of S1 and S2. The results showed a significant improvement in the accuracy by up to ~66% compared with a typical non-tilting Tx case. In addition, positioning errors of 1.7, and 1.3 cm were obtained for the tilted Tx for S1 and S2, respectively at z_F of 0 m. The results also showed that, the uniformity of the proposed VLP system in line with European Standard EN 12464-1, therefore meeting the uniformity requirement of the visible illumination regions. Furthermore, we improved the accuracy of the proposed VLP system by controlling the height of F by achieving the lowest ε_p of 1.3 and 0.8 cm for S1 and S2, respectively. Ultimately, it was concluded that the proposed VLP system with the tilting Tx outperforms the non-tilted Tx scenario. Likewise, we could gain lower ε_p when considering S2, whereas ε_p will increase with D_r as indicated for S1.

Chapter 4

A Unilateral 3D Indoor Positioning System Employing OCC

4.1 Introduction

Driven by the vast existence of smart devices and the rapid spread of new embedded applications, cameras are now considered the key sensor for enabling the IoT applications as part of the current and future smart environments. The complementary metal-oxide semiconductor ISs have been the most widely used devices in many applications in the last decade, with a revenue quadrupling between 2010 and 2019 to reach over \$18 billion [36]. The ISs have set nine consecutive record-high sales levels in the last nine years, and are poised to reach over \$24 billion by 2025. The overall market is set to grow at a compound annual growth rate of 10.5 % between 2020 and 2025 [209]. Thus, it is the very good reason to explore the potential of ISs for other applications including positioning and sensing, to complement vision. In addition, we have seen the widespread use of LED-based lighting fixtures at a global level, which is green, sustainable, and with fast switching capability, that can be used as optical access points in both indoor and outdoor applications [210].

In recent years, there have been marked growing research activities in VLP systems for indoor and outdoor applications within the scientific community. This is because of key features including low complexity, robustness to RF induced interference, directive propagation, energy efficiency, and limited signal reflections and scattering from the environment, hence, providing es high positioning accuracy at low overhead costs [1]. With the above features, VLP can be used in numerous applications including location tracking, navigation, ITS, shelf-label advertising in supermarkets and shopping malls, robot movement control, manufacturing, medical surveillance, street advertising, etc [50], [51], [60].

Table 4.1 Key system parameters.

Ref.	No. of Tx	No. of Rx	Test condition (m)	Technology	Accuracy
[163]	3 LEDs	Single IS	$NA \times NA \times 2$	OCC based communication	10 cm
[164]	4 LEDs		$NA \times NA \times 2.6$	Rolling shutter and multiple frequency-shift keying	2 cm
[165]	Single LED		$14 \times 1.6 \times 2.3$	IMU, and pedestrian dead reckoning algorithm	Real-time decimetre-level, several centimetres
[169]			$0.7 \times 0.3 \times 0.2$	Both AoA and the RSS with k nearest neighbours in feature space algorithm	1.97 cm
[170]			$1 \times 1 \times 2.4$	AoA and RSS with a geomagnetic field sensor and an accelerometer	<10 cm
[166]			$NA \times NA \times 1.2$	Rolling shutter and piecewise fitting. LED Tx detection algorithm.	The average 2D/3D were 3.17/4.45 cm
[171]			$1.8 \times 1.8 \times 2$	IMU	16 cm. Angle accuracies of 1.5° , 1.5° , and 15° were obtained for pitch, roll, and azimuth angles, respectively
[173]			$NA \times NA \times 2.8$	Flicker-free line coding with OOK modulation scheme was used for ID transmission.	Accuracy is 7.5 cm, user moving speed of up to 18 km/h, and computational time reduced to 22 ms and 35.7 ms for 1 LED and 2 LEDs, respectively
[167]			$2.7 \times 1.8 \times 1.8$	IMU and a plane intersection-line scheme	Average ε_p of 5.44 cm, 5.58 cm was achieved for a height of 1.75 m, and 1.45 m, respectively
This chapter				$2 \times 2 \times 2.5$	AoA and RSS OCC based communication

In indoor VLP systems, LEDs are used as the transmitters (Tx) and a PD, or an array of PDs in the form of a single IS are used as the Rx. Compared to the PD, IS-based VLP offers several key features such as (i) much more useful information on the LEDs' locations for use in vision processing-based algorithms; (ii) the ability to separate light sources, thus no need for complex multiplexing mechanisms; (iii) parallel transmission capabilities; and (iv) significantly higher accuracy compared with low frequency RF and ultrasound-based systems. Table 4.1 presents the recent works reported in IS-based VLP. For example, in [163], a distance estimation technique was implemented using both photography and IS-based communication (i.e., OCC), where an average estimation positioning error ε_p of 10 cm using 3-Txs was reported. Likewise, 4-LED and IS were used at the Tx - to transmit location information simultaneously using multiple frequency-shift keying - and the Rx, respectively, with a maximum ε_p of 2 cm at a linkspan of 100 cm [164]. In [165], a hybrid IS-based VLP and pedestrian dead reckoning for indoor application was proposed. The experimental results showed that, the proposed scheme could achieve both cell recognition and 3D positioning by capturing an image of a single Tx (i.e., LED) with the 2D and 3D average ε_p values of 2.46 and 13.4 cm, respectively.

In [166], a VLP system with a single LED lamp and the commercial mobile phone-based Rx was investigated. A LED-based Tx detection algorithm was proposed for identifying the edge of the light source based on brightness weakening, Sobel operator, and the least-square error (LSE) fitting. The experimental results revealed confirmed ε_p of a few cm for different Rx orientations. In [171], a VLP method using a single LED luminaire and a commercial off-the-shelf smartphone camera as the Tx and the Rx, respectively. Note, the inertial measurement unit (IMU) and the IS were deployed for localization purposes, whereas projective geometry was used to calibrate the orientation measurements. The experimental results showed that an average ε_p of 11.2 cm. Furthermore, IS may be utilised to create the illusion of a three-dimensional image. In photos or movies, the sense of depth is created by displaying a different image to each eye [30]. This is sometimes referred to as stereoscopic imaging or depth perception. The benefit of stereoscopic depth estimation is its capacity to generate dense depth maps of the environment using stereo-matching techniques. However, dense stereo depth estimation requires high computational capabilities since equivalent points in the stereo images must be matched. Furthermore, dense depth estimation utilising stereo images

suffers from the image sensors' restricted dynamic range, for example, due to pixel saturation in bright spots [211].

In most of the works reported in the literature studies, either multiple LEDs have been used for positioning or an additional sensor has been employed to obtain the position, see Table 4.1. However, in most scenarios, the narrow FoV of the front-facing camera in smartphones restricts the number of Tx's being captured at the IS, thus making bilateration or trilateration impractical. In addition, unilateration allows less complex and low-cost implementation of the VLC system. Also, the deployment of more LEDs will certainly add some constraints to the implementation of VLP. Therefore, to overcome these issues, in [165]–[167], [169]–[171], different technologies were investigated. For example, the use of an IMU sensor with OCC was reported in [165], [167], [168] with ε_p of several centimeters. Whereas, in [169] a VLP system using a single LED-based Tx and an IS was reported, where the AoA of the transmitted light was determined using the IS and the projection model of the lens. The IS acts simultaneously as a PD for measuring the RSS. Both measurements were utilised as the fingerprint to estimate the Rx's position. The k nearest neighbours in the feature space algorithm were deployed to achieve a more accurate coordinate estimation of the Rx at the cost of increased complexity. The preliminary experimental results showed that, the proposed positioning scheme achieved a high precision where the 95th percentile accuracy was 1.97 cm. Likewise, both AoA and RSS were used in indoor VLP in [170], which was based on a particular frame reception technique designated as the bokeh effect. The system was set intentionally to generate a frame in an out-of-focus condition, thus, avoiding optical power saturation by spreading the received power P_r to the adjacent pixels. The experimental results showed ε_p of < 10 cm.

In this chapter, we introduce a novel low complex and highly accurate AoA-RSS-based VLP system, which mitigates the error induced by the lens at the Rx by employing a single LED and an IS. We demonstrate that, the proposed system outperforms RSS for all circumstances and AoA reported previously. The experimental results show that, a 3D average ε_p of 4.35, 5.49, and 2.85 cm in the x , y , and z directions, respectively. Furthermore, we have investigated the impact of the camera exposure time τ on the detection of the Tx's location and show that the proposed scheme offers immunity against τ in the range of 250 μ s to 4 ms.

The rest of the chapter is organized as follows: In Section 4.2, we present the proposed system model. Section 4.3 outlines the results and discussion. Section 4.4 summarises the chapter.

4.2 System Model

Figure 4-1 shows the geometrical set-up diagram of the proposed indoor camera-based VLP system, which is composed of the Tx module the channel and the Rx unit. At the Tx, the LED ID in the OOK format is generated in Matlab® and is used for intensity modulation of the light source located on the ceiling via the sampler and LED driver for transmission over the free space channel with a transmit power P_t , see Figure 4-1(a). The coordinate of LED is $[x_L, y_L, z_L]^T$, which is associated with the world coordinate system (WCS). At the Rx, a CMOS IS positioned at the floor level at a height L from the Tx, see Figure 4-1(b), is used for detection of the intensity-modulated light beams. Here, we have used the rolling shutter-based OCC technique. The Rx's WCS coordinate R is at $[x_r, y_r, z_r]^T$. Figure 4-1(b) shows the 3D projection of LED in the 2D image plane using a lens. Note that, the lens is set such that to make the image defocused to ease the detection of the LED illumination pattern. The central coordinates of the LED projection are described based on the horizontal and vertical pixels in the image plane, i.e., (u, v) , where $u = 1, \dots, U$; $v = 1, \dots, V$. U and V are the maximum number of pixels in horizontal and vertical directions in the image, respectively.

The raw frames are captured in a lossless format, known as a digital negative, to eliminate the error caused by the different compression techniques used in other formats. To detect the Rx's position, the captured frame $\mathbf{F}_{U \times V}$ is processed as outlined in Figure 4-1 (c), in which, $\mathbf{F}_{U \times V}$ is converted into grayscale to eliminate the chromatic aberration induced by the camera lens [212]. $\mathbf{F}_{U \times V}$ is then binarized to maximize the efficiency of the proposed algorithm. Next, the system is designed to initially detect the LED footprint i.e., region of interest (ROI). Considering that the radiation patterns of typical Tx LEDs follow Lambertian profile [213], a circular Hough transform (CHT) method is used to detect the LED illumination footprint, see following subsections.

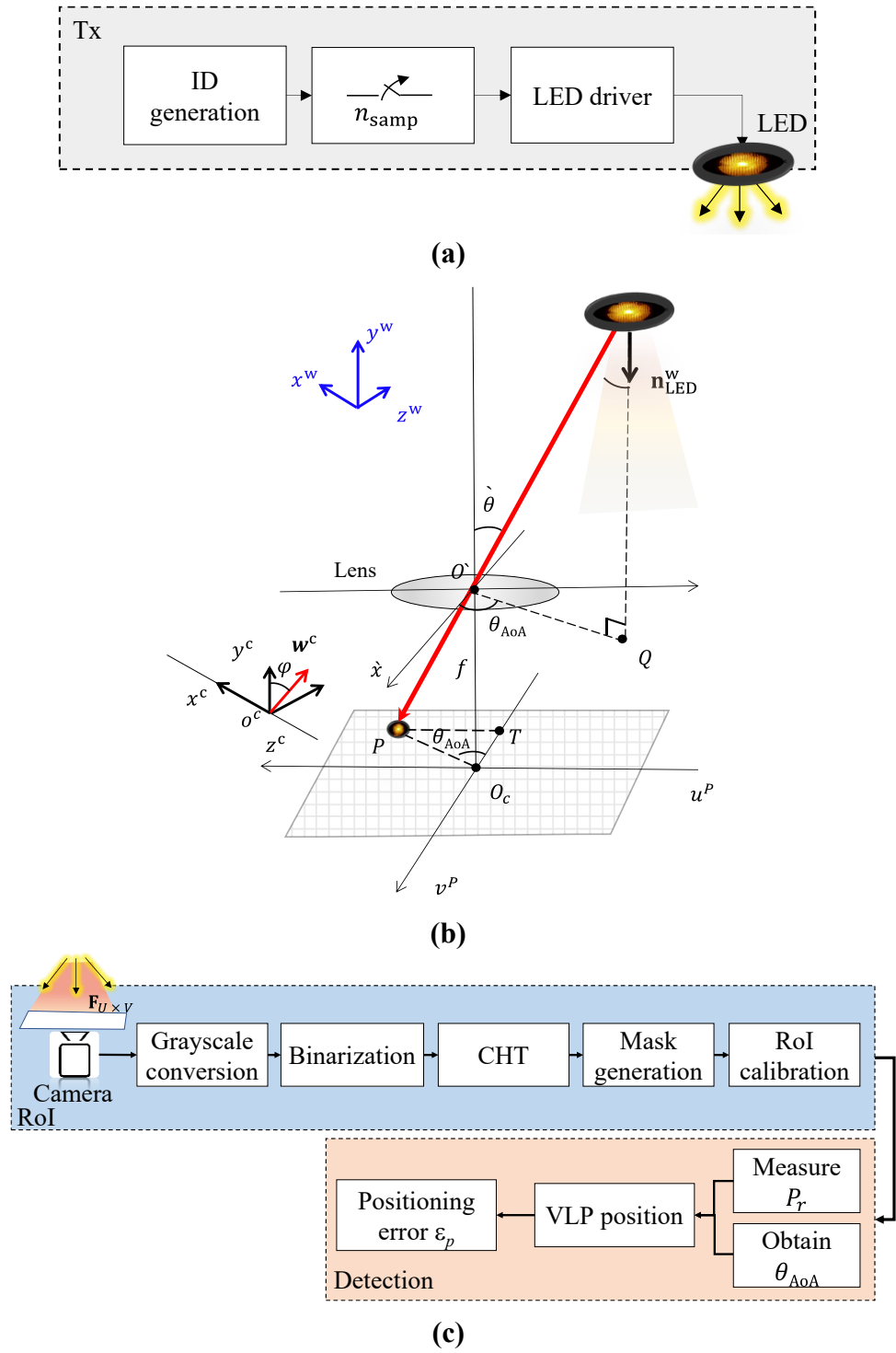


Figure 4-1. System model for the proposed positioning method: (a) Tx block diagram, (b) projection of a 3D object on a 2D image, and (c) flowchart of detection and extraction of information required for positioning.

The Rx's position is estimated using AoA and RSS algorithms. The RSS and AoA are extracted from the identified ROI at the captured frame. Initially, the RSS is measured by accumulating the amount of light energy received inside the ROI. The frame is then

multiplied by a proposed ellipse-shaped mask. Finally, the AoA is measured for the produced frame. The detailed description is explained in the following subsections.

4.2.1 ROI Detection Using CHT Algorithm

The LED illumination footprint on the image plane is extracted using the CHT. The extraction process is done via a voting process as described in Algorithm I. The circle description is done by applying a full sweep of θ for 360° to locate the Tx's fingerprint with a radius r_c and the centre coordinates of (x_c, y_c) . The CHT method was implemented offline using Matlab® and by including three main steps of the accumulator array computation, centre estimation, and radius estimation.

Algorithm 4-1 CHT for pupil boundary detection using 2-D accumulator array.

Input: The raw dng file of captured frame $\mathbf{F}_{U \times V}$, minimum circle radius (r_{\min}) and maximum circle radius (r_{\max})	
Output: Circle radius (r_c) and centre coordinates (x_c, y_c)	
1	for (pupil_radius = r_{\min} ; $r \leq r_{\max}$; $r = r + 1$) do
2	A=zeros(rows,cols) ; // 2-D accumulator of the iris image size
3	for each “Edge-point (a,b)” in edge map of $\mathbf{F}_{U \times V}$ do
4	for $\theta = 1$; $\theta \leq 360^\circ$; $\theta = \theta + 1$ do
5	$x = \text{round}(a + r * \cos \theta)$
6	$y = \text{round}(b + r * \sin \theta)$
7	if (x,y) is in image bounds do
8	$A(x,y) = A(x,y) + 1$; // Accumulator-voting step
9	end if
10	end for
11	end for
12	Find maximum value in A:
13	$M = A(x', y')$; //M is maximum value in A
14	Max_Array(pupil_radius) = M ;
15	X_Array(pupil_radius) = x' ;
16	Y_Array(pupil_radius) = y' ;
17	end for
18	$M' = \text{Max_Array}(\text{index})$
	//Find maximum in Max_Array:
19	$r_c = \text{index}$; $x_c = X_Array(\text{index})$; $y_c = Y_Array(\text{index})$;
	// End of CHT algorithm

4.2.2 RSSI- based IS Measurements

The image distance p is determined based on the RSS measurements. The received optical power via the line-of-sight paths is considered as non-frequency selective with the path loss being proportional to the inverse of L^2 . The amount of light energy received at each frame depends mainly on the P_t and τ . The regenerated electrical signal is converted into a digital format within the camera. The channel impulse response is given by [212]:

$$\mathbf{H}_{U \times V}^{\text{total}} = \mathbf{H}_{U \times V} \otimes \mathbf{H}_{\text{CoC}}, \quad (4.1)$$

where \otimes denotes matrix convolution, \mathbf{H}_{CoC} is the kernel of the circle of confusion (CoC), and $\mathbf{H}_{U \times V}$ represents the channel impulse response of the captured frame (U, V) . The received power at a single-pixel (u, v) is given by [214]:

$$P_r(u, v) = \int_{t_0}^{t_0 + \tau} h(u, v) P_t dt, \quad (4.2)$$

where $h(u, v)$ is the channel response of a single pixel (u, v) , which is estimated as:

$$\begin{aligned} h(u, v) &= \int_{x_{u-1}}^{x_u} \int_{y_{v-1}}^{y_v} R_t A_r \cos(\theta_{\text{AoA}}) \cdot \frac{dx dy}{L^2}, \quad u = 1, \dots, U; \quad v \\ &= 1, \dots, V, \end{aligned} \quad (4.3)$$

where the horizontal and vertical boundaries of an area covered by the pixel (u, v) are x_{u-1}, x_u, y_{v-1} , respectively. R_t and θ_{AoA} denote LED's Lambertian pattern and the angle of arrival on the IS, respectively. A_r is the entrance pupil of the lens, which is directly proportional to the IS aperture size, and L is the required distance between the LED and the Rx. Consequently, the sum of pixels output value within the LED illumination footprint (i.e., ROI), which is denoted as $\mathbf{F}_{U \times V}^k$, constitutes the required P_r .

4.2.3 Ellipse-shaped Mask Generation

The accuracy of the VLP system depends on the RSSI and AoA measurements. The ROI centric point estimation is required for AoA estimation, which may be influenced by the imperfections caused by the camera lens. These defects are mainly caused by the monochromatic lens aberrations (widely known as five Seidel aberrations), which consist of spherical aberrations, coma, astigmatism, curvature of field, and distortion [215]. Here, we propose a novel technique to mitigate the error induced by the aforementioned lens distortions at the Rx by generating an ellipse-shaped mask $\mathbf{M}_{U \times V}$ prior to finding the centroids. $\mathbf{M}_{U \times V}$ is formed using a single binarized frame to maximize the efficiency of

the algorithm, in which, the intensity value of the pixels within the ROI is set to be high, i.e., “1”, whereas the residual pixels within the frame are assigned a low value of “0”.

The generated mask is then multiplied with the image to eliminate the out-of-ROI noise, which is given as:

$$\mathbf{F}_{U \times V}^{m,k} = [f^{m,k}(u, v)]_{U \times V} = \mathbf{F}_{U \times V}^k \odot \mathbf{M}_{U \times V}, \quad (4.4)$$

where \odot is the matrix multiplication operator. Note, the variation of CoC size after a distance (depends on the focal position and the lens size) is insignificant [216].

In addition, the quality of the received image is evaluated in terms of the peak signal-to-noise (PSNR), which is given by [217]:

$$\text{PSNR} = 10 \log \frac{I_{\max}^2}{\text{MSE}}, \quad (4.5)$$

where I_{\max} represents the maximum possible pixel value ($I_{\max} = 255$ for the 8-bit grayscale image data value), and MSE is the pixel luminance mean squared error, which is defined by [16]:

$$\text{MSE} = \frac{1}{n} \sum_{j=1}^n (I_{\text{Tx}}(j) - I_{\text{Rx}}(j))^2, \quad (4.6)$$

where I_{Tx} are the pixel values for transmitted symbols. Note, here we have obtained I_{Tx} from the captured images at the lowest captured exposure, i.e., the exposure value (EV) of 1/4000). I_{Rx} is the average pixel values for the received symbols, n is the number of rows (i.e., the on and off states of the Tx for the OOK signalling format), and j is the pixel's row index number.

4.2.4 AoA- based IS Measurements

The relationship between the image distance p and the distance between the Tx and the lens x is described based on the thin lens formula and the focal length f and is defined as:

$$\frac{1}{f} = \frac{1}{x} + \frac{1}{p}, \quad (4.7)$$

where f is in the order of millimetres, and the Tx is placed on the ceiling with the height in meters, thus $d_0 \gg f$ and $d_i \approx f$.

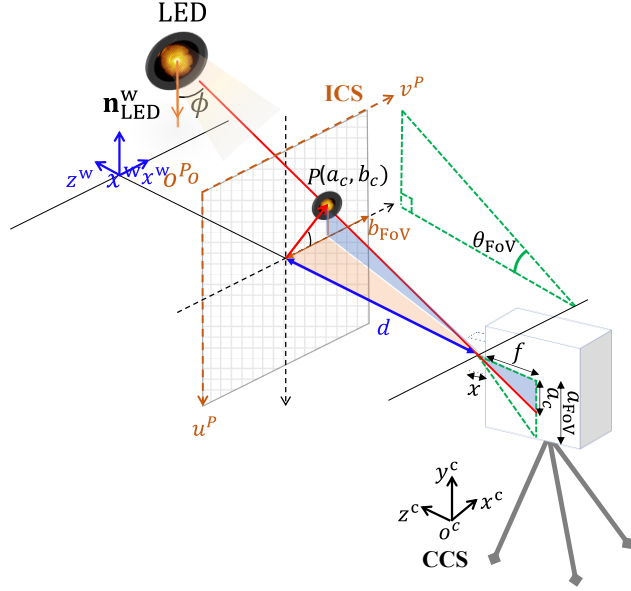


Figure 4-2. The geometrical model for the proposed system.

Figure 4-2 shows a projection of a simple light source located at a center point of (a_c, b_c) with respect to image coordinate system. The measurement of the relative AoA is highly dependent on measurements of both the FoV and f of the IS. Measurements of two referenced points are required to estimate the FoV of the utilised sensor prior to the estimation of AoA, which is given by:

$$\tan(\theta_{\text{FoV}}) = \frac{b_{\text{FoV}}}{p} = \frac{a_{\text{FoV}}}{f} = \frac{b_{\text{FoV}}}{d + x}, \quad (4.8)$$

where b_{FoV} denotes the half FoV of the vertical frame resolution. Note, p is $(d + x)$, d represents the distance between the light source and pupil entrance of the camera and x (the equivalent distance between the lens and the pupil entrance of the camera). a_{FoV} is the distance between the LED projection centre and the centre of IS plane.

The AoA of the incident light is quantified by the polar angle θ and the azimuthal angle φ in the camera coordinate, which is a coordinate frame attached to the lens and is defined as:

$$\tan(\theta_{\text{AoA}}) = \frac{a_c}{a_{\text{FoV}}} \tan(\theta_{\text{FoV}}). \quad (4.9)$$

4.3 Results and Discussion

The proposed low complex and highly accurate AoA-RSS-based VLP system is evaluated using an experimental platform as depicted in Figure 4-3. The set-up involves a robotic arm fitted with a camera (i.e., the Rx), and the optical Tx with a current driver and arbitrary function generator. First, we investigate the EV impact on the Tx ROI detection and P_r . Next, the 3D root mean square error (RMSE) of the proposed system is measured by changing the Rx's positions in all directions. Note that, the Rx's position is changed by moving the computer-controlled robotic arm with an accuracy of 0.1 mm [218]. All the key system parameters are shown in Table 4.2.

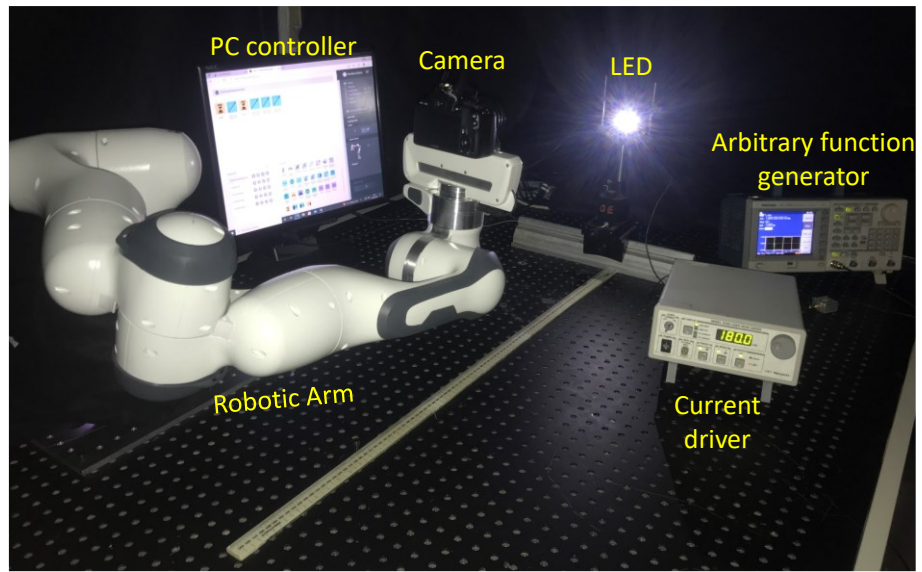


Figure 4-3. A photograph of the experimental setup of the proposed AoA-RSS-based VLP system.

Table 4.2 System parameters.

Parameter		Value
LED Tx	<ul style="list-style-type: none"> - Type - Bias current - Signal bandwidth 	Rebel star white LED CW100) 180 mA 220 Hz
Camera Rx	<ul style="list-style-type: none"> - Model - Exposure value (EV) - Frame rate - F-stop - Flash mode - Focal length - Height - Tilt angle - Pixel area - Image sensor area - Raw image resolution 	Canon Rebel SL1 EOS 100D 250 μ s to 4 ms 30 f/22 No flash 55 mm 24 cm 0 ° 18.4 μ m ² 22.3 \times 14.9 mm ² 5280 \times 3456 pixels
Channel	Length	0 to \approx 2 m
Robotic arm	<ul style="list-style-type: none"> - Model - Power use - Weight - Precision - Maximum distance: .Sides .Top .Below ground level 	Franka emika robotic arm 80 W 18 Kg 0.1 mm \approx 850 mm 1190 mm 360 mm

4.3.1 The Exposure Time Impact on ROI

The exposure time is investigated initially with respect to the ROI detection, where the CHT algorithm is applied as described in Section 4.2. Several transmitted frames are captured at the Rx for different EV values within 250 μ s to 4 ms and over a fixed channel length.

Figure 4-4 depicts the captured ROI for a range of EV, in which the statistical data for the radius, centre row and column were determined and indicated in Figure 4-4. The detected ROI at the captured $\mathbf{FkU}_{\times V}$ for a range of EV in the image domain.

Table 4.3. Next, the CHT is applied to detect Tx's ROI prior to the RSSI measurement. Using Eqs. (1-3), the RSS measurements are carried out for different EVs, in which, the P_r at each pixel within the ROI is aggregated to determine RSS. For instance, the intensity profiles for F-stop of f/3.5 and different EVs for the entire image and the ROI detected regions are depicted in Figure 4-5 (a) and (b), respectively. Note, (i) the summation of pixel intensities within the ROI indicates $\mathbf{F}_{U \times V}^k$ values; and (ii) the increase in EVs lead

to an additional gain in the received signal as well as more noise outside the ROI region, see Figure 4-4.

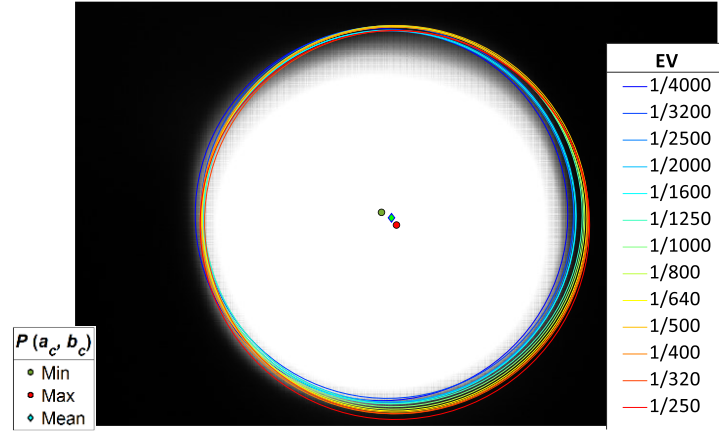


Figure 4-4. The detected ROI at the captured $\mathbf{F}_{U \times V}^k$ for a range of EV in the image domain.

Table 4.3 The data for the detected ROI from Figure 4-4.

	Min (px)	Max (px)	Mean (px)	Std (px)
Radius of ROI	330.00	345.00	336.53	5.76
Centre row (x -axis, a_c)	2769.05	2795.60	2786.80	7.46
Centre column (y -axis, b_c)	1857.80	1880.30	1867.50	5.92

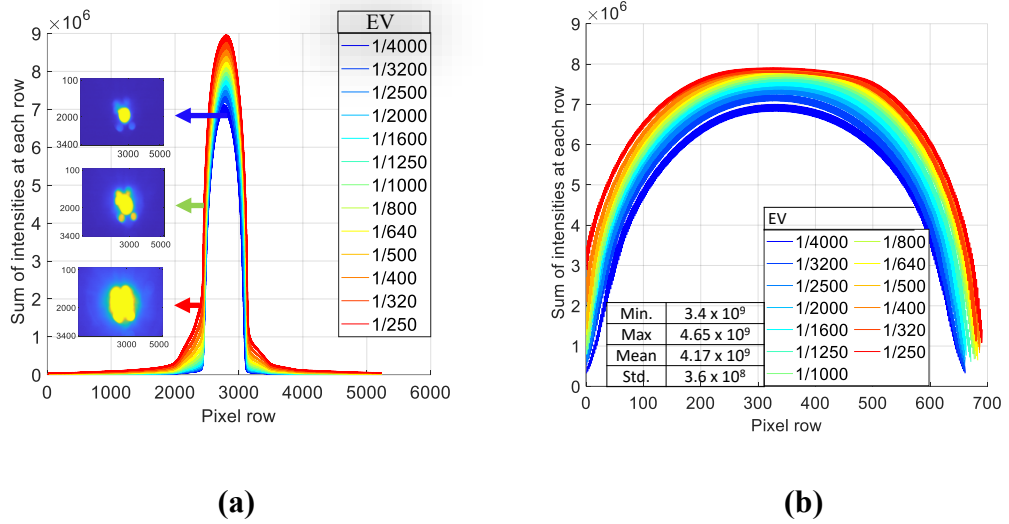


Figure 4-5. The intensity profiles versus the EV for the captured images and F-stop of $f/3.5$ for: (a) entire image, and (b) the ROI detected region ($\mathbf{F}_{U \times V}^k$).

Figure 4-6 shows the PSNR as a function of EV for the entire frame and the detected ROI with the former showing much higher PSNR for the entire range of EV. As illustrated, the recorded PSNR exponentially decreases with EV for both cases. E.g., at a

EV of 250 μ s the PSNR values are ~ 50 and 34 dB for the entire frame and the detected ROI, respectively dropping by 11 dB at the EV of 4 ms for both cases. Next, the generation of the ellipse-shaped mask $\mathbf{M}_{U \times V}$ is implemented as described in Section 894.2.3.

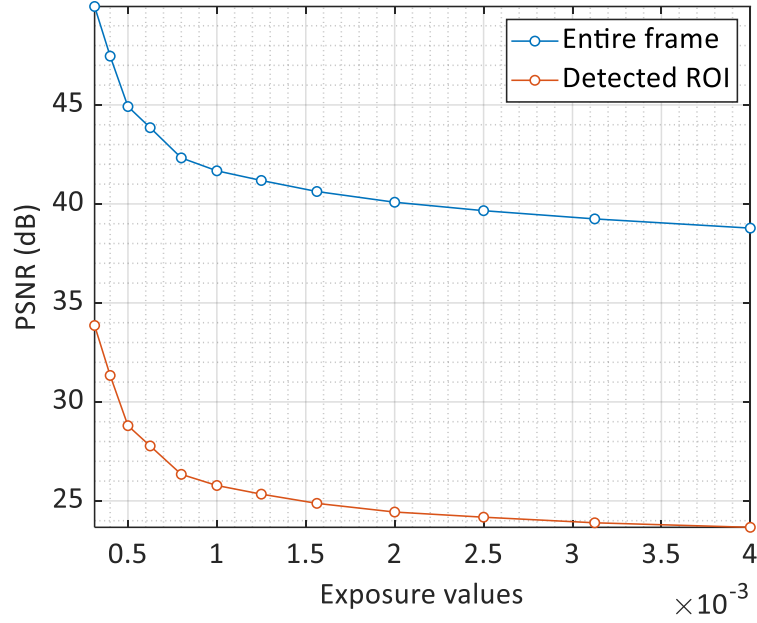


Figure 4-6. The PSNR as a function of EV for the entire frame and the ROI detected region.

An example of the standard captured source at the Rx (i.e., $\mathbf{F}_{U \times V}^{m,k}$) with and without the proposed method for the conventional $\mathbf{F}_{U \times V}^{m,k}$, generated binarized ellipse-shaped mask $\mathbf{M}_{U \times V}$, and the output frame ($\mathbf{F}_{U \times V}^k \odot \mathbf{M}_{U \times V}$) are depicted in Figure 4-7. It is noted that, the elliptical shape of the conventional $\mathbf{F}_{U \times V}^{m,k}$, which occurs due to the monochromatic aberrations, is eliminated as compared with the output frame ($\mathbf{F}_{U \times V}^k \odot \mathbf{M}_{U \times V}$), see Figure 4-7 (a and c). To estimate the impact of the proposed technique on the EV, the normalized P_r for the conventional method (w/o the $\mathbf{M}_{U \times V}$) is measured and compared with the proposed scheme, see Figure 4-8. As illustrated, P_r increases exponentially with respect to EV values, reaching the saturation levels at EV values of 1 and > 3 ms for the proposed and conventional schemes, respectively. E.g., at the EV of 250 μ s, the proposed scheme offers a power improvement by ~ 15 % compared with the conventional case. Thus, demonstrating the practical use of the proposed VLP system under different environments where the impact of EVs variations on the estimation of P_r is insignificant.

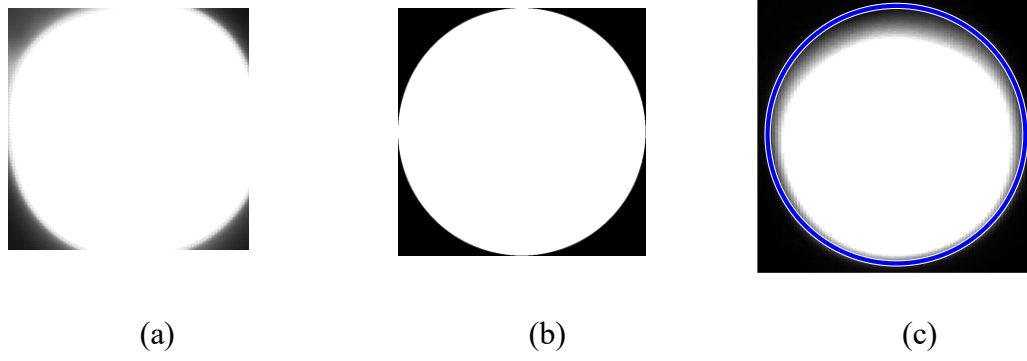


Figure 4-7. The captured frame with and without the proposed method for: (a) conventional $F_{U \times V}^{m,k}$, (b) generated ellipse-shaped mask $M_{U \times V}$, and (c) the output frame ($F_{U \times V}^k \odot M_{U \times V}$).

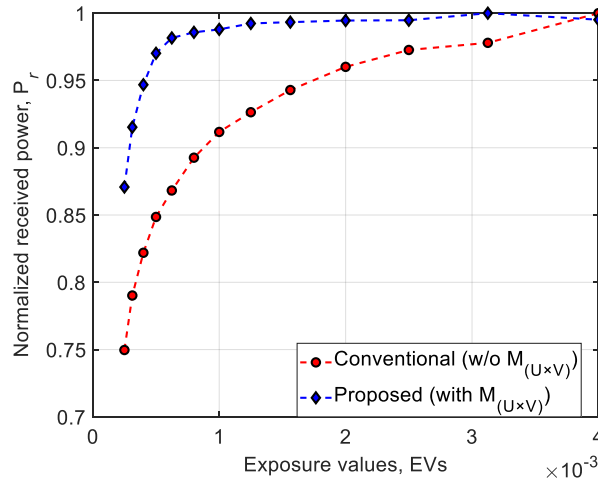


Figure 4-8. The normalized received power versus the EV for the conventional and proposed systems.

4.3.2 The Accuracy of the Proposed VLP system

Two reference points are considered to estimate the FoV of the IS used in this work with the captured images taken at distances of 0.27 cm, and 1 m. Using (4.8), the computed FoV of both horizontal and vertical axes are 25.46° and 16.94° , respectively. The AoA is then measured at different depths in order to evaluate the accuracy of the proposed system. Figure 4-9 shows the comparison between real and estimated coordinates of the Rx as it moves along the: (a) x , (b) y , and (c) z axes. The overall 3D average error for the Rx travelling along the x -axis (i.e., both the y - and z -axes set to 0 and 88 cm, respectively) is 4.35 cm. As illustrated in Figure 4-9 (b), this process is repeated for the Rx travelling down the y -axis (i.e., x - and z -axes set to 0 and 88 cm, respectively), with a recorded mean error of 5.5 cm from all directions. Ultimately, the depth of the system is measured as depicted in Figure 4-9 (c), where the recorded mean errors from all directions are 5.49 and 2.85 cm, respectively.

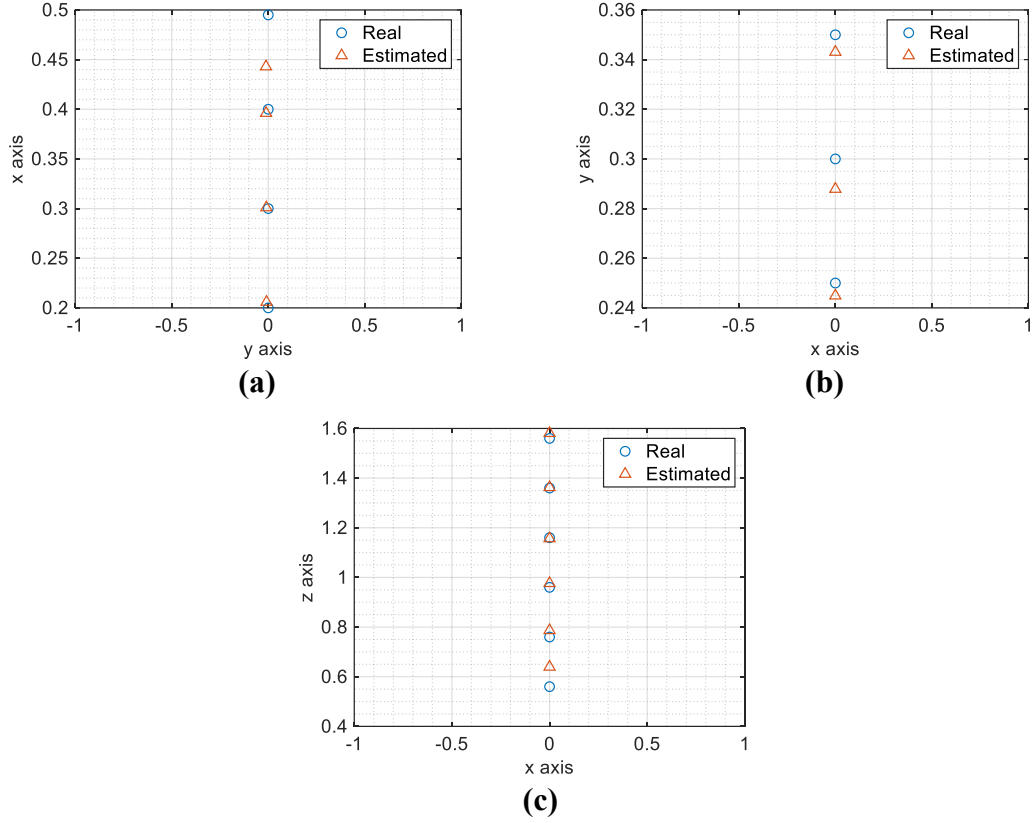


Figure 4-9. The comparison between the real and estimated 3D position of the Rx when moving along: (a) x-axis ($y = 0$; $z = 88$ cm), (b) y-axis ($x = 0$; $z = 88$ cm), and (c) z-axis ($x = 0$; $y = 0$).

4.4 Summary

In this work, a low complex and highly accurate AoA-RSS-based VLPs system using a single LED and an IS was introduced. A novel technique was proposed to mitigate the error induced by the lens at the receiving side, hence, leading to reduced positioning errors. The results showed that the proposed method offers immunity (i.e., power improvement by ~ 15 %) against different exposure times within the standard range of $250 \mu\text{s}$ to 4 ms , as well as outperforming the RSS method in all circumstances and AoA reported previously. The experimental results demonstrated that a 3D RMSE of 7.56 cm was achieved using the proposed algorithm. Furthermore, the impact of the exposure time on the detection of the Tx's location was investigated.

Chapter 5

Artificial Neural Network Equalizer

5.1 Introduction

There are two type of optical receivers commonly used in VLC systems: (i) PDs; and (ii) ISs [16], [162], [219]. The former is low cost and has higher bandwidth (or large detection areas). The latter, which is composed of a large number of PDs (i.e., pixels) aligned orthogonally, offer both multi-input multi-output capabilities and large detection areas but with complex data processing. Advances made in handheld smart devices have triggered the use of off-the-shelf conventional CMOS ISs for cameras. These devices can be used as an inherently Rx module in OCCs, which can capture light signals from a range of sources (i.e., LED-based traffic light, signage, headlights, vehicle tail lights, etc.) [16]. Moreover, in IS-based VLC systems the signal to noise ratio is independent of the transmission distance [46]. Note, as long as the projected image of the transmitting LEDs cover a number of pixels, the incident light power level per pixel remains unchanged. However, the drawbacks of ISs-based Rx are low transmission bandwidth due to the camera frame rate R_f limitations and higher costs compared with PDs [35]. The maximum data rates of conventional commercial cameras are relatively low within a range of a few kbps, which are sufficient for non-data communications related applications such as device to device communications, sensing, and health care [37]–[44].

In [37], a data rate of 15 bit/s was demonstrated using an UFSOOK and a 30 frames-per-second camera. The data rate increased to 150 bps using UPSOOK, two LEDs, and a 50- frames-per-second (fps) camera [38]. In [39], a data rate of 150 bps was achieved using a red-green-blue (RGB) LEDs and a 50-fps in an IS-based VLC link. Alternatively, mobile-phone based VLC with a beacon jointed packet transmission scheme with RS was deployed with a data rate and R_f of 10.3 kbps and 60 fps for a link distance of 20 cm [40].

A colour-shift keying (CSK) modulation scheme was adopted for RGB LEDs based VLC and OCC offering data rates of 240 bps, 5.2 kbps and 8.64 kbps (i.e., 288 bit/frame

with a R_f of 30 fps), respectively [41], [42], [44]. In [43], both data rate and packet size enhancement were employed in IS-based communications with 4-PAM to achieve a data rate of 3.6 kbps. Whereas in [220], [221], an OCC link with RS-based multilevel phase and amplitude modulation with the LED lights having spatial luminance distributions was investigated with data rates of 80, 78.5 bps for 256- and 64-QAM, respectively with R_f of 30 fps. The use of equalisation techniques is adopted to compensate spatial and time dispersions in the OCC system. In [222], a double-equalisation was investigated for a single white LED. The 1st equaliser used a frame averaging based signal tracing algorithm to extract the signal with nearly constant grayscale, while the 2nd scheme is an adaptive least mean square-based FFE, where the data rate achieved was 14.37 kb/s at R_f of 60 fps.

Additionally, different approaches can be adopted to improve the data rates in OCC with CMOS-based ISs including (i) high-speed cameras, which are highly costly and with limited applications; (ii) multiple transmitters, which may suffer from flickering [45]; and (iii) a special IS with a built-in PIN PD array has been used to increase the data rate to 55 Mbps using an optical orthogonal frequency division multiplexing [46]. However, the fabrication process of this IS is too complex and not commercially available. In contrast, the RS technique offers high-speed data transfer and has been widely adopted in OCC [223]–[226]. The concept of a 9.6 kbps VLC link using multiple TxS i.e., an array of 8×8 LEDs and an IS of a resolution of 320×240 with R_f of 30 fps was adopted in [227]. However, providing high capacities still imposes a number of challenges, which needs addressing [228], [229], including sampling rates, frame resolution image distortion factor and detection speed of the transmitted light source.

The sampling rate corresponds to exposure time T_{exp} i.e., the time where IS is exposed to the light. Increasing T_{exp} allows more lights to be integrated by the IS and increases the noise level, which is the key parameter in determining the bandwidth (i.e., T_{exp} acts as a temporal low pass filter (LPF) where it takes an average over a period of time. If the changes in the scene are faster than the bandwidth of the camera induced by the exposure time, the scene will be blurred).

ANNs as universal classifiers are used in VLC systems, the use of ANN is deployed for each channel in MIMO VLC [230]. In [231], an ANN-based equaliser was deployed in a fully connected mode to reduce the effect of the inter-symbol interference in a NLoS or

diffuse VLC link in indoor environment. It is also deployed in OCC systems to compensate for the data loss by reducing the gap-time between observed frames [232], [233]. Unlike previous studies, in this chapter, for the first time, we propose and implement an ANN-based equaliser to mitigate the ISI induced by high sampling duration within the observed frame in OCC, and hence increase the transmission data rate.

The ANN network is trained only once for a range of T_{exp} and can be stored in a look-up table. We have developed an experimental test-bed for the proposed system for evaluating its performance in terms of the data rate, BERs and eye diagrams. In addition, we investigate a number of training methods and show that, the resilient back-propagation algorithm offers the best performance with a trained mean square error value of 9.29×10^{-5} . We have also achieved the highest data rate in OCC using a single white LED source, the manchester line code (MLC) NRZ encoded signal at the transmitter, an image sensor with R_f of 30 fps and an ANN-based equaliser at the receiver. The achievable bandwidth is also increased by approximately 9, 5, and 2 times for T_{exp} of 2, 1 and 0.5 ms, respectively compared with the existing reported systems [37].

The remainder of the chapter is organised as follows: Section 5.2 introduces the CMOS IS model for the OCC system. In Section 5.3 the proposed ANN-based post-equaliser is outlined, while in Section 5.4 the system model is presented. The numerical results are presented and commented in Section 3.5. Finally, section 5.5 draws the final conclusion.

5.2 CMOS IS Modelling in OCC System

In CMOS ISs with RS, an array of pixels is used to capture the incident light in a progressive manner by exposing each row (column) of pixels as illustrated in Figure 5-1 (a). In RS-based cameras, the incident light at high frequencies and a relatively low exposure time is observed by forming different illuminated bands indicating the “ON” or “OFF” status of the incident signal for OOK-NRZ at T_{exp} , or the intensity level at other modulation schemes, while light cannot preserve any signal during the resetting time T_{rst} and the readout time for a given row. The standard IS-based Rx is modelled as a linear shift-invariant (LSI) system, which is composed of two stages as depicted in Figure 5-1 (b). The voltage at a pixel (U, V), which corresponds to an individual photodiode, is given by [232]:

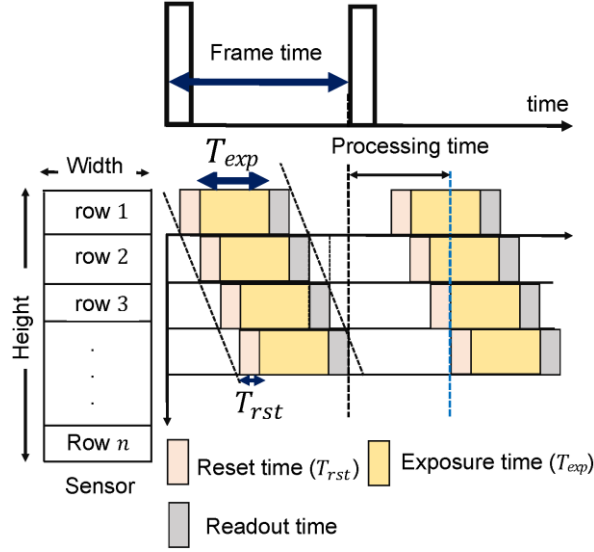
$$v_r(t) = \frac{A}{C_{PD}} \int_{t-T_{exp}}^t \Re. x(t) dt, \quad (5.1)$$

where A is the gain (set to unity for simplicity), C_{PD} and \Re are the equivalent capacitance and responsivity of the PD, respectively and $x(t)$ is the received optical signal at the pixel (U, V) at time t . Note, $T_{exp} \geq T_{sym}$, where T_{sym} is the symbol period [234]. The number of symbols observed at the Rx depends on the resolution of the IS, exposure time, pixel clock, and the size of the region of interest [35]. The system response is given by [235]:

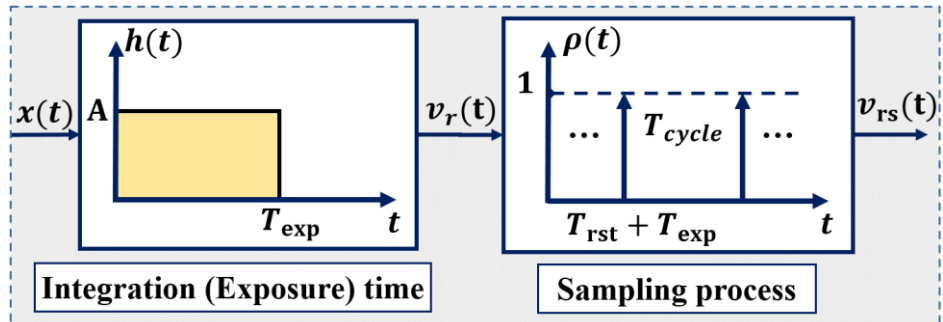
$$h(t) = \frac{A}{C_{PD}} \left(u(t) - u(t - T_{exp}) \right), \quad (5.2)$$

where $u(t)$ is the unit step function. Integration of the input signal over T_{exp} results in a finite impulse response (FIR) LPF effect with a transfer function given as [235]:

$$H(f) = \mathcal{F}\{h(t)\} = \frac{A T_{exp}}{C_{PD}} \frac{\sin(\pi f T_{exp})}{\pi f T_{exp}} e^{-j\pi f T_{exp}}. \quad (5.3)$$



(a)



(b)

Figure 5-1. (a) An example of the frame acquisition based on rolling-shutter CMOS sensor. (b) The LSI model of a CMOS image sensor receiver.

The DC gain is proportional to T_{exp} , therefore a trade-off between the gain and the required bandwidth, where increasing T_{exp} will reduce the cut-off frequency. Following sampling, the discrete signal is given by [232]:

$$v_{rs}(kT_{\text{cycle}}) = v_r(t) \sum_{k=n-T} \delta(t - kT_{\text{cycle}}) + n(t), \quad (5.4)$$

where $\delta(t)$ is the Dirac delta function, T_{cycle} is the sampling period and $n(t)$ is the noise (i.e., signal-induced shot noise, ambient light induced shot noise and the thermal noise), which is modelled as zero-mean additive AWGN.

5.3 Artificial Neural Network Equaliser

In RS-based OCC systems, the bandwidth limitation imposed by the sampling process of IS (i.e., LPF) results in ISI at higher data rates, thus leading to a significant degradation in system performance. The slow rise-time of the detected symbol is affected by the existence of the transition between different illumination levels, see Figure 5-2. Generally, a matched filter is adopted to mitigate ISI, however if this is not sufficient equalisation can be used to enhance data rates by estimation and mitigating the ISI effect [236]. Equalisation can be viewed from (i) the information theory, where ISI is predicted by the training filter coefficients based on a training sequence in order to minimise the error cost; and (ii) classification, where class decision boundaries are created in order to classify symbols based on training. The key difference between the two is that the former allows generalisation because of the use of boundaries, where unknown symbol transitions can be tolerated.

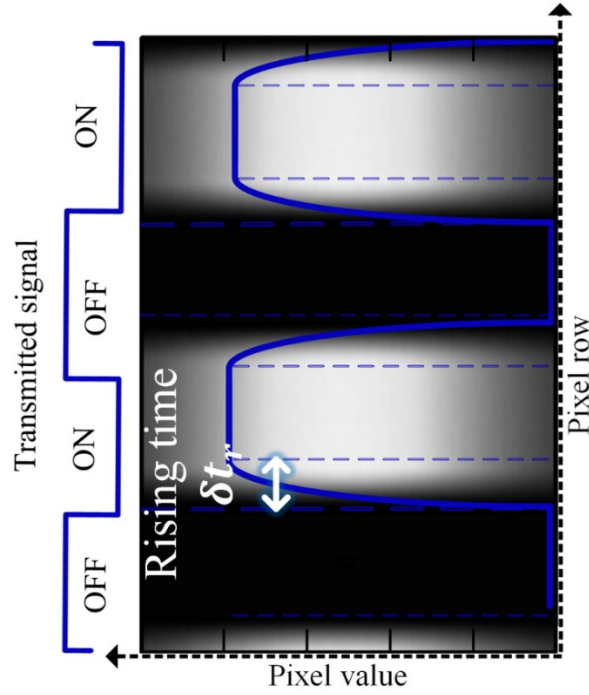


Figure 5-2. An example of the frame acquisition based on the RS CMOS sensor.

Linear decision boundaries are not sufficient to provide an optimal decision in practical channels, where the threshold boundaries are nonlinear. Therefore, ANN-based equalisers with the realisation of nonlinear decision boundaries offer improved performance in communication systems [230]. The classification and regression models are categorized as a sub-section of supervised machine learning. The main difference between regression and the classification is that the output variable of the formal one is numerical (or continuous) whereas is categorical (or discrete) for the latter one [237]. Note, the boundaries have a high dependency on the number of neurons and the hidden layers, which are analogous to the human brain, where the synaptic weight is changed based on the training sequence. Different ANN approaches can be deployed for equalisation including the single-layer [238] and the Multi-layer perceptron (MLP) [236]. In [231], it was shown that, MLP offers superior performance in mitigating ISI in optical wireless systems and hence, has been adopted in this work.

The ANN-based equaliser includes input layer, variable number of hidden layers ($M - 1$) and output layer. The neuron (k) in the MLP filter in layer (m) receives N_{m-1} tapped delay inputs $[o_1^{(m-1)}, o_2^{(m-1)}, \dots, o_{N_{m-1}}^{(m-1)}]$, known as the observation vector. The N_{m-1} tapped delay inputs are considered to study the impact of N previous samples on the desired sample. The n^{th} input has a corresponding weight connected to the k^{th} neuron

$w_{kn}^{(m)}$. Note, $N = \frac{T_{\text{exp}}}{T_{\text{sample}}}$, where T_{sample} is the sampling duration which depends mainly on the pixel clock. The neurons represent the functional unit of the ANN, and are represented by a transformed version of the summed weighted inputs. The output is added to a constant offset value $C^{(m)}$, which is weighted with the threshold factor $v_k^{(m)}$ to estimate the output $o_k^{(m)}$ of the neuron k using a non-linear function $f(\cdot)$, given by [236]:

$$o_k^{(m)} = f\left(\sum_{n=1}^{N_{m-1}} w_{kn}^{(m)} o_n^{(m-1)} + C^{(m)} v_k^{(m)}\right). \quad (5.5)$$

By considering a $N_o \times 1$ input vector, and a $N_M \times 1$ output vector the estimation of the next observation vector $\mathbf{o}^{(m)}$ is required, where $\mathbf{o}^{(o)} = \mathbf{x}$, $\mathbf{o}^{(M)} = \mathbf{y}$, and given $\mathbf{x} = [x_1 \ x_2 \ \dots \ x_{N_o}^{(m)}]^T$, and $\mathbf{y} = [y_1 \ y_2 \ \dots \ y_{N_M}]^T$. Therefore, we have:

$$\mathbf{y} = f(\mathbf{W}^{(M)} \mathbf{o}^{(M-1)} + C^{(M)} \mathbf{v}^{(M)}). \quad (5.6)$$

The MLP record its trained information in the weights $w_{kn}^{(m)}$ and in the threshold factors $\mathbf{v}_n^{(m)}$, since $C^{(m)}$ is given as a constant for all layers (set as $C^{(m)} = 1, m = 1, 2, \dots, M$).

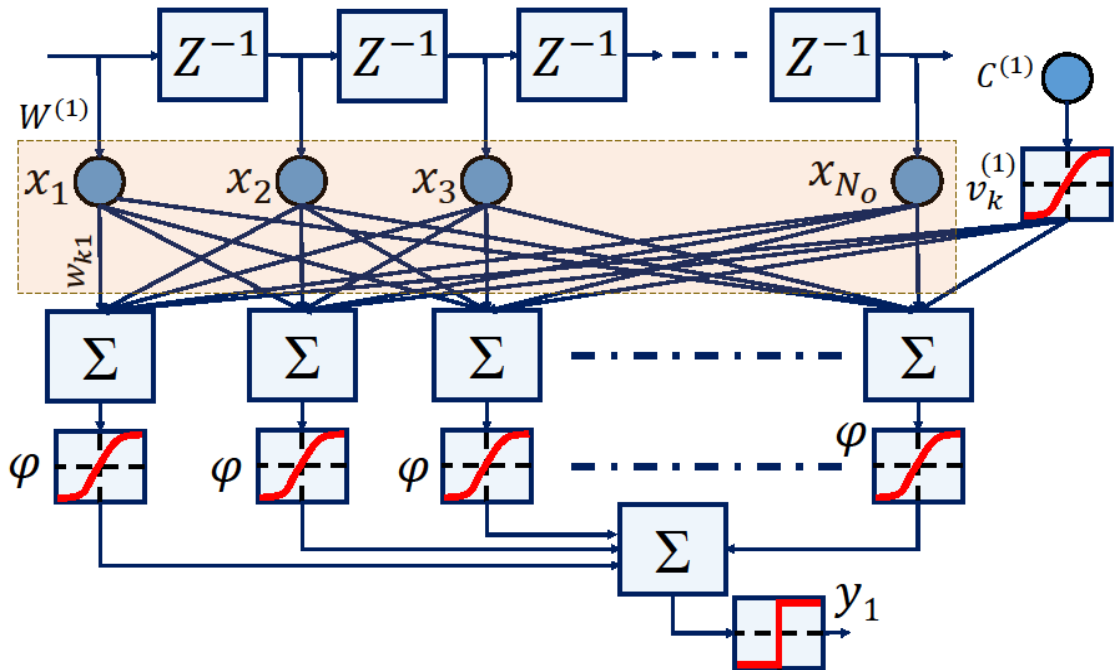


Figure 5-3. Block diagram of a single-hidden-layer ANN based equaliser.

With a suitable number of neurons, a single hidden layer ANN is recognised as a universal approximator. Figure 5-3 illustrates the block diagram of a single layer ANN-

based equaliser. The non-linear hyperbolic tangent sigmoid φ activation function is selected in this work since it provides a wider range for faster learning and grading, given by [239]:

$$\varphi = \frac{e^{\beta\xi} - e^{-\beta\xi}}{e^{\beta\xi} + e^{-\beta\xi}}, \quad (5.7)$$

where β is the slope factor (the standard unity value is assigned) and ξ is the weighted input.

ANN can be trained using supervised and unsupervised methods [240], [241]. Resilient back-propagation (RBP) is an advanced version of back-propagation, which has been adopted to train ANN in this work. RBP, considered as one of the best learning methods in ANN [242], takes into account the sign of the error gradient to designate the direction of the weight update, and hence overcoming the slow convergence of the standard back-propagation algorithm and reducing the level of training compared with other algorithms. The concept of RBP is similar to the regular backpropagation technique, where ANN adjusts the weight in order to minimize the error cost function E_n as defined by [236]:

$$E_k = ||d_k - y_k||^2, \quad (5.8)$$

where d_k is the ideal symbol value and y_k is the actual received value. RBP is an iterative operation, where the step size is dynamically adapted for each weight depending on a gradient descent of E_k . The updated weight is given by [243]:

$$w_{kn}(t+1) = w_{kn}(t) - \eta \frac{\partial E_k}{\partial w_{kn}}(t) + \mu \Delta w_{kn}(t-1), \quad (5.9)$$

where w_{kn} is the weight between the junction point of x_k and k^{th} neuron and η is the learning rate parameter.

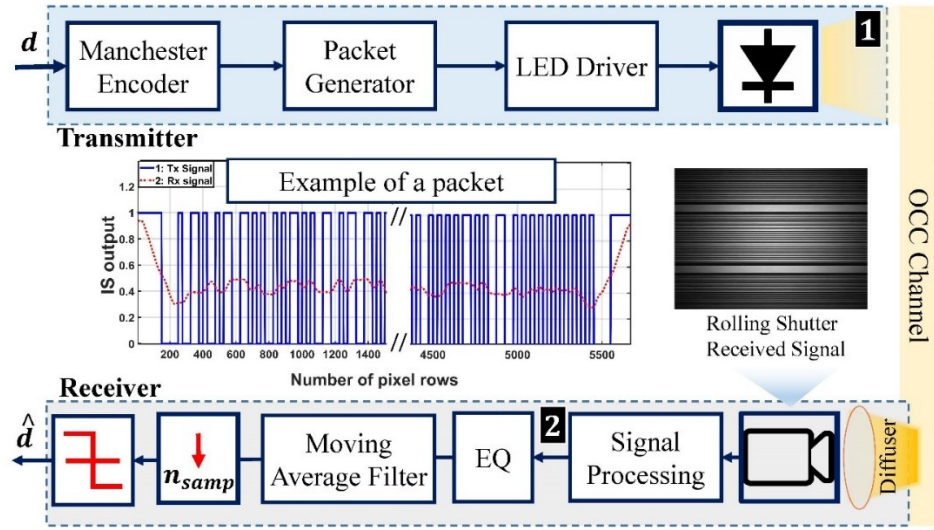
The momentum parameter μ scales the impact of the pervious step on the present one, thus introducing stability to the system and improving the convergence of the error function. Each weight has an individual evolving-value $\Delta w_{kn}(t)$, and the weight-step, which is only determined by its update-value. The sign of the gradient is given by [243]:

$$\Delta w_{nk}(t) = \begin{cases} +\Delta_{nk}(t), & \text{if } \frac{\partial E_k}{\partial w_{nk}}(k) > 0 \\ -\Delta_{nk}(t), & \text{if } \frac{\partial E_k}{\partial w_{nk}}(k) < 0 \\ 0, & \text{otherwise} \end{cases} \quad (5.10)$$

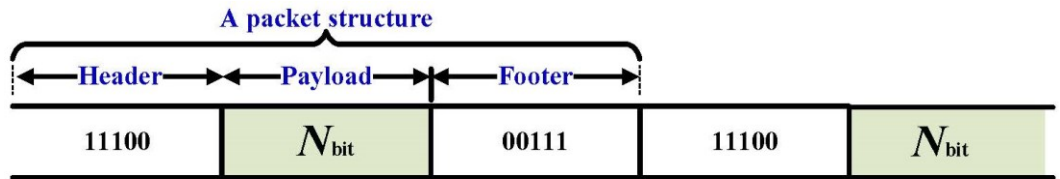
where $\Delta_{kn}(t)$ is the updated value. In order to provide a unity efficiency, the number of neurons is set to be similar to the number of tapped inputs [236].

5.4 Proposed System Model

The system block diagram of the proposed OCC system is illustrated in Figure 5-4 (a). The transmitter is comprised of a Pseudorandom binary sequence (PRBS) d with a length of $2^{14} - 1$ is generated in MATLAB, which is then up-sampled and encoded using the NRZ-MLC in order to avoid flickering and a unity amplitude rectangular pulse shaping filter. The MLC signal, which ensures a uniform distribution of 1 and 0 symbols and facilitates both decoding and synchronisation processes of the signal [234], is packetized in order to ensure proper detection at the Rx as illustrated in Figure 5-4 (b). Each packet consists of 5-bit header [11100], N_{bit} -bit payload and 5-bit footer [00111], which are used for intensity modulation of the LED via the optical driver.



(a)



(b)

Figure 5-4. (a) System block diagram for OCC using LED and rolling shutter CMOS sensor. (b) The proposed structure of data frame packet.

The pattern of header and footer is designed such that (i) it never occurs in the MLC pattern for the payload; and (ii) the transition from one packet to another is smooth,

which facilitates the training of the network. The transmitted optical signal over a free space channel is captured using a CMOS IS Rx. The link distance is set to 60 cm, which can be extended by increasing the intensity of light, having a clear available region of interest and using the lenses at the transmitter and the receiver. For example, increasing the optical transmit power from 1 to 4 mw will increase the transmission range by 100% [1]. A diffuser is utilised to distribute the captured light over the IS (i.e., the LED foot print was projected into the IS).

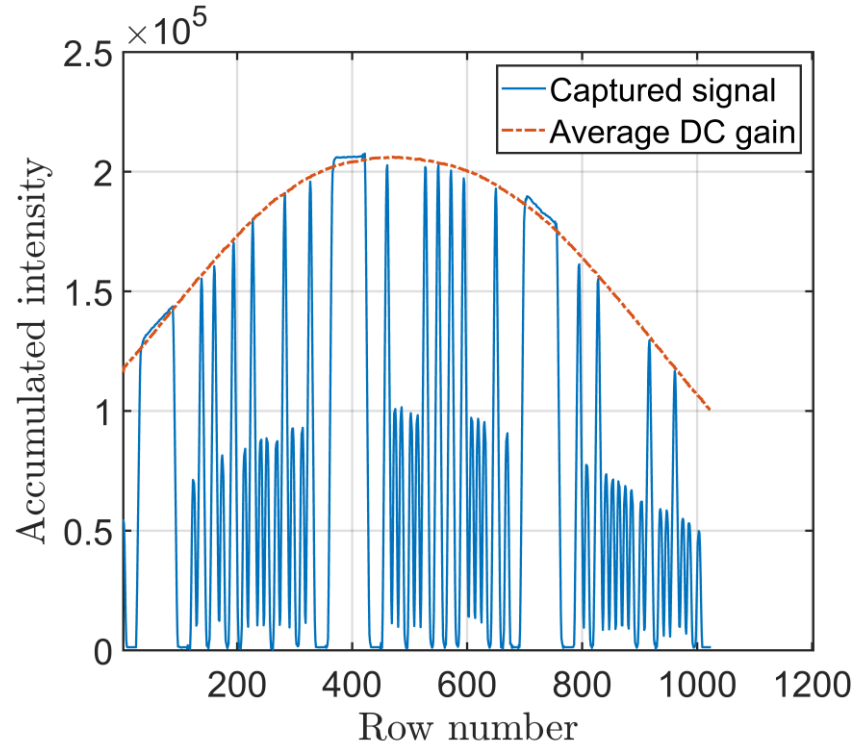
Algorithm 5-1 Signal extraction algorithm.

Input: RS captured image $\mathbf{P}_{U \times V \times 3}$ and 20 frame of illumination gain (DC signal only) $\mathbf{G}_{U \times V \times 3}$

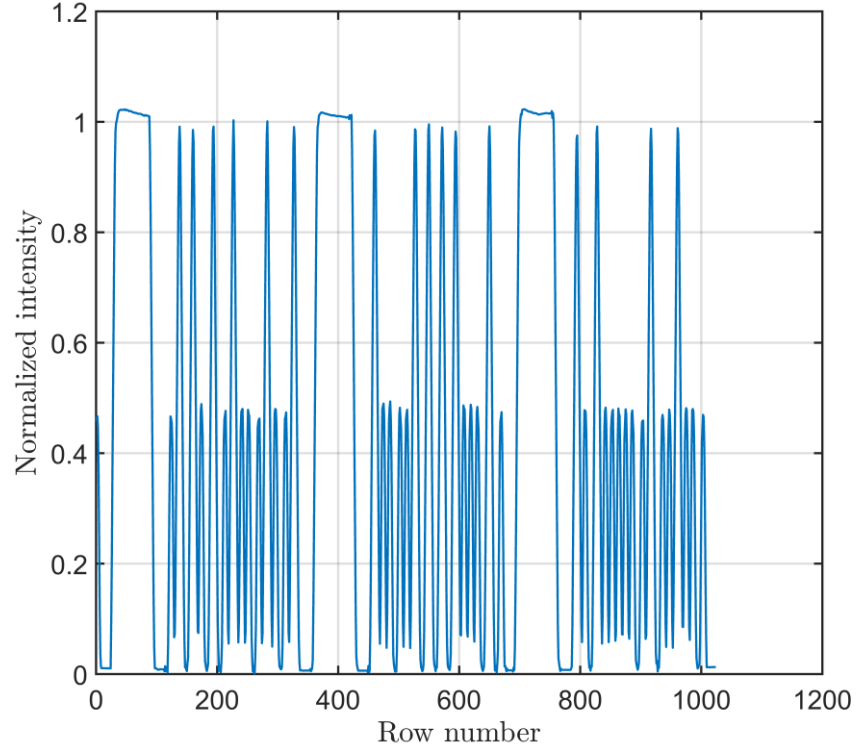
Output: The received signal is ordered the same as the transmitted signal

- 1 **foreach** Set of captured data frames $\mathbf{P}_{U \times V \times 3}$ **do**
- 2 Read $U \times V \times 3$ sized colour plaintext image $\mathbf{P}_{U \times V \times 3} = [P(i, j, c)]$. Let $F = U \times V$, and denote RGB components of $\mathbf{P}_{U \times V \times 3}$ as $\mathbf{RP}_{U \times V} = [RP(i, j)]$, $\mathbf{GP}_{U \times V} = [GP(i, j)]$ and $\mathbf{BP}_{U \times V} = [BP(i, j)]$, respectively. Where $i = 1, 2, \dots, U, j = 1, 2, \dots, V, c = 1, 2, 3$.
- 3 Convert the monochrome image to the grayscale image by calibrating RGB components $\mathbf{RP}_{U \times V}$, $\mathbf{GP}_{U \times V}$ and $\mathbf{BP}_{U \times V}$ together over 3, resulting $\mathbf{PS}_{U \times V}$.
- 4 Accumulate intensities for all pixels at each row $z = (z_i)_{i=1}^V$ where $z_i = \sum_{j=1}^V \mathbf{PS}_{U \times V}$.
- 5 Calibrate z with respect to the averaged DC value $z_{cal} = z / \overline{z_{DC}}$ where $\overline{z_{DC}} = \sum_{j=1}^V \mathbf{GS}_{i \times j}$ where \sum is the averaged DC.
- 6 Resample z_{cal} with respect to the packet length.
- 7 Locate the start of each packet in the frame.
- 8 Received packets are placed randomly within the captured frame due to the lack of synchronization between Tx and Rx, hence a correlation algorithm is adopted as follows: Create a filtered version of the ideal signal using a moving average filter $z[s] = \frac{1}{M} \sum_{m=0}^{M-1} y[s + m]$ where M is the window size (set to n_{smp}). Correlate the recieved signal with the filtered signal to find the correct sequence and change accordingly.

The RS received data is formed by accumulating intensities for all pixels at each row, since they are exposed to incident light at the same time. This increases the SNR of the signal by a maximum of V times, where V is the number of pixels in each row. The received signal strength forms the amplitude of the signal as explained in section II. The observed frames at the IS are first processed in MATLAB, where conversion to the grayscale is applied in order to eliminate the hue and saturation information while retaining the luminance of the image plane. Due to the non-uniformity of the illumination, the DC gain of the optical signal estimated from (3) is then measured to generate a calibration matrix. In order to mitigate the impact of noise, the calibration matrix is constructed by averaging over 20 frames of plain illumination, i.e., no AC signal. Note, none of the pixels of the region of interest in the calibration matrix should be over/under exposed, see Figure 5-5 (a & b). The signal extraction algorithm is shown in Algorithm 5-1.



(a)



(b)

Figure 5-5. The received signal at a signal bandwidth of 400 Hz with T_{exp} of 1 ms: (a) without DC gain normalization and (b) with normalization.

The frequency responses of the IS are first introduced for the conventional T_{exp} values of 0.5, 1 and 2 ms, which are also estimated using (3), where the frequency of the main lobe and the followed side-lobes is introduced in the following section. The main lobe indicates bandwidth available by means of 3 dB region (i.e., the cut-off frequency), whereas followed harmonics describe the rest of the magnitude spectrum. The harmonic frequency f_{sh} is used to specify the required bandwidth of the transmitted signal to ensure a minimum attenuation (i.e., at the peak of the side-lobes), where h is the harmonic number. Subsequently, a set of different signals are generated where N_{bit} -payload is varied with respect to f_{sh} in a way that ensures the capturing of three packets at every frame. T_{exp} is set to 2 ms and the values of selected N_{bit} are shown in

Table 5.1. In a typical scenario, the bandwidth of the transmitted signal should be less than or equal to the cut-off frequency f_c as highlighted in Section, whereas f_{sh} includes successive harmonics; The processed data is then applied to the proposed equaliser for different f_{sh} , and the quality of the transmitted signal is investigated in terms of the BER and the data rate.

Table 5.1 System parameters.

Parameter	Value
Image sensor	DCC1645C
Maximum SNR of IS	44 dB
Exposure time T_{exp}	0.5, 1, and 2 ms
Camera raw image resolution	1280×1024
Pixel clock	10 MHz
Camera frame rate R_f	30 fps
Link distance	60 cm
LED type	SR-01-WC310
Number of sample n_{samp}	50
Number of bit per frame N_{bit}	108 to 1170 bits
Activation function	Hyperbolic tangent sigmoid
Number of neurons in input layer	128 ($N_{\text{bit}} = 108$ bits), 250 ($N_{\text{bit}} = 192$ bits), and 1200 ($N_{\text{bit}} = 1170$ bits)
Number of neurons in output layer	1
Number of neurons in hidden layer	200
Number of hidden layer	1
Percentage of train to test	0.8
Maximum epochs	1000
Learning rate parameter η	0.01
Target BER	10^{-4}
Network training function	Resilient backpropagation Bayesian Regularization Polak–Ribière Conjugate Descent Scaled Conjugate Descent Conjugate Descent with Momentum

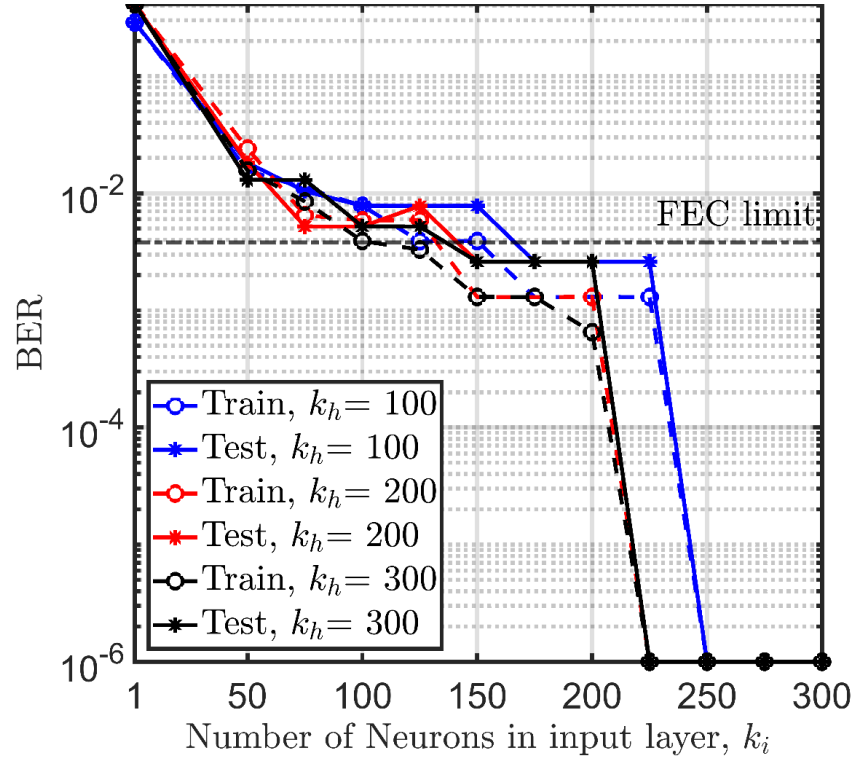
A moving average filter (i.e., comparing the energy of current per chip with the previous one) is employed to reduce the noise while retaining a sharp response by means of averaging the input signal y in order to produce a discrete signal (i.e., point) given by [244]:

$$z[s] = \frac{1}{L} \sum_{l=0}^{L-1} y[s + l], \quad (5.11)$$

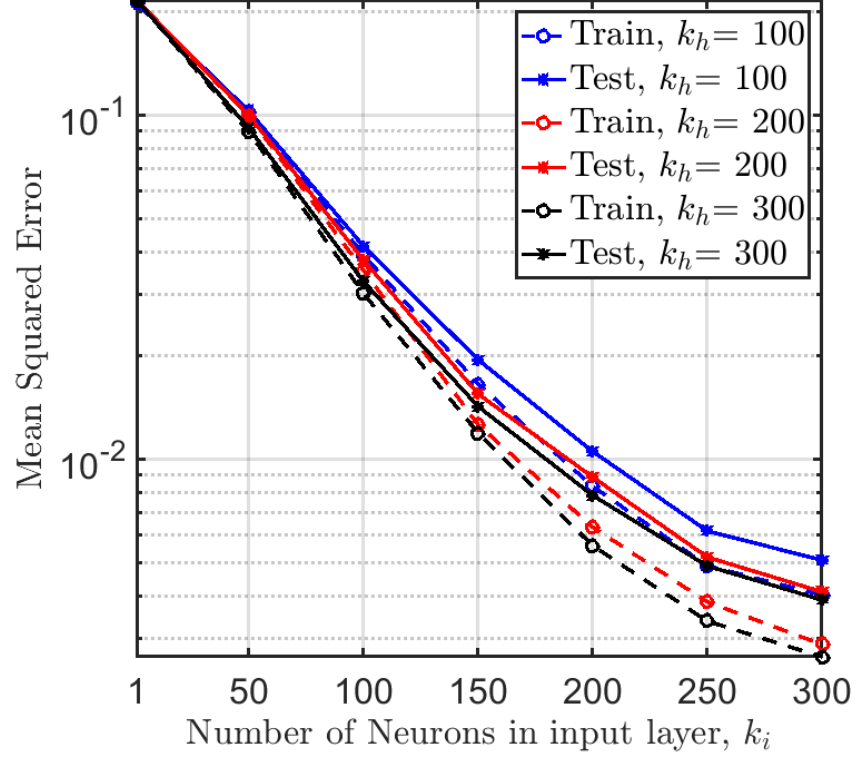
where L is the number of points.

The data is then down-sampled prior to thresholding to recover the estimated version transmitted signal. Finally, we have adopted different training algorithms in order to achieve the optimal results in terms of the BER and the convergence speed. For this, we

have used 80% of the data in the first frame for training, which corresponds to N_{bit} , and the number of bits used for training and testing is set based on N_{bit} per frame. For instance, for N_{bit} of 1170 bits, 80% (i.e., 936 bits) of the data is set to train the network while the rest (i.e., 20%, 234 bits) is used for consecutive testing purposes. Training is repeated every 10- N_{bit} since a set of 10 frames is considered for this purpose. The number of input neurons is set to be equal to the length of input patterns or vectors plus one, and the additional neuron being the bias neuron [245]. The optimal number of neurons is selected based on the experimental measurements of the BER and the MSE values. Figure 5-6 shows the BER and MSE as a function of the number of neurons in the input and hidden layer. At the FEC BER limit, the number of neurons at the input and the hidden layers are 250 and 100, respectively which correspond to the MSE values of $< 10^{-2}$ and 6×10^{-1} , respectively.



(a)



(b)

Figure 5-6. BER and MSE as a function of the number of neurons in input layer k_i , and the hidden layer k_h and N_{bit} of 192.

5.5 Results and Discussion

The system parameters used are shown in Table 5.1. Figure 5-7 shows the measured and simulated IS frequency response for a range of T_{exp} . The simulation is done through using MATLAB and based on the modelling introduced in section 5.2 and the equation (5.3). The measured (and simulated) 3-dB f_c are 811 (1020), 443 (443) and 250 (250) Hz for T_{exp} of 0.5, 1 and 2 ms, respectively. We have used the odd frequencies f_{sh} (i.e., 716, 1231, 1736 and 2240 Hz, see Figure 5-7 for generating MLC data formats). Note, we have used an average of 636 bps per frame, thus a total of 12 kbps for 30 frames in order to meet the forward error correction (FEC) BER limit of 3.8×10^{-3} .

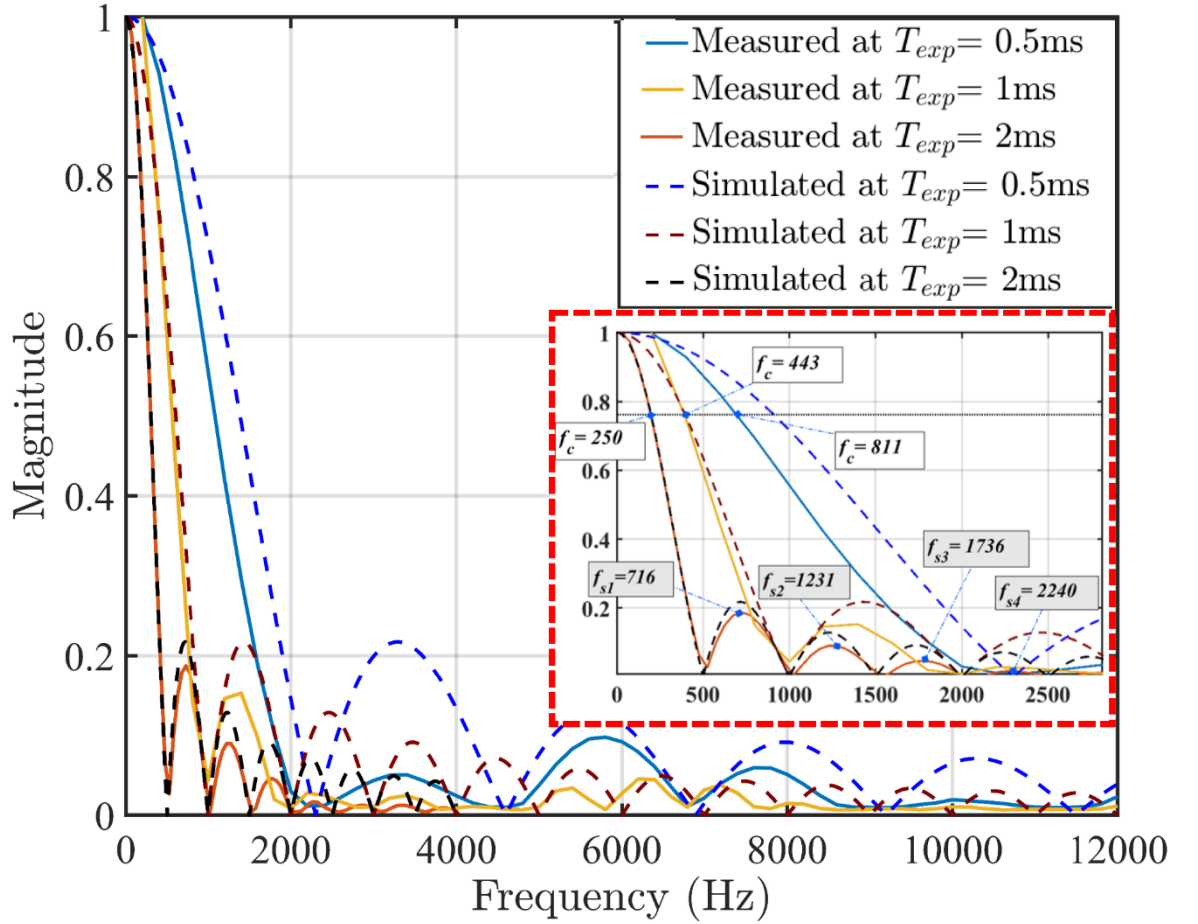


Figure 5-7. Image Sensor frequency response with different exposure time.

Next, the effective data rate of the system is evaluated following the methodology adopted in the previous section. The higher sampling rate is associated with the higher data rates used in this work. The BER as a function of the data rate for the system is initially measured prior to introduction of the proposed ANN equaliser as depicted in Figure 5-8. The proposed system demonstrates BER values below the FEC limit of 3.8×10^{-3} up to a data rate of 12 kbps for all three values of T_{exp} and a transmitted signal bandwidth of 2.275 kHz, which is around 9 times (for T_{exp} of 2 ms) higher the f_c of the unequalised system

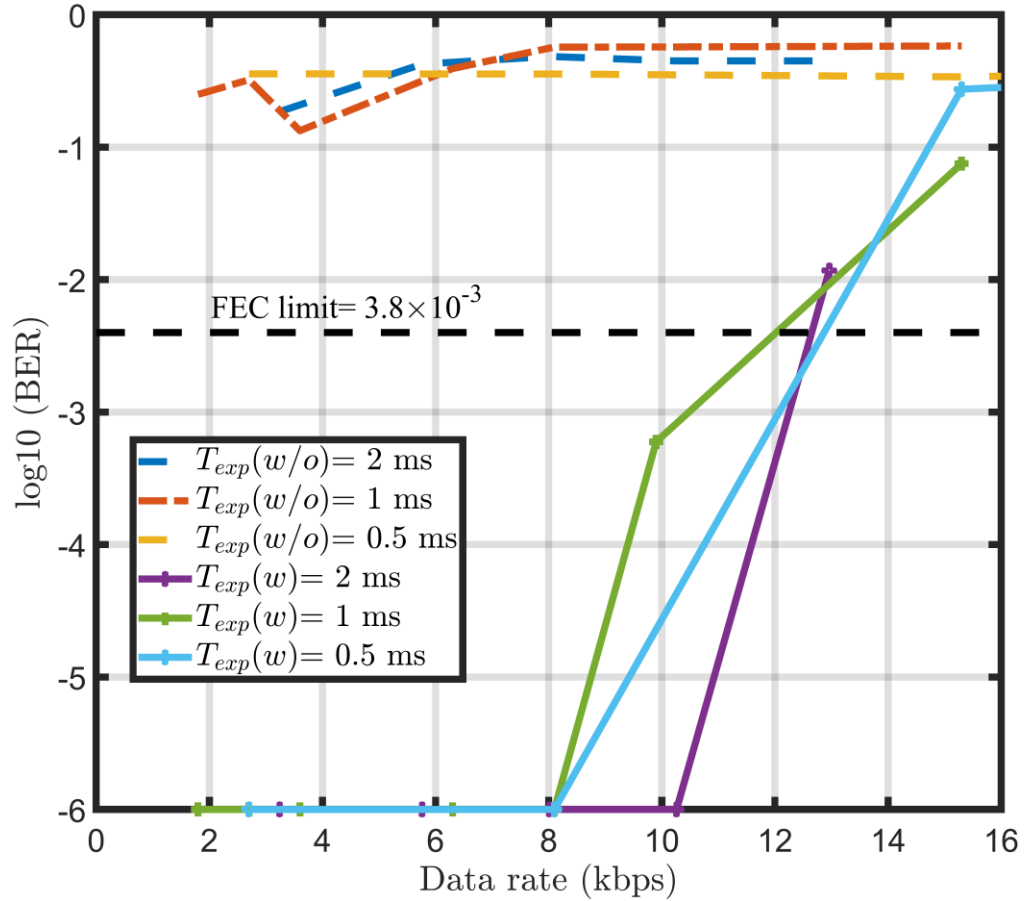
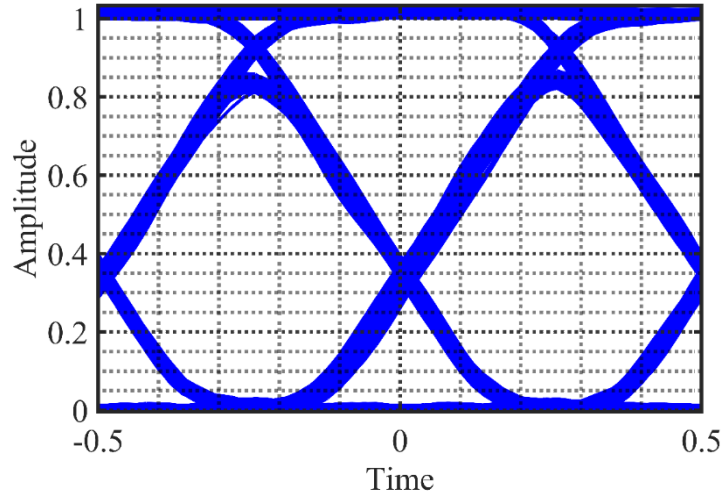


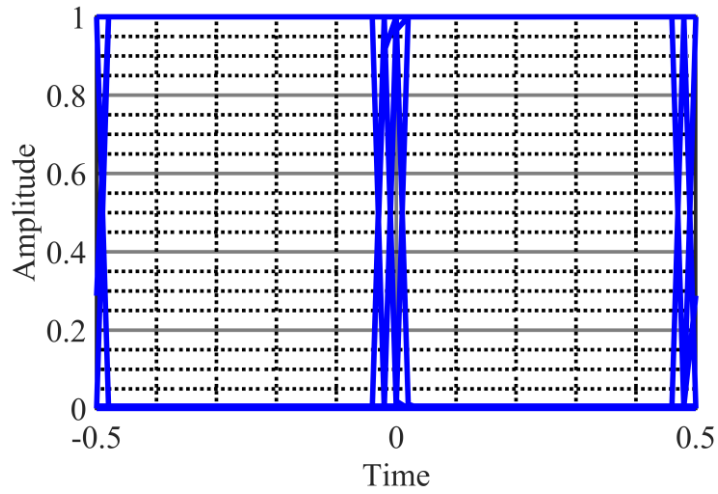
Figure 5-8. BER measurements of the system with and without equalisation in respect to effective data rates of different exposure times with R_f of 30.

The eye diagrams at T_{exp} of 2 ms without an ANN equaliser is illustrated in Figure 5-9 (a), where the received signal shows three levels of amplitude in spite of sending an OOK signal due to the ISI, which creates an additional level due to the transition delay in the status of the captured signal as explained in the previous section (Figure 5-2). However, with an ANN equaliser the eye diagram depicted in Figure 5-9 (b) shows significantly reduced ISI. Finally, we have evaluated the proposed system behaviour over time to determine the convergence time for different training algorithms for the hyperbolic tangent sigmoid activation function as illustrated in Figure 5-10. The system performance is measured based on the estimated MSE values, which is estimated between the equaliser outputs and the desired outputs. The ideal case is considered, where the channel is assumed to be noise-free, and hence the error in the equaliser outputs is solely due to the channel dispersion. As shown, the resilient backpropagation algorithm displays faster convergence compared with others and offers the best performance (the estimated trained mean square error value is recorded as 9.29×10^{-5}). The superiority of this algorithm is

due to magnitudes elimination of the partial derivatives where the sign of the derivative is merely utilised to estimate the direction of the weight update.



(a)



(b)

Figure 5-9. Eye diagram of the received signal at a signal bandwidth of 400 Hz of: (a) without deploying the ANN-based receiver, and (b) after applying the proposed receiver.

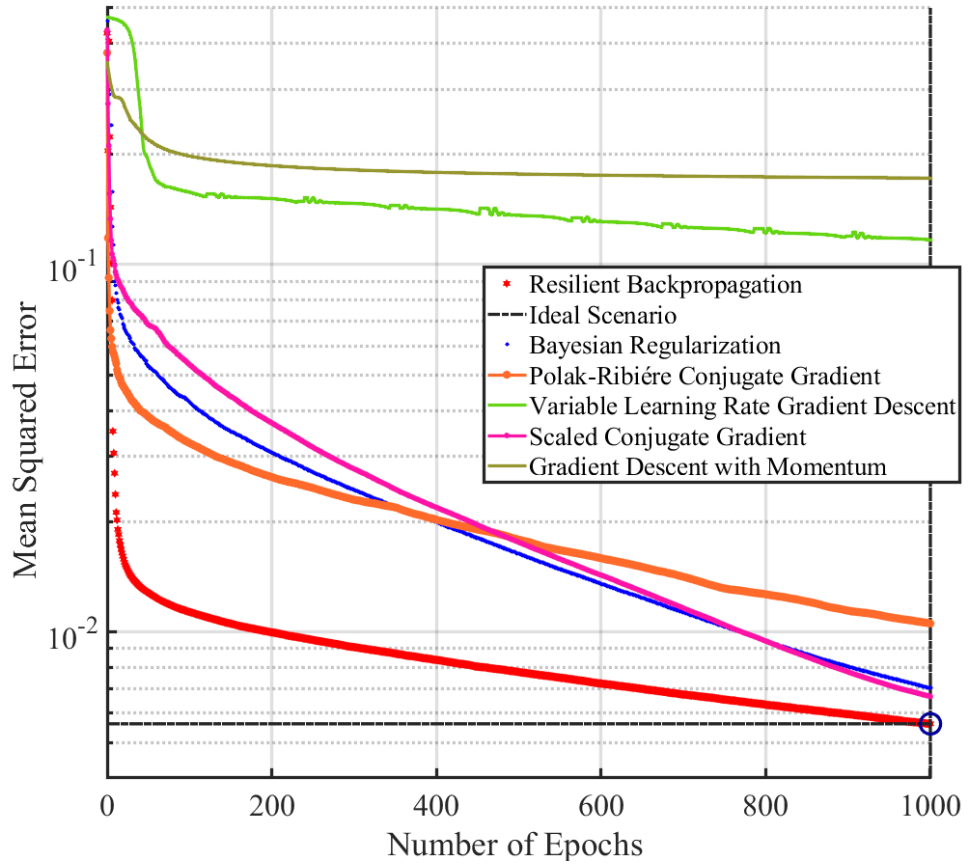


Figure 5-10. ANN system behaviour over time to calculate the faster convergence of different training algorithms for hyperbolic tangent sigmoid activation function.

5.6 Summary

In this chapter and for the first time, ANN adaptive equaliser was demonstrated at the receiver within the OCC system. The study provided the performance indicators for the proposed system. The data rates achieved were the highest in the OCC field, recorded as 12 kbps at the exposure time of 2, 1, and 0.5 ms using a single source and the MLC-NRZ encoded signal. The proposed system demonstrated the capability in retrieving the transmitted information with a bandwidth beyond the cut-off frequency limitation. Hence, it provided the bandwidth improvement of around 9, 5, and 2 times at the exposure times of 2, 1, and 0.5 ms, respectively.

Chapter 6

The Utilization of ANN Equalizer and a Constant Power-PAM in RS-Based OCC System

6.1 Introduction

In OCC systems, which are part of the OWC, leverage the use of off-the-shelf conventional, CMOS ISs and LEDs as the Rx and the Tx, respectively. The camera-based RxS can capture intensity-modulated light signals from a range of LED light sources (i.e., traffic lights, advertising boards, signage, display screens, vehicle head, and taillights, streetlights, etc.). The OCC technology together with the visible and infrared light transmission could be used in different low data rate R_b applications, such as the Internet of Things (IoT) (e.g., as part of the fifth-generation wireless and beyond), motion capturing [241], intelligent transportation systems [246], indoor localization, security, virtual reality, and advertising [247]. OCC comprises a plurality of pixels (i.e., PDs), where the signal strength of each pixel depends on the intensity of incident light [28]. Each pixel can detect signals at different wavelengths over the visible range, e.g., RGB, hence offering parallel detection capabilities and an adaptive FoV feature. In addition, the transmitted information from many light sources, different directions, and locations via the LoS [248], [249], non-LoS, and/or a combination of both paths [228] can be captured using a single-pixel or a pixel-array IS-based Rx. Thus resulting in a higher signal-to-noise ratio, improved mobility, and flexibility over a linkspan up to hundreds of meters [250].

On the contrary, the IS requires a higher sampling duration and lower number of quantization levels compared with the PDs due to the light integration time (known as the exposure time T_{exp}), and the built-in analog to digital converter circuit [251]. The sequential-readout nature of CMOS IS-based Rx allows each pixel-row to capture the incident light at a different time, thus resulting in the so-called RS effect [251]. Note that, the performance of VLC with IS-based Rx is limited mainly by the camera capabilities,

i.e., the frame rate R_f , T_{exp} , and FoV. As a result, in OCC, the transmission bandwidth is rather low and limited to a few tens of kHz compared to the PD-based VLC systems. Although, low data should not be seen as a problem considering that there are many applications where low R_b is not critical at all (i.e., IoT, etc.). However, in OCC, lower R_b may result in the flickering effect at the Tx [232], [252]. In IEEE 802.15.7m standard [253], different schemes have been proposed for OCC to mitigate flickering and to increase R_b [254]. For example, in [46], an optical orthogonal frequency division multiplexing VLC with a special IS-based Rx with a built-in PD-array was used to achieve a very high R_b of 55 Mbps. However, the fabrication process of the IS was too complex and, therefore, not commercially available. In [37], [255], under-sampled frequency and phase shift OOK modulation schemes were proposed to mitigate flickering in OCC with low R_b . In [43], Manchester coding was proposed to alleviate flickering in the RS mode, where it was shown that link performance in terms of R_b deteriorated with the transmission range [43], [250].

Moreover, an OCC link with the under-sampled PAM with subcarriers was experimentally demonstrated with the increase R_b to 250 bps [162], [256]. In addition, a multilevel-intensity modulation scheme for RS-based OCC with the frame rate R_f of 30 fps was proposed in [257] with R_b of 10 kbps over a link range of up to 2 m. Furthermore, a parallel transmission VLC system with color-shift-keying (i.e., different colors RGB-LEDs) was reported in [258] with an overall R_b of 5.2 kbps. In [259], the concept of parallel transmission was demonstrated over a range of up to 60 m and with R_b of 150 bps. Whereas a 16×16 array μ LED and a high-speed camera with R_f of 960 fps and using R_b of 122.88 kb/s was reported in [260].

In OCC systems, equalization methods can also be deployed to compensate for spatial and temporal induced dispersion. In [222], an OOK VLC (a single LED) and camera-based Rx with a dual equalization scheme to compensate for both spatial and temporal dispersion were reported with increased R_b up to 14.37 kb/s. The ANN architecture has also been proposed for post-equalization to combat non-linear impairments in OWC [236], [240]. The use of an ANN-based equalizer is one of the remarkable solutions adapted in PD-based OWCs, wherein the ANN act as the universal classifiers [231]. In [236], a 170 Mb/s OOK VLC link using an LED with a modulation bandwidth of 4.5 MHz and the ANN-based equalizer at the Tx was reported, where the superiority of ANN equalizers in mitigating ISI was demonstrated compared with other equalization

techniques. Note, in OCC with the ANN-based equalizer, the network needs to be trained once for a range of T_{exp} with the data being stored in a look-up table within the camera.

In [261], the variable transparent amplitude shape code scheme was experimentally evaluated for D2D (i.e., smartphones) communications in the form of High-density modulation with the ANN assisted demodulator. R_b of 2.66 Mbps over a 20 cm long transmission link was achieved. Note, the concept of D2D is one form of the multiple-input multiple-output system, where every pixel is transmitted and detected. Similarly, to allow transmission and reception of information under bad weather conditions, a convolution neural network-based OCC was proposed in [262]. The CNN was used for classification and recognition of LED patterns and to decode the transmitted data streams even under an unclear state, where LED patterns are not visible to the camera due to blocking of the transmission path and/or weather conditions. In [233], an OCC link with an ANN-based decoder was reported to mitigate the gap-time effect between two adjacent frames, where OOK was transmitted using an RGB-LED with R_b of 47 kb/s. In [28], an OCC link using a single LED source and Manchester line code with the non-return to zero formats was reported with R_b of 14 kb/s.

In this work, the aim is to establish a flickering-free OCC system with improved R_b using a single LED and an ANNs-based equalizer. The key contributions extended from our previous work [263] are:

- Comprehensive and systematical investigation of the applicability of CP-PAM for the LED- and camera-based VLC.
- Development of a practical CP-PAM OCC prototype with a single Luxeon Rebel white LED (SR-01-WC310) and an IS (Thorlabs DCC1645C) as the Tx and the Rx, respectively.
- Development of an efficient signal extraction algorithm for the RS-based OCC system.
- Implementation of an ANN-based equalizer at the Rx to enhance the system performance.
- Development of an experimental test-bed for the proposed system and evaluating it in terms of the Tx's frequency, eye diagrams, and the BER with and without the ANNs-based equalizer.

- Proposing a new measurement metric for assessing the quality of the communications link in terms of the number of row pixels/symbol.

The remainder of the chapter is organized as follows. Section 6.2 introduces the proposed CP PAM scheme, whereas Section 0 outlines the ANN equalizer model for IS-based OCC. The experimental setup is described in Section 6.4. Results and discussion are presented in Section 6.5. Finally, the summary is given in Section 6.6.

6.2 Constant Power-PAM in RS-Based OCC System

The OCC system is mainly composed of a light source-based Tx with normalized length (diameter) represented in L , and a camera-based Rx, which is modeled using a single convex lens with a focal length f . The transmission speed in the RS-based OCC system is defined by the amount of the information that can be captured by an image at the distance d , which depends on the acquired number of samples (i.e., pixel rows) and is given by [264]:

$$N_{row} = 2f \times \tan\left(\frac{\text{FoV}}{2}\right) = 2f \times \frac{L}{2d}, \quad (6.1)$$

where FoV is the angular field of view.

Note that, the acquired N_{row} is incorporated with the sampling frequency of the IS, known as the rolling rate of IS, F_s (i.e., the frequency at which the row pixels are sampled at the image plane).

Therefore, the maximum frequency of the transmitted signal is limited $\frac{F_s}{2}$ according to Nyquist's theorem. The F_s value depends on the pixel clock and T_{exp} (i.e., the time that every sample (pixel) of the IS is exposed to the light). Note, T_{exp} acts as a moving-average filter [232], [235] with the frequency resolution given by:

$$\Delta f = \frac{1}{T_{exp}} = \frac{F_s}{N_{row}(d)}, \quad (6.2)$$

F_s is defined in terms of the bandwidth of the transmitted signal f_{Tx} and the number of received pixels per symbol, N_{pps} , which is given by:

$$F_s = N_{pps} \cdot f_{Tx}, \quad (6.3)$$

Note, (i) N_{pps} varies with the payload P_{bit} ; and (ii) the maximum transmission distance is proportional to both Δf and the size (diameter) of the light source. Higher T_{exp} results in increased signal intensity levels, and, therefore, higher signal-to-noise-ratio (SNR) at the cost of reduced Rx bandwidth. With reference to Equations (1–3), a communications link can be established at low R_f but with flickering, which is due to the variation in the mean value of light intensity during a time period larger than the optical bandwidth of the human eye. This may occur provided there are many consecutive symbols with the same logical state.

The flicker index is a relative measure of the cyclic variation in the output of various sources at given frequencies [265], [266]. It considers the waveform of the light output and its amplitude, which can be determined by dividing the area above the line of average light output by the total area under the light output curve for a single curve, see Figure 6-1, and is given by:

$$\text{Flicker index} = \frac{\text{area 1}}{\text{area 1} + \text{area 2}}. \quad (6.4)$$

The flicker index has a range of 0 to 1.0, with 0 representing the steady light output level. Area 2 may be close to zero provided the light output varies as periodic spikes, thus leading to a flickering index close to 1. Higher values indicate an increased possibility of noticeable flickering.

To mitigate flickering, CP-PAM can be adopted to equalize the mean intensity value of all symbols, i.e., I_{ave} [256]. In CP-PAM, each PAM symbol is temporally divided into two equal chips, (i) the 1st chip for the intensity of the PAM symbol I_S ; and (ii) the 2nd chip for the stabilization level, i.e., $2I_{ave} - I_S$, see Figure 6-2. For example, a symbol with a level of “2” will be stabilized in the following chip with another symbol with a level of “1” to ensure performance equality, as clarified in Table 6.1.

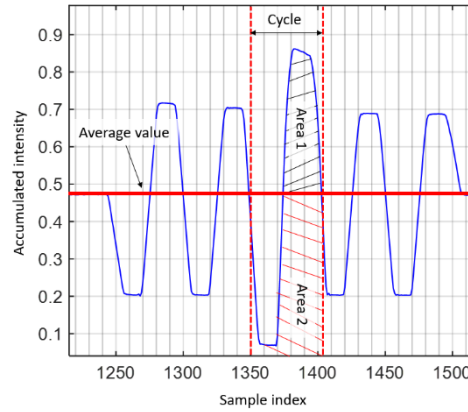


Figure 6-1. Defining flicker index [265], [266].

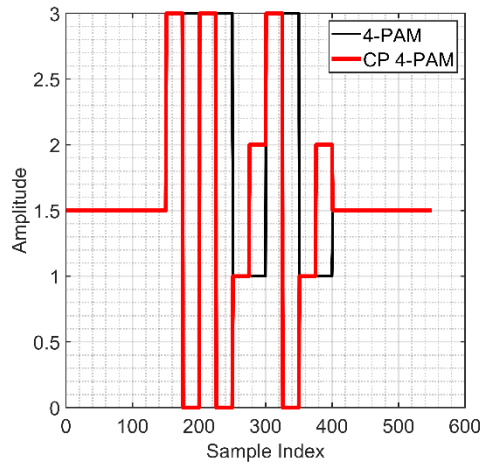


Figure 6-2. An example of a generated packet signal with f_{Tx} of 220 Hz.

It is also noted that considering the R_b efficiency of CP 4-PAM is reduced by half due to the stabilization level (also used for error detection), the CP N-PAM offers a higher coding efficiency compared with Manchester coding [43].

Table 6.1 Proposed CP 4-PAM levels.

Input Data	Conventional PAM Level	Constant Power 4-PAM	
		First Level (I_s)	Stabilization Level ($2I_{ave} - I_s$)
11	3	3	0
10	2	2	1
01	1	1	2
00	0	0	3

6.3 ANN Equalizer

In RS-based OCC systems, the IS sampling process limits the available bandwidth and results in ISI at higher data rates, thus impacting the performance of the communications link. The ability to detect the slow rise-time symbol may be impacted by the existence of the transition between different illumination levels. Equalization is one option that is being adopted to mitigate the ISI. Note, the ISI is predicted by the training filter coefficients based on a training sequence. Alternatively, the ISI can be viewed as a classification problem, where class decision boundaries are created to classify symbols based on training [28]. Hence, determining the optimal threshold boundaries in a practical channel can be seen as a nonlinear process, and consequently, the ANN-based equalizer with the adaptive algorithm can be employed to mitigate ISI and, therefore, increase the data rate. Unlike other communication systems, OCC training of the ANN network is carried out only once for a specific exposure time with the data being stored with a look-up table [236], [240].

An ANN is an interconnected network of processing elements (neurons). It comprises of two distinct stages: (i) The training phase, where the ANN estimates an input-output map between the received and training data to determine the weighted input from each neuron. The weighted values are updated in each training iteration until either the required performance is achieved, or the entire training set is used; and (ii) the operation phase, where the ANN is deployed without the knowledge of the dataset under test. The MLP is a popular ANN architecture, which has been demonstrated with high effectiveness in signal equalization [267]. It offers the ability to map any non-linear input-output sequence, provided there are sufficient neurons in the hidden layer(s), and the SNR is sufficiently high.

The MLP structure consists of at least three layers; (i) a single input layer x ; (ii) $(M - 1)$ hidden layers; and (iii) a single output layer y . The input layer (also called the observation vector) has the same structure as a conventional linear equalizer for sequential equalization, i.e., it is a tapped delay line $\mathbf{o}^{(m-1)} = [o_1^{(m-1)}, o_2^{(m-1)}, \dots, o_{N_{m-1}}^{(m-1)}]$, where N is the number of neurons, and m is the layer number. This is illustrated in Figure 6-3, where weights $w_{kn}^{(m)}$ relate the n^{th} input to the k^{th} neuron. Each neuron can be biased with a value $C^{(m)}$, which is in turn scaled by a threshold factor $v_k^{(m)}$.

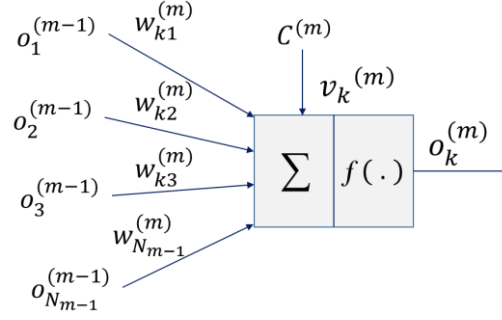


Figure 6-3. A structure of the k^{th} neuron in the layer m .

The output $o_k^{(m)}$ of the k^{th} neuron is mapped via a non-linear activation function $f(\cdot)$ as given by [236]:

$$o_k^{(m)} = f\left(\sum_{n=1}^{N_{m-1}} w_{kn}^{(m)} o_n^{(m-1)} + C^{(m)} v_k^{(m)}\right). \quad (66.5)$$

The output of each layer is usually connected to each of the neurons in the next layer, i.e., a fully connected mode, therefore, using the observation vector $\mathbf{o}^{(m)}$ for the m^{th} layer and the $N_m \times N_{m-1}$ connection matrix between layers m and $m - 1$, the output is given in the vector form by:

$$\mathbf{o}^{(m)} = f(\mathbf{W}^{(m)} \mathbf{o}^{(m-1)} + C^{(m)} \mathbf{v}^{(m)}), \quad (6.6)$$

where $\mathbf{W}^{(m)}$ and $\mathbf{v}^{(m)}$ are given by:

$$\mathbf{W}^{(m)} = \begin{bmatrix} \mathbf{w}_1^{(m)} \\ \mathbf{w}_2^{(m)} \\ \vdots \\ \mathbf{w}_{N_m}^{(m)} \end{bmatrix}, \quad (6.7)$$

$$\mathbf{v}^{(m)} = [v_1^{(m)} \quad v_2^{(m)} \quad \dots \quad v_{N_m}^{(m)}]^T. \quad (6.8)$$

Considering the $N_0 \times 1$ input vector, $N_M \times 1$ output vector, $\mathbf{o}^{(0)} = \mathbf{x}$ and $\mathbf{o}^{(M)} = \mathbf{y}$, the following observation vector $\mathbf{o}^{(m)}$ is given by:

$$\mathbf{x} = [x_1 \quad x_2 \quad \dots \quad x_{N_0}^{(m)}]^T, \quad (6.9)$$

$$\mathbf{y} = [y_1 \quad y_2 \quad \dots \quad y_{N_M}^{(m)}]^T. \quad (6.10)$$

Therefore,

$$\mathbf{o}^{(1)} = f[\mathbf{W}^{(1)}\mathbf{x} + \mathbf{C}^{(1)}\mathbf{v}^{(1)}], \quad (6.11)$$

$$\mathbf{o}^{(2)} = f[\mathbf{W}^{(2)}\mathbf{o} + \mathbf{C}^{(2)}\mathbf{v}^{(2)}], \quad (6.12)$$

...

$$\mathbf{y} = f[\mathbf{W}^{(M)}\mathbf{o}^{(M-1)} + \mathbf{C}^{(M)}\mathbf{v}^{(M)}]. \quad (6.13)$$

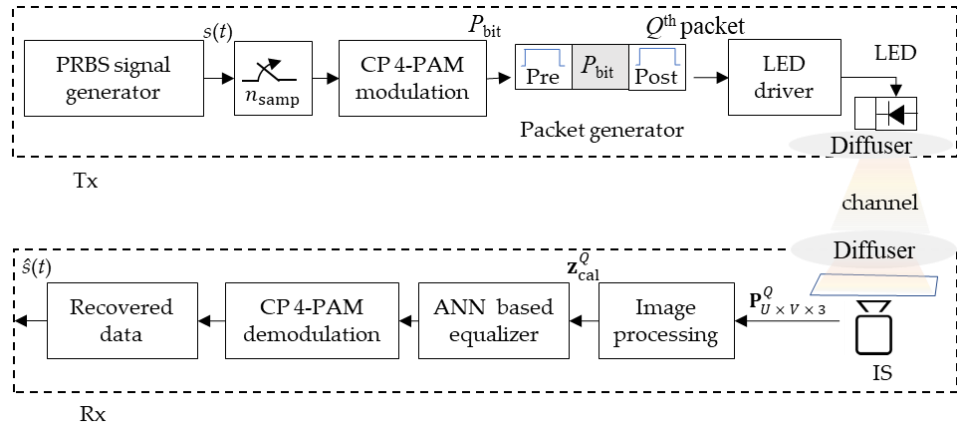
MLP will record its trained information in $w_{kn}^{(m)}$ and in the threshold factors $\mathbf{v}_n^{(m)}$, since $\mathbf{C}^{(m)}$ is given as a constant for all layers (i.e., set as $\mathbf{C}^{(m)} = 1, m = 1, 2, \dots, M$). RBP is a supervised BP training method, which updates the weights to converge more rapidly than the standard BP training technique [240]. Figure 6-3 depicts a single neuron for the case where the layers are interconnected with different weight coefficients. The RBP adjusts the MLP weights to reduce the error cost function E_n as given by [236]:

$$E_k = ||d_k - y_k||^2, \quad (6.14)$$

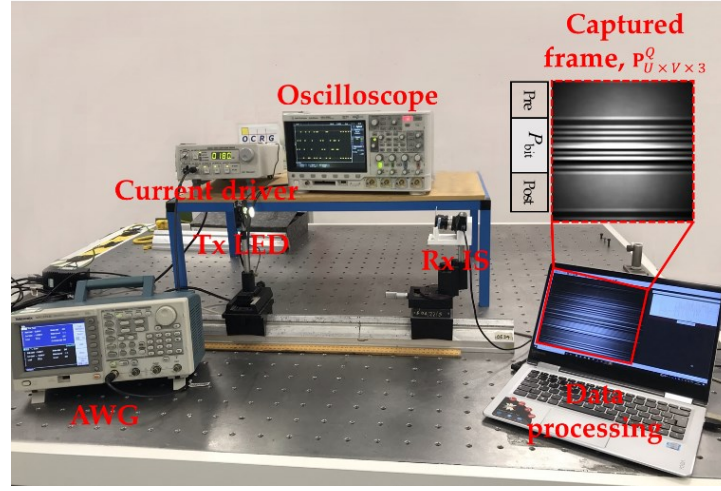
where d_k and y_k are the ideal and actual received symbols, respectively. It should be noted that, for the training sequence, \mathbf{d} is known. Each iteration of the RBP algorithm has a dynamic step size, which varies based on the magnitude of the gradient descent of E_k .

6.4 Experimental Setup

The schematic block diagram of the proposed OCC system is shown in Figure 6-4(a). A PRBS with a length of $2^{16}-1$ bits was generated using MATLAB, which was then up-sampled with n_{samp} of 50 and modulated using CP-4-PAM. Based on the output labels provided for 4-PAM, see Table 6.1, mapping of the data to the corresponding symbols was carried out.



(a)



(b)

Figure 6-4. The CP 4-PAM OCC scheme: (a) system block diagram, and (b) photograph of the experimental setup.

The PRBS $s(t)$ was divided into sub-sequences with effective symbols per packet with lengths of P_{bit} - symbols, which depends on the transmitter bandwidth f_{Tx} . Each subsequence was encoded with a pre- and post-amble to form a Q^{th} Tx packet, where Q^{th} represents the packet number and each packet consists of 3-symbol pre-amble [1.5 1.5 1.5], P_{bit} -symbol payload, and 3-symbol post-amble [1.5 1.5 1.5].

The symbols in the overhead signal (i.e., pre-amble and post-amble) were chosen to ensure constant average optical power when compared with the payload. The signal was then sequentially uploaded onto an arbitrary wave generator (AWG, AFG3252C, 240 MHz bandwidth), see Figure 6-4(b). The uploading process was done through the generation of Q^{th} Tx packet at different f_{Tx} , the output of which was used for intensity modulation of a Luxeon Rebel LED (SR-01-WC310) with a peak wavelength at 630 nm. Note, a linewidth of 118 nm was used for transmission of the modulated light over a short LoS free-space channel (i.e., 50 cm).

At the Rx, a diffuser was used to scatter the light over the capturing area of the IS (Thorlabs DCC1645C RS) with a standard T_{exp} of 2 ms was adopted in this study. The observed frames $\mathbf{P}_{U \times V \times 3}^Q$ at the output of the camera were processed off-line in MATLAB using both Algorithms 1 and 2. In Algorithm 6-1, the data set \mathbf{z}_i^Q was retrieved by accumulating the intensities for all pixels in each row. The received signal was then normalized to remove the DC by capturing 20 frames with no signal, see Figure 6-5 (a,b).

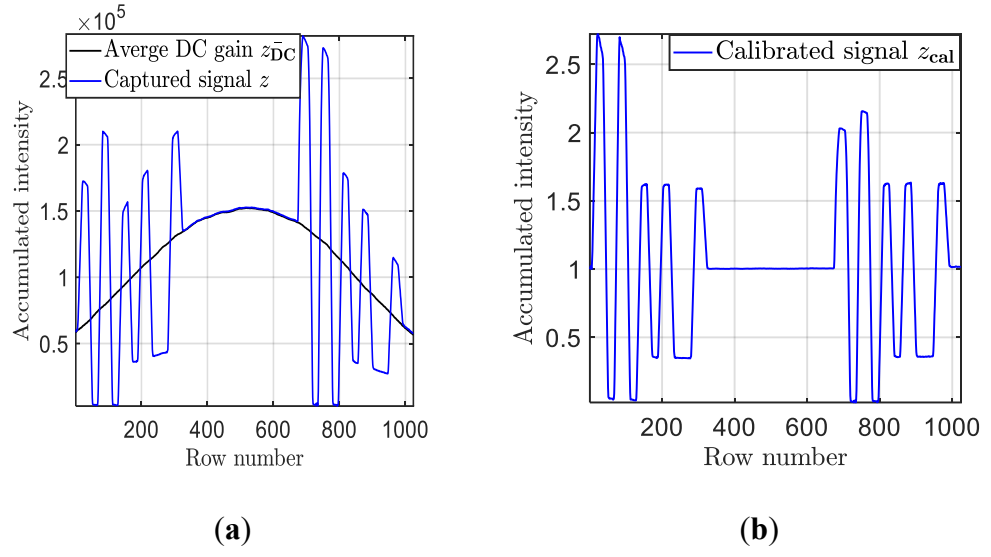


Figure 6-5. An example of the received Q^{th} Tx packet signal at a T_{exp} of 2 ms: (a) without DC gain normalization, and (b) with normalization.

Algorithm 6-1 Signal extraction algorithm.

Input: Q^{th} Tx packets signals and $(Q^{\text{th}} \times 10 \text{ RS})$ Captured frames $\mathbf{P}_{U \times V \times 3}^Q$ at different f_{Tx} where $Q = 1, 2, \dots, 150$ and 20 frames of illumination gain (DC signal only) $\mathbf{G}_{U \times V \times 3}$

Output: $\mathbf{z}_{\text{cal}}^Q$ with that is fully synchronized with Tx packet

- 1 **For each** $Q = 1$ to 150 **do**
- 2 • Read $U \times V \times 3$ sized colour plain text frame $\mathbf{P}_{U \times V \times 3}^Q = [[P^Q(i, j, c)]]$. The RGB components of $\mathbf{P}_{U \times V \times 3}^Q$ denoted as $\mathbf{RP}_{U \times V}^Q = RP^Q(i, j)$, $\mathbf{GP}_{U \times V}^Q = GP^Q(i, j)$, $\mathbf{BP}_{U \times V}^Q = BP^Q(i, j)$, respectively, $i = 1, 2, \dots, U$ and $j = 1, 2, \dots, V$ represents the pixels indices of captured frame, and $c = 1, 2, 3$.
- 3 • Monochrome to grayscale frame conversion is applied by calibrating RGB components $\mathbf{RP}_{U \times V}^Q$, $\mathbf{GP}_{U \times V}^Q$, and $\mathbf{BP}_{U \times V}^Q$ together over c , resulting $\mathbf{PS}_{U \times V}^Q$.
- 4 • Accumulate intensities for all pixels at each row $\mathbf{z} = (\mathbf{z}_i)_{i=1}^V$ where $\mathbf{z}_i^Q = \sum_{j=1}^V \mathbf{PS}_{U \times V}^Q$.
- 5 • Estimate the averaged DC value \bar{z}_{DC} by repeating previous steps on $\mathbf{G}_{U \times V \times 3}$.
- 6 • Calibrate \mathbf{z}^Q with respect to the averaged DC value $\mathbf{z}_{\text{cal}}^Q = \mathbf{z} \frac{1}{\bar{z}_{DC}}$
- 7 • Find the frame with full packet inclusion using Algorithm 2
- 8 • Resample $\mathbf{z}_{\text{cal}}^Q$ with respect to the packet length
- 9 • Locate the start of each packet in the frame
- 10 • Synchronize both Tx and Rx signal using a correlation algorithm
- 11 • return $\mathbf{z}_{\text{cal}}^Q$ signal
- 12 **end**

Next, to ensure that a full packet was captured by the IS, Algorithm 6-2 was applied to select the optimum frame (i.e., including both pre- and post-ambles) for each Q^{th} Tx packet per f_{Tx} , in which $10 \times \mathbf{P}_{U \times V \times 3}^Q$ are captured at Q^{th} Tx packet to maintain the synchronization between both the Tx and the Rx.

A resampling process was then applied to resize the signal length based on the packet size observed in pixels. Next, a correlation algorithm was used to maintain the synchronization between the transmitted Q^{th} Tx packet and received $\mathbf{z}_{\text{cal}}^Q$ signals, where a filtered version of $\mathbf{z}_{\text{cal}}^Q$ was simulated based on the encoded Q^{th} packet using a moving average filter. Note, the window size of the filter was set to n_{samp} since it provided an

optimal match compared with the observed signal. Next, \mathbf{z}_{cal} in the vector form was applied to an MLP equalizer using an array of tapped-delay lines as previously described. The MLP used here included single input, hidden, and output layers. All the key system parameters are listed in Table 6.2.

Algorithm 6-2 Find the frame with full packet inclusion (i.e., includes both pre- and post-ambles).

Input: $10 \times \mathbf{P}_{U \times V \times 3}^Q$ Captured frames at Q^{th} Tx packet

Output: One frame $\mathbf{P}_{U \times V \times 3}$ at each Q^{th}

```

1      for  $l = 1$  to 10
2          Define  $Check$ ,  $Counter$ ,  $CeckVal$ 
3           $Check = \text{abs}(\mathbf{z}_{\text{cal}}^Q(2:\text{end}) - \mathbf{z}_{\text{cal}}^Q(1:\text{end} - 1))$ 
4           $Check = Check < 0.01$ 
5          for  $cc = 2:\text{length}(Check)$ 
6              if  $Check(cc) == 1 \ \&\& \ Check(cc) == check(cc-1)$ 
7                   $Counter = Counter + 1$ 
8              else
9                   $CeckValk(l) = Counter$ 
10              $Counter = 0$ 
11         end
12     end
13     return  $\mathbf{P}_{U \times V \times 3}$ 
14 end

```

Table 6.2 System parameters.

Description		Value
Tx	LED type	Luxeon Rebel LED (SR-01-WC310)
	Tx signal bandwidth f_{Tx} (Hz)	220–1520 Hz
	Tx bias current	180 mA
Camera Rx	Camera model	Thorlabs DCC1645C-HQ
	Exposure time T_{exp}	2 ms
	Maximum SNR of IS	44 dB [268]
	Lens type	Navitar 12 mm F/1.8 2/3" 10 MP
	Pixel clock	10 MHz
	Camera raw image resolution	1280 × 1024 pixels
	Captured symbols per frame	11–76 symbols
Packet Generator	Data format	CP-PAM
	Symbol per packet P_{bit}	5–70 symbols
	Packet generator sample rate	11.125 kHz
	Number of samples n_{samp}	10
Channel	Channel length	50 cm
ANN Equalizer	Activation function	Hyperbolic tangent sigmoid
	Number of neurons in input layer	200
	Number of neurons in output layer	1
	Number of neurons in hidden layer	200
	Number of hidden layers	2
	Percentage of the train to test	0.8
	Maximum epochs	1000
	learning rate parameter η	0.01
	Network training function	Resilient back-propagation

6.5 Results and Discussions

The experimental work was focused on deploying an MLP-based equalization to mitigate the ISI due to the limited modulation bandwidth of the CMOS IS-based Rx. The measured and simulated CIS for T_{exp} of 2 ms are highlighted in Figure 6-6, showing that the obtained IS bandwidth (i.e., a 3 dB point) was 250 Hz. It is also noted that the mismatch between the measured and simulated response was caused by aliasing due to the limited sampling frequency of the IS and utilization of image compression techniques [269]. The CP 4-PAM encoded signal was then generated at a different bandwidth f_{Tx} of up to 1520 Hz.

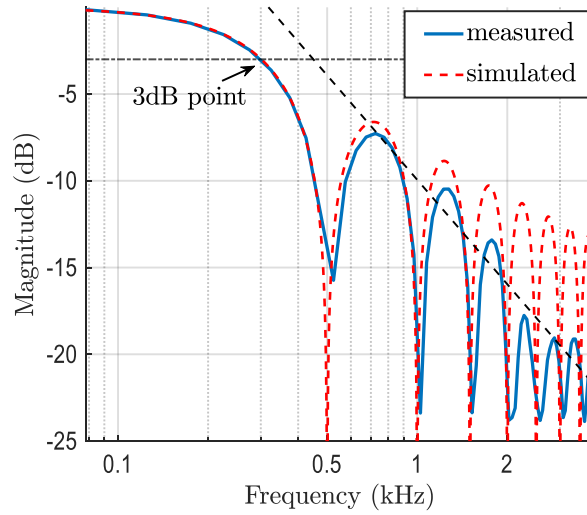


Figure 6-6. Measured and estimated bandwidth of the for IS with T_{exp} of 2 ms.

The captured frames at the Rx are processed with P_{bit} of up to 70 symbols per packet. Figure 6-7 illustrates examples of the captured frames and the processed signals for P_{bit} of 5, 10, 15, 20, 50, and 70, i.e., f_{Tx} 220, 320, 420, 520, 1120, and 1520 Hz, respectively. Note, the width of the received Q^{th} packet and the recorded F_s are 666 pixels and 13.31 kHz, respectively, based on the demodulated signal, see Figure 6-7. Increasing f_{Tx} decreases the number of received pixels for each CP 4-PAM symbol, thus, reducing the quality of data transmission. The number of pixels utilized for each CP 4-PAM symbol is indicated in Table 6.3. For the link with the ANN-based equalizer deployed at the Rx side, the quality of the received signal was measured using the eye diagrams and the BER performance. As illustrated in the eye diagrams, see Figure 6-8, the eye-openings indicate the impact of the ISI on the received signal. Note, (i) the threshold levels can be

differentiated for P_{bit} of 5 and 20 symbols, see Figure 6-8(a,b), respectively, but not for P_{bit} of 50 and 70 symbols as in see Figure 6-8(c,d), respectively; (ii) the five levels are shown in the eye diagrams, where one of the levels represents the packet overhead designed to maintain the same average power for CP 4-PAM; and (iii) the overhead level is removed at the Rx side using Algorithm 6-1.

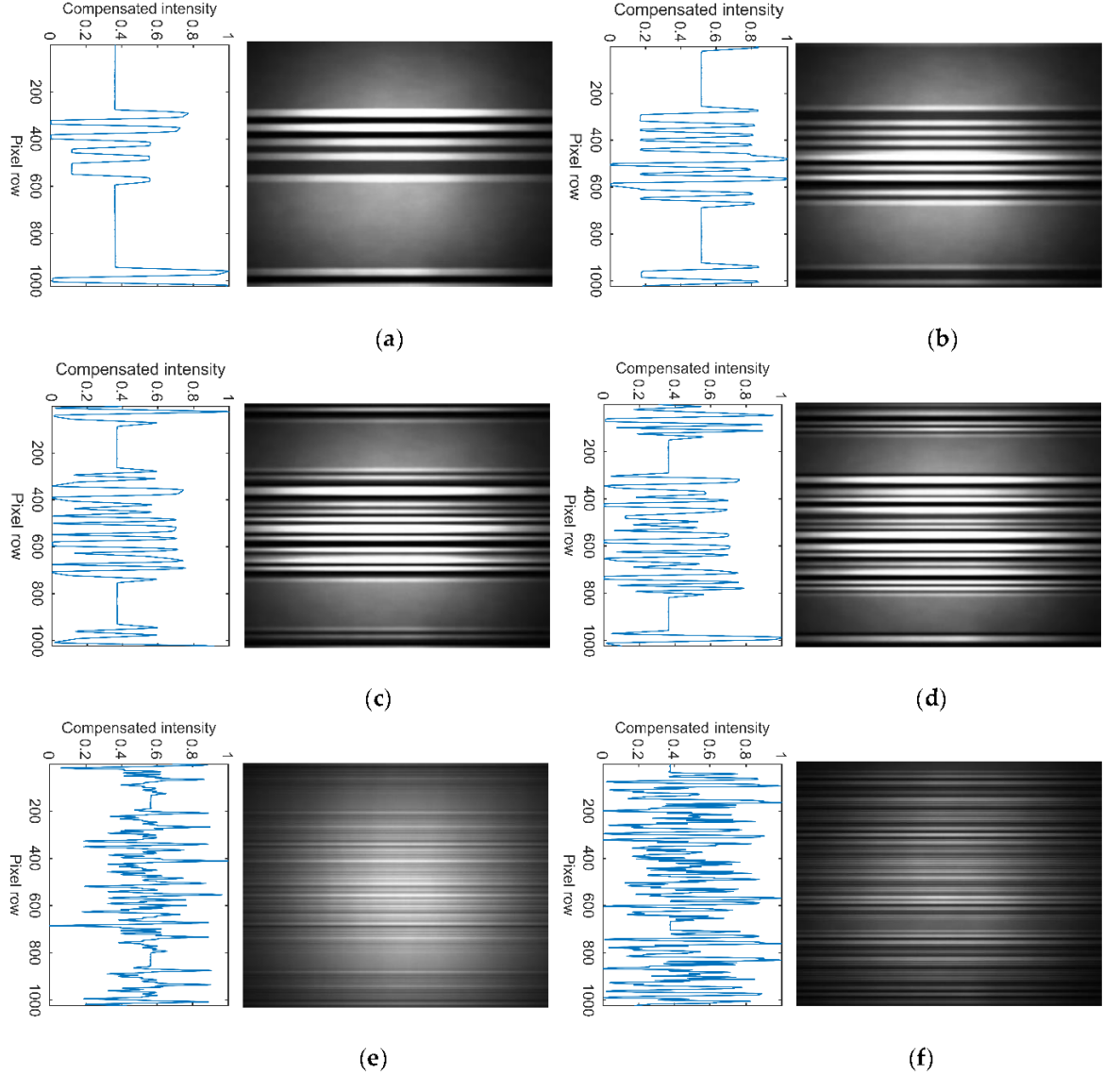


Figure 6-7. Examples of the frame acquisition based on CIS for CP 4-PAM and f_{Tx} of: (a) 220 Hz, (b) 320 Hz, (c) 420 Hz, (d) 520 Hz, (e) 1120 Hz, and (f) 1520 Hz.

Table 6.3 Results with Rf of 30 fps and CIS width of 1024 px.

Payload Symbol/Package (P_{bit})	Total Number of Symbols/Pack et	Number of Row Pixels/Symbol (N_{pps})	f_{Tx} (Hz)
5	11	60.54	220
10	16	41.62	320
15	21	31.71	420
20	26	25.61	520
30	36	18.50	720
35	41	16.24	820
40	46	14.48	920
50	56	11.89	1120
70	76	8.76	1520

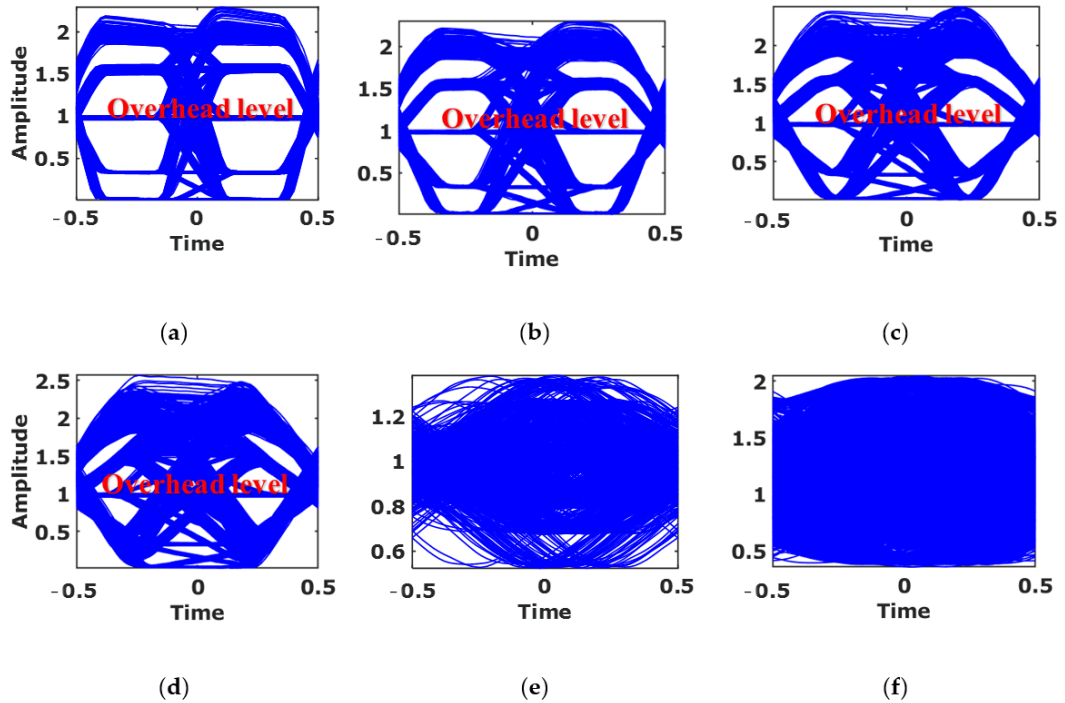


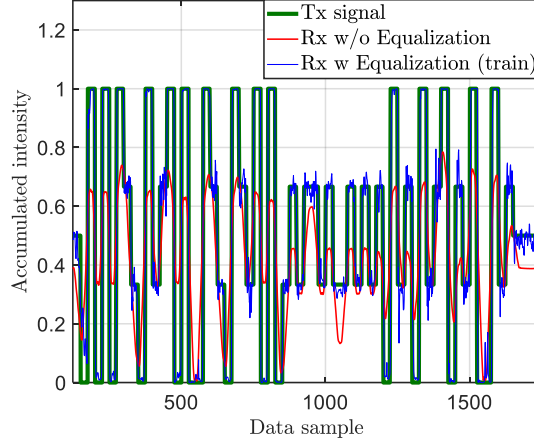
Figure 6-8. Examples of the captured eye diagrams of the CIS received signal for CP 4-PAM with f_{Tx} of: (a) 220 Hz, (b) 320 Hz, (c) 420 Hz, (d) 520 Hz, (e) 1120 Hz, and (f) 1520 Hz.

An example of transmitted and received signals with and without equalizer for N_{pps} of 8.7 pixels per symbol is illustrated in Figure 6-9. The equalized signal at the Rx side shows a significant improvement in reducing the impact of the ISI on the received signal with minimal signal distortions.

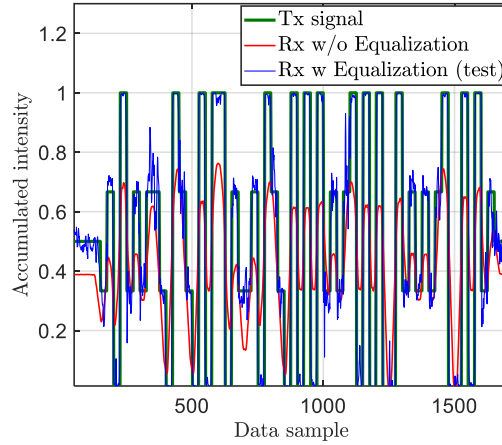
The eye linearity of the received signals is measured based on the average amplitude levels is given by [270]:

$$\text{Eye linearity} = \frac{\min(V_{\text{up}}, V_{\text{mid}}, V_{\text{low}})}{\max(V_{\text{up}}, V_{\text{mid}}, V_{\text{low}})}, \quad (6.15)$$

where V_{up} , V_{mid} , and V_{low} are the average amplitude levels.



(a)



(b)

Figure 6-9. An example of the transmitted and received signal with and without equalization for CP 4-PAM and N_{pps} of 18.5 row pixels/symbol: (a) training sets, and (b) testing sets.

Figure 6-10 shows the eye linearity of the received signals with respect to N_{pps} for the link with and without ANN equalizer and for T_{exp} of 2 ms. Note, we have used N_{pps} , i.e., new terminology for a fair comparison considering the progress made in the development of ISs. As shown, for the link with no equalizer, the eye linearity increases with N_{pps} reaching a maximum level of 0.6 at N_{pps} of ~ 26 , beyond which it drops linearly with rapidly N_{pps} . However, with the ANN equalizer, the eye linearity is improved

significantly for both the test and trained cases reaching the optimal linearization of almost 1 at N_{pps} of 18 and remaining constant beyond $N_{pps} > 18$ (i.e., being independent of N_{pps}). Thus, the ANN equalizer show an improvement of ~66 % in the eye linearity for $N_{pps} > 18$ pixels/symbol (i.e., $f_{Tx} < 920$ Hz) for both training and testing sets.

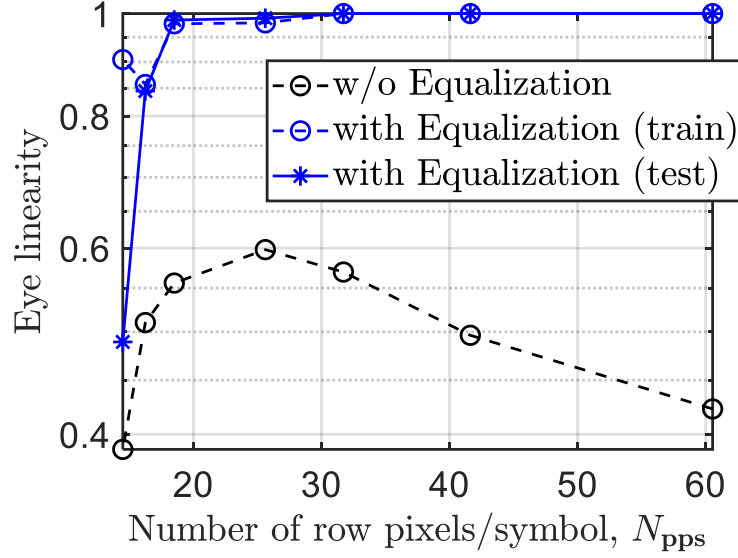


Figure 6-10. The eye linearity against N_{pps} for the proposed system with and without equalization and for T_{exp} of 2 ms.

Next, the BER is measured as a function of N_{pps} for the link with and without ANN equalizer, as illustrated in Figure 6-11. In addition, shown is the forward error correction (FEC) BER limit line of 3.8×10^{-3} . Note, at the FEC limit the N_{pps} value is reduced from 30 to 20 for pixels per symbol for the links without and with the ANN equalizer, respectively, compared with the test plot. Thus, the effective R_b (i.e., no post- and preambles) is estimated by:

$$R_b = 2 \frac{V}{N_{pps}} \cdot R_f, \quad (6.16)$$

where V represents the pixel row.

The effective R_b at the FEC limit for the case with and without the ANN equalizer with a range of IS resolutions is indicated in Table 6.4. It demonstrates with the ANN equalizer R_b of 24.4 and 12.2 kbps for R_f of 60, and 30 fps, respectively, can be achieved compared with the case of no equalizer with R_b of 18.6, and 9.3 kbps for R_f of 60, and 30 fps, respectively.

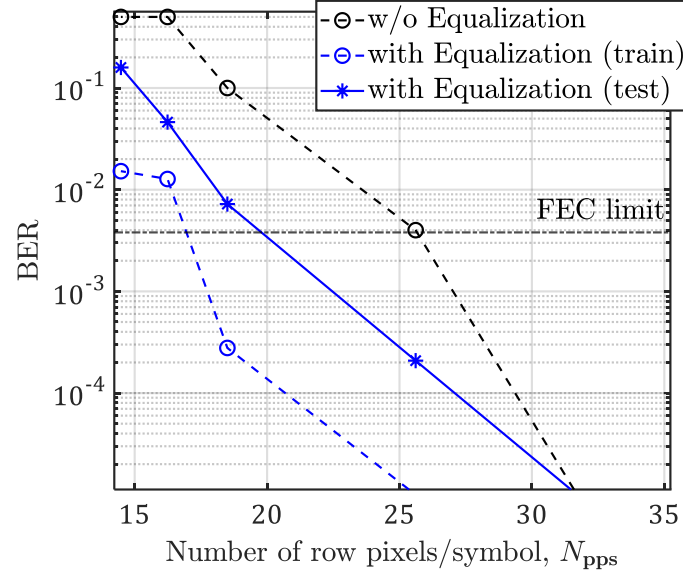


Figure 6-11. The BER measurements as a function of N_{pps} for the proposed system with and without equalization and for T_{exp} of 2 ms.

Table 6.4 Effective R_b at different ISs resolutions at the FEC limits.

ISs Resolutions	R_b (bps) at $N_{pps} = 26$		R_b (bps) at $N_{pps} = 20$	
	(i.e., w/o Equalization)		(i.e., with Equalization)	
	$R_f = 30$ fps	$R_f = 60$ fps	$R_f = 30$ fps	$R_f = 60$ fps
1200×1800	3794	7588	5040	10,080
1500×2100	4486	8972	5940	11,880
1800×2400	5178	10,357	6840	13,680
2100×3000	6563	13,126	8640	17,280
2400×3000	6563	13,126	8640	17,280
3300×4200	9332	18,665	12,240	24,480

6.6 Summary

An ANN-based equalization technique was proposed for a CP 4-PAM based OCC system. An experimental setup was developed to demonstrate non-flickering communications using a single light-emitting diode with a transmission rate of R_b of 24.4 kbps. The quality of received signals was measured based on the eye-diagram opening, eye linearity, and the BER. The ability to mitigate the intersymbol interference was demonstrated and hence to transmit a signal with an acceptable BER (below the FEC limit) for N_{pps} of 20, and 30 for unequalized and equalized systems, respectively. An improvement of ~66 % in the eye linearity was achieved using a single LED, and a typical commercial camera with equalization technique was achieved. The limitation of the proposed system was assessed by the system complexity, including the associative memories needed for the look-up table training data as well as the IS resolution, gap-time and exposure time, and reading time.

Chapter 7

Conclusion and Future Works

7.1 Conclusions

The necessity for indoor location-based services has been growing over the past decades due to its significance in the development of various IoT applications. VLPs have been introduced in recent years, which have shown great potential in achieving high-precision indoor positioning due to the use of optical signals. This thesis focused on enabling VLC for both localization and communication using a single PD, or an array of PDs in the form of a single IS. Initially, an extensive review of various indoor positioning technologies was introduced in Chapter 2. Besides, the key challenges in the existing positioning methods to achieve its foremost goal of facilitating the design of a low-cost, accurate and less complex IPS were pointed out in this chapter. Likewise, the use of different VLPs techniques were then analyzed based on their common characteristics and achievable accuracy.

Most research reported on VLP has focused on the investigation of geometrical properties using range-based (i.e., triangulation/trilateration), fingerprinting, or range-free (i.e., proximity) methods to determine the transmission distance based on establishing a one-to-one relationship between the target location and its RSS. Though, Chapter 3 showed that in most of the reported literature, the angular dependency was neglected in RSS-based localization. with the assumption that, the Rx has a fixed height and is pointing up towards the Tx. However, computational and implementation costs are too high, and the assumptions made may not be valid in real-time application scenarios with mobile Rx. Therefore, the impact of the LED tilting on the VLPs was explored in Chapter 3, in which, the systematic analysis showed that the accuracy of RSS-based VLP is primarily limited by the tilting angles of both Tx and Rx as well as the multipath reflections. Subsequently, a novel approach was proposed to achieve a highly accurate indoor VLP system by considering multipath reflections, in which, the Tx was tilted towards the center of the receiving plane to achieve higher accuracy by maximizing the received power level due to contributions from the LoS paths at the pointing center F.

The positioning error was estimated by using the LLS algorithm with polynomial regression and results showed a significant improvement in the accuracy by up to ~66% compared with a typical non-tilting Tx case. The results also showed that, the uniformity of the proposed VLP system is in line with European Standard EN 12464-1, thus meeting the uniformity requirement of the visible illumination regions.

In Chapter 4, an overview of the merits/application, as well as the experimental reports on IS based VLPs were outlined where details of utilized technology, the number of Tx and Rx, test conditions and the accuracy achieved so far reported in literature were highlighted. Notably, either multiple LEDs have been used for positioning or an additional sensor has been employed to obtain the position. However, in most scenarios, the narrow FoV of the front-facing camera in smartphones restricts the number of Tx's being captured at the IS, thus making bilateration or trilateration impractical. In addition, unilateration allows less complex and low-cost implementation of the VLC system. Also, the deployment of more LEDs will certainly add some constraints to the implementation of VLP. Therefore, to overcome these issues a highly accurate AoA-RSS-based VLPs system using a single LED and an IS was introduced. A novel technique was proposed to mitigate the error induced by the lens at the receiving side, hence, leading to reduced positioning errors. The experimental results showed that, the proposed method offers immunity (i.e., power improvement by ~15 %) against different exposure times within the standard range of 250 μ s to 4 ms, as well as outperforming the RSS method in all circumstances and AoA reported previously. Likewise, a 3D RMSE of 7.56 cm was achieved using the proposed algorithm. Furthermore, we investigated the impact of exposure time on the detection of the Tx's location.

Next, the use IS can be used as an inherently Rx module in OCCs, which can capture light signals from a range of sources. In Chapter 5, an overview of the OCC link capabilities reported in the literature was initially explored. The modelled standard IS-based Rx showed that the DC gain is proportional to T_{exp} , therefore a trade-off between the gain and the required bandwidth, where increasing T_{exp} will reduce the cut-off frequency. As a result, in OCC, the transmission bandwidth is rather low and limited to a few tens of kHz compared to the PD-based VLC systems. Therefore, in this chapter and for the first time, ANN adaptive equaliser was demonstrated at the receiver within the OCC system. The study provided the performance indicators for the proposed system.

The data rates achieved were the highest in the OCC field, recorded as 12 kbps at the exposure time of 2, 1, and 0.5 ms using a single source and the MLC-NRZ encoded signal. The proposed system demonstrated the capability in retrieving the transmitted information with a bandwidth beyond the cut-off frequency limitation. Hence, it provided the bandwidth improvement of around 9, 5, and 2 times at the exposure times of 2, 1, and 0.5 ms, respectively.

Similarly, an ANN-based equalization technique was proposed for a CP 4-PAM based OCC system in Chapter 6. An experimental setup was developed to demonstrate non-flickering communications using a single light-emitting diode with a transmission rate of R_b of 24.4 kbps. The quality of received signals was measured based on the eye-diagram opening, eye linearity, and the BER. The ability to mitigate the intersymbol interference was demonstrated and hence to transmit a signal with an acceptable BER (below the FEC limit) for N_{pps} of 20, and 30 for unequalized and equalized systems, respectively. An improvement of ~66 % in the eye linearity was achieved using a single LED, and a typical commercial camera with equalization technique was achieved. The limitation of the proposed system was assessed by the system complexity, including the associative memories needed for the look-up table training data as well as the IS resolution, gap-time and exposure time, and reading time.

In Summary, this thesis focused on the key challenges of VLP systems and provided novel contributions and insights in (i) tilting the Tx can be beneficial in VLP systems to provide a highly accurate indoor VLP system by considering multipath reflections; (ii) increasing VLP robustness for IS-based Rx against different exposure time capturing conditions using a novel AoA-RSS-based VLP system and a single LED; (iii) increasing the OCC transmission link capabilities using an ANN-based equalizer; and (iv) demonstrate non-flickering communications using a CP 4-PAM based OCC system.

7.2 Future Works

The conducted research in this thesis reveals additional prospects and areas that require further investigation. For future work, the following recommendations are suggested:

1. Many positioning methods have been integrated with AR technology to provide indoor VLPs in the recent decade. Visual markers have been proposed as a solution to indicate the device's exact location and orientation. However, these markers must be scanned by users and displayed on everything they augment. As a result, its implementation is difficult to scale and cannot be modified without highly time-consuming and expensive efforts. Alternatively, an integration of a VLP-based OCC system with AR technology can be examined to provide a seamless and reliable positioning and communication link.
2. The IS designer should do further research into expanding the IS bandwidth since it might be critical in providing a new technology that integrates imaging, positioning, and communication simultaneously.
3. The NLoS communication link may be examined with IS-based VLP system applications, where the camera can capture the modulated signals regardless of the existence of the LoS link.
4. The usage of a near-infrared band that is visible to a typical camera but invisible to the human eye might be researched further, allowing the OCC linkages to be used in a variety of IoT applications at low cost and with minimal complexity.
5. An investigation into the use of IS-based VLP utilising an OCC system for underwater settings is another area that may contribute to the progress and enabling technologies of underwater wireless communication systems. This includes aspects such as system architecture, synchronisation, frame selection, image processing techniques required to decode the information, and optimization techniques.

References

- [1] E. D. Kaplan and C. J. Hegarty, *Understanding GPS: principles and applications*. Boston : Artech House, 1996.
- [2] Y. Zhuang and N. El-Sheimy, "Tightly-Coupled Integration of WiFi and MEMS Sensors on Handheld Devices for Indoor Pedestrian Navigation," *IEEE Sens. J.*, vol. 16, no. 1, pp. 224–234, 2016, doi: 10.1109/JSEN.2015.2477444.
- [3] J. Nieminen *et al.*, "Networking solutions for connecting bluetooth low energy enabled machines to the internet of things," *IEEE Netw.*, vol. 28, no. 6, pp. 83–90, 2014, doi: 10.1109/MNET.2014.6963809.
- [4] Y. Zhuang, J. Yang, Y. Li, L. Qi, and N. El-Sheimy, "Smartphone-Based Indoor Localization with Bluetooth Low Energy Beacons," *Sensors*, vol. 16, no. 5, p. 596, Apr. 2016, doi: 10.3390/s16050596.
- [5] N. B. Priyantha, A. K. L. Miu, H. Balakrishnan, and S. Teller, "The Cricket Compass for Context-Aware Mobile Applications," in *Proceedings of the 7th Annual International Conference on Mobile Computing and Networking*, 2001, pp. 1–14. doi: 10.1145/381677.381679.
- [6] H. Liu, H. Darabi, P. Banerjee, and J. Liu, "Survey of wireless indoor positioning techniques and systems," *IEEE Trans. Syst. Man Cybern. Part C Appl. Rev.*, vol. 37, no. 6, pp. 1067–1080, 2007, doi: 10.1109/TSMCC.2007.905750.
- [7] M. J. Kuhn, J. Turnmire, M. R. Mahfouz, and A. E. Fathy, "Adaptive leading-edge detection in UWB indoor localization," in *2010 IEEE Radio and Wireless Symposium (RWS)*, New Orleans, LA, USA, Jan. 2010, pp. 268–271. doi: 10.1109/RWS.2010.5434259.
- [8] H. Zou, L. Xie, Q.-S. Jia, and H. Wang, "Platform and Algorithm Development for a RFID-Based Indoor Positioning System," *Unmanned Syst.*, vol. 02, no. 03, pp. 279–291, Jul. 2014, doi: 10.1142/S2301385014400068.
- [9] C.-W. Hsu, S. Liu, F. Lu, C.-W. Chow, C.-H. Yeh, and G.-K. Chang, "Accurate Indoor Visible Light Positioning System utilizing Machine Learning Technique with Height Tolerance," *2018 Opt. Fiber Commun. Conf. Expo. OFC*, vol. 1, no. c, p. M2K.2, 2018, doi: 10.1364/ofc.2018.m2k.2.
- [10] J. Chung, M. Donahoe, C. Schmandt, I.-J. Kim, P. Razavai, and M. Wiseman, "Indoor location sensing using geo-magnetism," presented at the Proceedings of the 9th international conference on Mobile systems, applications, and services, 2011, pp. 141–154.
- [11] M. Youssef and A. Agrawala, "The Horus WLAN location determination system," presented at the Proceedings of the 3rd international conference on Mobile systems, applications, and services, 2005, pp. 205–218.
- [12] Y. Chen, D. Lymberopoulos, J. Liu, and B. Priyantha, "FM-based indoor localization," presented at the Proceedings of the 10th international conference on Mobile systems, applications, and services, 2012, pp. 169–182.
- [13] N. Chaudhary, O. I. Younus, L. N. Alves, Z. Ghassemlooy, S. Zvanovec, and H. Le-Minh, "An Indoor Visible Light Positioning System Using Tilted LEDs with High Accuracy," *Sensors*, vol. 21, no. 3, p. 920, Jan. 2021, doi: 10.3390/s21030920.
- [14] N. U. L. Hassan, M. Adeel Pasha, A. Naeem, and T. M. Jadoon, "Indoor Positioning Using Visible LED Lights: A Survey," *ACM Trans. Sens. Netw.*, vol. 11, no. 2, pp. 1–30, 2015, doi: 10.1145/0000000.0000000.
- [15] T.-H. Do and M. Yoo, "An in-Depth Survey of Visible Light Communication Based Positioning Systems," *Sensors*, vol. 16, no. 5, p. 678, May 2016, doi: 10.3390/s16050678.
- [16] T. H. Do and M. Yoo, "An in-Depth Survey of Visible Light Communication Based Positioning Systems," *Sens. Basel*, vol. 16, no. 5, 2016, doi: 10.3390/s16050678.
- [17] N. Chaudhary, L. N. Alves, and Z. Ghassemblooy, "Current Trends on Visible Light Positioning Techniques," presented at the 2019 2nd West Asian Colloquium on Optical Wireless Communications (WACOWC), Apr. 2019, pp. 100–105.

- [18] J. Rabadan, V. Guerra, C. Guerra, J. Rufo, and R. Perez-Jimenez, "A Novel Ranging Technique Based on Optical Camera Communications and Time Difference of Arrival," *Appl. Sci.*, vol. 9, no. 11, 2019, doi: 10.3390/app9112382.
- [19] A. Yassin *et al.*, "Recent Advances in Indoor Localization: A Survey on Theoretical Approaches and Applications," *IEEE Commun. Surv. Tutor.*, vol. 19, no. 2, pp. 1327–1346, 2017, doi: 10.1109/COMST.2016.2632427.
- [20] J. Luo, L. Fan, and H. Li, "Indoor Positioning Systems Based on Visible Light Communication: State of the Art," *IEEE Commun. Surv. Tutor.*, vol. 19, no. 4, pp. 2871–2893, 2017, doi: 10.1109/COMST.2017.2743228.
- [21] M. Maheepala, A. Z. Kouzani, and M. A. Joordens, "Light-Based Indoor Positioning Systems: A Review," *IEEE Sens. J.*, vol. 20, no. 8, pp. 3971–3995, 2020.
- [22] F. Dou, J. Lu, Z. Wang, X. Xiao, J. Bi, and C. -H. Huang, "Top-Down Indoor Localization with Wi-Fi Fingerprints Using Deep Q-Network," in *2018 IEEE 15th International Conference on Mobile Ad Hoc and Sensor Systems (MASS)*, Oct. 2018, pp. 166–174. doi: 10.1109/MASS.2018.00037.
- [23] S. Zhang, J. Guo, N. Luo, L. Wang, W. Wang, and K. Wen, "Improving Wi-Fi Fingerprint Positioning with a Pose Recognition-Assisted SVM Algorithm," *Remote Sens.*, vol. 11, no. 6, 2019, doi: 10.3390/rs11060652.
- [24] C. Liu, C. Wang, and J. Luo, "Large-Scale Deep Learning Framework on FPGA for Fingerprint-Based Indoor Localization," *IEEE Access*, vol. 8, pp. 65609–65617, 2020, doi: 10.1109/ACCESS.2020.2985162.
- [25] H. Elgala, R. Mesleh, and H. Haas, "Indoor optical wireless communication: potential and state-of-the-art," *IEEE Commun. Mag.*, vol. 49, no. 9, pp. 56–62, 2011.
- [26] J. Lee, S. Kim, and S. Han, "3D Visible Light Indoor Positioning by Bokeh Based Optical Intensity Measurement in Smartphone Camera," *IEEE Access*, vol. 7, pp. 91399–91406, 2019, doi: 10.1109/ACCESS.2019.2927356.
- [27] H. Cheng, C. Xiao, Y. Ji, J. Ni, and T. Wang, "A Single LED Visible Light Positioning System Based on Geometric Features and CMOS Camera," *IEEE Photonics Technol. Lett.*, pp. 1–1, 2020.
- [28] O. I. Younus *et al.*, "Data Rate Enhancement in Optical Camera Communications Using an Artificial Neural Network Equaliser," *IEEE Access*, vol. 8, pp. 42656–42665, 2020.
- [29] T. Akiyama, M. Sugimoto, and H. Hashizume, "Time-of-arrival-based smartphone localization using visible light communication," in *2017 International Conference on Indoor Positioning and Indoor Navigation (IPIN)*, Sapporo, Sep. 2017, pp. 1–7. doi: 10.1109/IPIN.2017.8115904.
- [30] M. Kinoshita *et al.*, "A Comparison of Reception Methods for Visible Light Communication Using High-Speed Stereo Cameras," in *2018 IEEE Global Communications Conference (GLOBECOM)*, Abu Dhabi, United Arab Emirates, Dec. 2018, pp. 1–5. doi: 10.1109/GLOCOM.2018.8647953.
- [31] A. Naz, H. M. Asif, T. Umer, S. Ayub, and F. Al-Turjman, "Trilateration-based indoor localization engineering technique for visible light communication system," *Softw. Pract. Exp.*, pp. 1–14, 2020, doi: 10.1002/spe.2823.
- [32] S. Zhang, P. Du, C. Chen, W.-D. Zhong, and A. Alphones, "Robust 3D Indoor VLP System Based on ANN Using Hybrid RSS/PDOA," *IEEE Access*, vol. 7, pp. 47769–47780, 2019, doi: 10.1109/ACCESS.2019.2909761.
- [33] H. Zhang *et al.*, "High-Precision Indoor Visible Light Positioning Using Deep Neural Network Based on the Bayesian Regularization With Sparse Training Point," *IEEE Photonics J.*, vol. 11, no. 3, pp. 1–10, Jun. 2019, doi: 10.1109/JPHOT.2019.2912156.
- [34] W. Gu, M. Aminikashani, P. Deng, and M. Kavehrad, "Impact of Multipath Reflections on the Performance of Indoor Visible Light Positioning Systems," *J. Light. Technol.*, vol. 34, no. 10, pp. 2578–2587, 2016, doi: 10.1109/JLT.2016.2541659.

- [35] T.-H. Do and M. Yoo, "Performance Analysis of Visible Light Communication Using CMOS Sensors," *Sensors*, vol. 16, no. 3, p. 309, 2016.
- [36] IC Insights, "A Market Analysis and Forecast for the Optoelectronics, Sensors/Actuators, and Discretes," May 2021. [Online]. Available: [icinsights.com](https://www.icinsights.com)
- [37] R. D. Roberts, "Undersampled frequency shift ON-OFF keying (UFSOOK) for camera communications (CamCom)," presented at the 2013 22nd Wireless and Optical Communication Conference, May 2013, pp. 645–648. doi: 10.1109/WOCC.2013.6676454.
- [38] P. Luo, Z. Ghassemlooy, H. Le Minh, X. Tang, and H.-M. Tsai, "Undersampled phase shift ON-OFF keying for camera communication," in *2014 Sixth International Conference on Wireless Communications and Signal Processing (WCSP)*, Hefei, China, Oct. 2014, pp. 1–6. doi: 10.1109/WCSP.2014.6992043.
- [39] P. Luo *et al.*, "Experimental Demonstration of RGB LED-Based Optical Camera Communications," *IEEE Photonics J.*, vol. 7, no. 5, pp. 1–12, 2015, doi: 10.1109/JPHOT.2015.2486680.
- [40] W. Wang, C. Chow, C. Chen, H. Hsieh, and Y. Chen, "Beacon Jointed Packet Reconstruction Scheme for Mobile-Phone Based Visible Light Communications Using Rolling Shutter," *IEEE Photonics J.*, vol. 9, no. 6, pp. 1–6, 2017, doi: 10.1109/JPHOT.2017.2762460.
- [41] S. Chen and C. Chow, "Color-Shift Keying and Code-Division Multiple-Access Transmission for RGB-LED Visible Light Communications Using Mobile Phone Camera," *IEEE Photonics J.*, vol. 6, no. 6, pp. 1–6, 2014, doi: 10.1109/JPHOT.2014.2374612.
- [42] H. Chen *et al.*, "Color-Shift Keying for Optical Camera Communication Using a Rolling Shutter Mode," *IEEE Photonics J.*, vol. 11, no. 2, pp. 1–8, 2019, doi: 10.1109/JPHOT.2019.2898909.
- [43] D. T. Nguyen, Y. Chae, and Y. Park, "Enhancement of Data Rate and Packet Size in Image Sensor Communications by Employing Constant Power 4-PAM," *IEEE Access*, vol. 6, pp. 8000–8010, 2018, doi: 10.1109/ACCESS.2018.2802948.
- [44] Pengfei Hu, Parth H. Pathak, Xiaotao Feng, Hao Fu, and Prasant Mohapatra, "ColorBars: increasing data rate of LED-to-camera communication using color shift keying," presented at the Proceedings of the 11th ACM Conference on Emerging Networking Experiments and Technologies, 2015, pp. 1–13. doi: 10.1145/2716281.2836097.
- [45] W. Huang, P. Tian, and Z. Xu, "Design and implementation of a real-time CIM-MIMO optical camera communication system," *Opt. Express*, vol. 24, no. 21, pp. 24567–24579, Oct. 2016, doi: 10.1364/OE.24.024567.
- [46] Y. Goto *et al.*, "A New Automotive VLC System Using Optical Communication Image Sensor," *IEEE Photonics J.*, vol. 8, no. 3, pp. 1–17, 2016, doi: 10.1109/JPHOT.2016.2555582.
- [47] H. Liu, H. Darabi, P. Banerjee, and J. Liu, "Survey of Wireless Indoor Positioning Techniques and Systems," *IEEE Trans. Syst. Man Cybern. Part C Appl. Rev.*, vol. 37, no. 6, pp. 1067–1080, Nov. 2007, doi: 10.1109/TSMCC.2007.905750.
- [48] IC Insights, "IoT Analytics," Nov. 2020. Accessed: Jan. 31, 2022. [Online]. Available: <https://www.statista.com/statistics/1101442/iot-number-of-connected-devices-worldwide/>
- [49] M. Z. Chowdhury, T. Hossan, A. Islam, and Y. M. Jang, "A Comparative Survey of Optical Wireless Technologies: Architectures and Applications," vol. 6, p. 22, 2018.
- [50] C. T. Nguyen *et al.*, "Enabling and Emerging Technologies for Social Distancing: A Comprehensive Survey and Open Problems," *IEEE Access*, vol. 8, pp. 153479–153507, 2020, doi: 10.1109/ACCESS.2020.3018140.
- [51] T. L. Vu, T. Nguyen, C. S. Kim, E. B. Sin, J. Jeong, and Y. M. Jang, "Survey of indoor optical camera communication (OCC) systems for the Internet of lights," in *2017 International Conference on Information and Communication Technology Convergence (ICTC)*, Jeju, Oct. 2017, pp. 700–703. doi: 10.1109/ICTC.2017.8190758.

- [52] M. A. Dawood, S. S. Saleh, E.-S. A. El-Badawy, and M. H. Aly, "A comparative analysis of localization algorithms for visible light communication," *Opt. Quantum Electron.*, vol. 53, no. 2, p. 108, Feb. 2021, doi: 10.1007/s11082-021-02751-z.
- [53] J. Xiao, Z. Zhou, Y. Yi, and L. M. Ni, "A survey on wireless indoor localization from the device perspective," *ACM Comput. Surv. CSUR*, vol. 49, no. 2, pp. 1–31, 2016.
- [54] R. F. Brena, J. P. García-Vázquez, C. E. Galván-Tejada, D. Muñoz-Rodríguez, C. Vargas-Rosales, and J. Fangmeyer, "Evolution of Indoor Positioning Technologies: A Survey," *J. Sens.*, vol. 2017, p. 2630413, Mar. 2017, doi: 10.1155/2017/2630413.
- [55] A. Pérez-Navarro *et al.*, "1 - Challenges of Fingerprinting in Indoor Positioning and Navigation," in *Geographical and Fingerprinting Data to Create Systems for Indoor Positioning and Indoor/Outdoor Navigation*, J. Conesa, A. Pérez-Navarro, J. Torres-Sospedra, and R. Montoliu, Eds. Academic Press, 2019, pp. 1–20. doi: 10.1016/B978-0-12-813189-3.00001-0.
- [56] P. Davidson and R. Piché, "A Survey of Selected Indoor Positioning Methods for Smartphones," *IEEE Commun. Surv. Tutor.*, vol. 19, no. 2, pp. 1347–1370, Secondquarter 2017, doi: 10.1109/COMST.2016.2637663.
- [57] J. Armstrong, Y. Sekercioglu, and A. Neild, "Visible light positioning: a roadmap for international standardization," *IEEE Commun. Mag.*, vol. 51, no. 12, pp. 68–73, Dec. 2013, doi: 10.1109/MCOM.2013.6685759.
- [58] A. Poullose, J. Kim, and D. S. Han, "A Sensor Fusion Framework for Indoor Localization Using Smartphone Sensors and Wi-Fi RSSI Measurements," *Appl. Sci.*, vol. 9, no. 20, p. 4379, Oct. 2019, doi: 10.3390/app9204379.
- [59] J. Rabadan, V. Guerra, R. Rodríguez, J. Rufo, M. Luna-Rivera, and R. Perez-Jimenez, "Hybrid Visible Light and Ultrasound-Based Sensor for Distance Estimation," *Sensors*, vol. 17, no. 2, p. 330, Feb. 2017, doi: 10.3390/s17020330.
- [60] M. Z. Chowdhury, M. T. Hossan, A. Islam, and Y. M. Jang, "A Comparative Survey of Optical Wireless Technologies: Architectures and Applications," *IEEE Access*, vol. 6, pp. 9819–9840, 2018, doi: 10.1109/ACCESS.2018.2792419.
- [61] Z. Ghassemlooy, P. Luo, and S. Zvanovec, "Optical Camera Communications," in *Optical Wireless Communications*, M. Uysal, C. Capsoni, Z. Ghassemlooy, A. Boucouvalas, and E. Udvary, Eds. Cham: Springer International Publishing, 2016, pp. 547–568. doi: 10.1007/978-3-319-30201-0_25.
- [62] W. A. Cahyadi, Y. H. Chung, Z. Ghassemlooy, and N. B. Hassan, "Optical Camera Communications: Principles, Modulations, Potential and Challenges," *Electronics*, vol. 9, no. 9, 2020, doi: 10.3390/electronics9091339.
- [63] G. M. Mendoza-Silva, J. Torres-Sospedra, and J. Huerta, "A Meta-Review of Indoor Positioning Systems," *Sensors*, vol. 19, no. 20, 2019, doi: 10.3390/s19204507.
- [64] N. Q. Pham, K. Mekonnen, E. Tangdiongga, A. Mefleh, and T. Koonen, "User Localization and Upstream Signaling for Beam-Steered Infrared Light Communication System," *IEEE Photonics Technol. Lett.*, vol. 33, no. 11, pp. 545–548, Jun. 2021, doi: 10.1109/LPT.2021.3075080.
- [65] HTC Corporation, "Discover Virtual Reality Beyond Imagination," *Vive. VIVE™*, 2018. <https://www.vive.com/us/>
- [66] Z. Zhang, "Microsoft kinect sensor and its effect," *IEEE Multimed.*, vol. 19, no. 2, pp. 4–10, 2012.
- [67] N. Chaudhary, L. N. Alves, and Z. Ghassemblooy, "Current Trends on Visible Light Positioning Techniques," *2019 2nd West Asian Colloq. Opt. Wirel. Commun. WACOWC*, pp. 100–105, 2019, doi: 10.1109/wacowc.2019.8770211.
- [68] B. W. Parkinson and J. J. Spilker, *Progress in astronautics and aeronautics: Global positioning system: Theory and applications*, vol. 164. Aiaa, 1996.

- [69] L. Antsfeld, B. Chidlovskii, and E. Sansano-Sansano, "Deep Smartphone Sensors-WiFi Fusion for Indoor Positioning and Tracking," *ArXiv201110799 Cs*, Nov. 2020, Accessed: Dec. 09, 2020. [Online]. Available: <http://arxiv.org/abs/2011.10799>
- [70] F. Qin, T. Zuo, and X. Wang, "CCpos: WiFi Fingerprint Indoor Positioning System Based on CDAE-CNN," *Sensors*, vol. 21, no. 4, p. 1114, Feb. 2021, doi: 10.3390/s21041114.
- [71] Y. Wang, X. Yang, Y. Zhao, Y. Liu, and L. Cuthbert, "Bluetooth positioning using RSSI and triangulation methods," presented at the 2013 IEEE 10th Consumer Communications and Networking Conference (CCNC), 2013, pp. 837–842.
- [72] A. Baniukevic, D. Sabonis, C. S. Jensen, and H. Lu, "Improving wi-fi based indoor positioning using bluetooth add-ons," presented at the 2011 IEEE 12th International Conference on Mobile Data Management, 2011, vol. 1, pp. 246–255.
- [73] S. Gezici *et al.*, "Localization via ultra-wideband radios: a look at positioning aspects for future sensor networks," *IEEE Signal Process. Mag.*, vol. 22, no. 4, pp. 70–84, Jul. 2005, doi: 10.1109/MSP.2005.1458289.
- [74] S. Gezici *et al.*, "Localization via ultra-wideband radios: a look at positioning aspects for future sensor networks," *IEEE Signal Process. Mag.*, vol. 22, no. 4, pp. 70–84, Jul. 2005, doi: 10/bxh37p.
- [75] C. Schönegger, M. E. Wernle, and B. Stadlmann, "Analysis of an UHF RFID System for interior position sensing," presented at the 4th European Workshop on RFID Systems and Technologies, 2008, pp. 1–5.
- [76] J. Shen, C. Jin, and D. Liu, "A survey on the research of indoor RFID positioning system," presented at the International conference on cloud computing and security, 2016, pp. 264–274.
- [77] W. A. Cahyadi and Y. H. Chung, "Experimental demonstration of indoor uplink near-infrared LED camera communication," p. 8, 2018.
- [78] D. R. Dhatchayeny, S. Arya, and Y. H. Chung, "Infrared-Based Multiple-Patient Monitoring in Indoor Optical Wireless Healthcare Systems," *IEEE Sens. J.*, vol. 19, no. 14, pp. 5594–5599, Jul. 2019, doi: 10.1109/JSEN.2019.2906898.
- [79] S. Bastiaens, W. Raes, N. Stevens, L. Martens, W. Joseph, and D. Plets, "Impact of a Photodiode's Angular Characteristics on RSS-Based VLP Accuracy," *IEEE Access*, vol. 8, pp. 83116–83130, 2020, doi: 10.1109/ACCESS.2020.2991298.
- [80] N. Chaudhary, L. N. Alves, and Z. Ghassemloooy, "Current Trends on Visible Light Positioning Techniques," in *2019 2nd West Asian Colloquium on Optical Wireless Communications (WACOWC)*, Tehran, Iran, Apr. 2019, pp. 100–105. doi: 10.1109/WACOWC.2019.8770211.
- [81] S.-Y. Jung, S. Hann, S. Park, and C.-S. Park, "Optical wireless indoor positioning system using light emitting diode ceiling lights," *Microw. Opt. Technol. Lett.*, vol. 54, no. 7, pp. 1622–1626, Jul. 2012, doi: 10.1002/mop.26880.
- [82] J. Lim, "Ubiquitous 3D positioning systems by led-based visible light communications," *IEEE Wirel. Commun.*, vol. 22, no. 2, pp. 80–85, Apr. 2015, doi: 10.1109/MWC.2015.7096289.
- [83] G. Kail, P. Maechler, N. Preyss, and A. Burg, "Robust asynchronous indoor localization using LED lighting," in *2014 IEEE International Conference on Acoustics, Speech and Signal Processing (ICASSP)*, Florence, Italy, May 2014, pp. 1866–1870. doi: 10.1109/ICASSP.2014.6853922.
- [84] J. Vongkulbhisal, B. Chantaramolee, Y. Zhao, and W. S. Mohammed, "A fingerprinting-based indoor localization system using intensity modulation of light emitting diodes," *Microw. Opt. Technol. Lett.*, vol. 54, no. 5, pp. 1218–1227, May 2012, doi: 10.1002/mop.26763.
- [85] M. Biagi, A. M. Vegni, and T. D. C. Little, "LAT indoor MIMO-VLC — Localize, access and transmit," in *2012 International Workshop on Optical Wireless Communications (IWOW)*, Oct. 2012, pp. 1–3. doi: 10.1109/IWOW.2012.6349698.

- [86] S. Hann, J. Kim, S. Jung, and C. Park, "White LED ceiling lights positioning systems for optical wireless indoor applications," in *36th European Conference and Exhibition on Optical Communication*, Sep. 2010, pp. 1–3. doi: 10.1109/ECOC.2010.5621490.
- [87] S.-H. Yang, D.-R. Kim, H.-S. Kim, Y.-H. Son, and S.-K. Han, "Indoor positioning system based on visible light using location code," in *2012 Fourth International Conference on Communications and Electronics (ICCE)*, Hue, Vietnam, Aug. 2012, pp. 360–363. doi: 10.1109/CCE.2012.6315928.
- [88] S.-H. Yang, D.-R. Kim, H.-S. Kim, Y.-H. Son, and S.-K. Han, "Visible light based high accuracy indoor localization using the extinction ratio distributions of light signals," *Microw. Opt. Technol. Lett.*, vol. 55, no. 6, pp. 1385–1389, Jun. 2013, doi: 10.1002/mop.27575.
- [89] A. M. Vegni and M. Biagi, "An indoor localization algorithm in a small-cell LED-based lighting system," in *2012 International Conference on Indoor Positioning and Indoor Navigation (IPIN)*, Nov. 2012, pp. 1–7. doi: 10.1109/IPIN.2012.6418887.
- [90] M. Yoshino, S. Haruyama, and M. Nakagawa, "High-Accuracy Positioning System Using Visible LED Lights and Image Sensor," p. 4, 2008.
- [91] T. Tanaka and S. Haruyama, "New Position Detection Method Using Image Sensor and Visible Light LEDs," presented at the 2009 Second International Conference on Machine Vision, Dec. 2009, pp. 150–153. doi: 10.1109/ICMV.2009.44.
- [92] W. Guan, S. Wen, L. Liu, and H. Zhang, "High-precision indoor positioning algorithm based on visible light communication using complementary metal–oxide–semiconductor image sensor," *Opt. Eng.*, vol. 58, no. 2, p. 024101, 2019.
- [93] K. Byung Yeon, C. Jung-Sik, P. Youngil, and K. Ki-Doo, "Implementation of indoor positioning using LED and dual PC cameras," presented at the 2012 Fourth International Conference on Ubiquitous and Future Networks (ICUFN), Jul. 2012, pp. 476–477. doi: 10.1109/ICUFN.2012.6261753.
- [94] Y. Wang, Y. Gong, and Z. Shi, "Research on the Collinear Equation Model of Visual Positioning Based on Visible Light Communication," *MATEC Web Conf.*, vol. 22, p. 02003, 2015, doi: 10.1051/mateconf/20152202003.
- [95] D. Zheng, R. Vanitsthan, G. Chen, and J. A. Farrell, "LED-based initialization and navigation," in *2013 American Control Conference*, Jun. 2013, pp. 6199–6205. doi: 10.1109/ACC.2013.6580810.
- [96] M. S. Rahman, M. M. Haque, and K. Ki-Doo, "High precision indoor positioning using lighting LED and image sensor," presented at the 14th International Conference on Computer and Information Technology (ICCIT 2011), Dec. 2011, pp. 309–314. doi: 10.1109/ICCITech.2011.6164805.
- [97] Y. Zhuang *et al.*, "A Survey of Positioning Systems Using Visible LED Lights," *IEEE Commun. Surv. Tutor.*, vol. 20, no. 3, pp. 1963–1988, 2018, doi: 10.1109/COMST.2018.2806558.
- [98] N. Rajagopal, P. Lazik, and A. Rowe, "Visual light landmarks for mobile devices," presented at the IPSN-14 Proceedings of the 13th International Symposium on Information Processing in Sensor Networks, Apr. 2014, pp. 249–260. doi: 10.1109/IPSN.2014.6846757.
- [99] M. Nakajima and S. Haruyama, "New indoor navigation system for visually impaired people using visible light communication," *EURASIP J. Wirel. Commun. Netw.*, vol. 2013, no. 1, p. 37, Feb. 2013, doi: 10.1186/1687-1499-2013-37.
- [100] G. del Campo-Jimenez, J. M. Perandones, and F. J. Lopez-Hernandez, "A VLC-based beacon location system for mobile applications," in *2013 International Conference on Localization and GNSS (ICL-GNSS)*, Jun. 2013, pp. 1–4. doi: 10.1109/ICL-GNSS.2013.6577276.
- [101] Y. U. Lee and M. Kavehrad, "Two hybrid positioning system design techniques with lighting LEDs and ad-hoc wireless network," *IEEE Trans. Consum. Electron.*, vol. 58, no. 4, pp. 1176–1184, Nov. 2012, doi: 10.1109/TCE.2012.6414983.

- [102] C. Sertthin, E. Tsuji, M. Nakagawa, S. Kuwano, and K. Watanabe, "A Switching Estimated Receiver Position Scheme For Visible Light Based Indoor Positioning System," in *2009 4th International Symposium on Wireless Pervasive Computing*, Feb. 2009, pp. 1–5. doi: 10.1109/ISWPC.2009.4800561.
- [103] C. Sertthin, T. Fujii, O. Takyu, Y. Umeda, and T. Ohtsuki, "On Physical Layer Simulation Model for 6-Axis Sensor Assisted VLC Based Positioning System," in *2011 IEEE Global Telecommunications Conference - GLOBECOM 2011*, Dec. 2011, pp. 1–5. doi: 10.1109/GLOCOM.2011.6134119.
- [104] Y. U. Lee and M. Kavehrad, "Long-range indoor hybrid localization system design with visible light communications and wireless network," in *2012 IEEE Photonics Society Summer Topical Meeting Series*, Seattle, WA, USA, Jul. 2012, pp. 82–83. doi: 10.1109/PHOSST.2012.6280712.
- [105] N. Chaudhary, L. N. Alves, and Z. Ghassemblooy, "Impact of Transmitter Positioning Uncertainty on RSS-based Visible Light Positioning Accuracy," presented at the 12th International Symposium on Communication Systems, Networks & Digital Signal Processing (CSNDSP), Porto, 2020.
- [106] A. Arafa, S. Dalmiya, R. Klukas, and J. F. Holzman, "Angle-of-arrival reception for optical wireless location technology," *Opt. Express*, vol. 23, no. 6, p. 7755, Mar. 2015, doi: 10.1364/OE.23.007755.
- [107] H. Steendam, T. Q. Wang, and J. Armstrong, "Cramer-Rao bound for AOA-based VLP with an aperture-based receiver," *IEEE Int. Conf. Commun.*, pp. 1–6, 2017, doi: 10.1109/ICC.2017.7996691.
- [108] M. Vieira, R. Costa, A. Pereira, and P. Fonseca, "A Validation Framework for Visible Light Positioning in Mobile Robotics," *Proc. - 2016 Int. Conf. Auton. Robot Syst. Compet. ICARSC 2016*, pp. 47–52, 2016, doi: 10.1109/ICARSC.2016.25.
- [109] J. Yan and B. Zhu, "A visible light communication indoor localization algorithm in rotated environments," *IEEE CITS 2016 - 2016 Int. Conf. Comput. Inf. Telecommun. Syst.*, pp. 1–4, 2016, doi: 10.1109/CITS.2016.7546430.
- [110] B. Zhu, J. Cheng, Y. Wang, J. Yan, and J. Wang, "Three-Dimensional VLC Positioning Based on Angle Difference of Arrival with Arbitrary Tilting Angle of Receiver," *IEEE J. Sel. Areas Commun.*, vol. 36, no. 1, pp. 8–22, 2018, doi: 10.1109/JSAC.2017.2774435.
- [111] B. Zhu, Z. Zhu, Y. Wang, and J. Cheng, "Optimal Optical Omnidirectional Angle-of-Arrival Estimator With Complementary Photodiodes," *J. Light. Technol.*, vol. PP, no. c, pp. 1–1, 2019, doi: 10.1109/jlt.2019.2907969.
- [112] Z. Zhu, B. Zhu, Y. Wang, Z. Shi, and Y. Jiang, "Angle-of-Arrival Estimator for Light Signals Based on Optimized Photodiode Array," *2019 Int. Conf. Comput. Netw. Commun. ICNC 2019*, pp. 62–66, 2019, doi: 10.1109/ICNC.2019.8685534.
- [113] J. Yan, B. Zhu, L. Chen, J. Wang, and J. Liu, "Error Analysis on Indoor Localization with Visible Light Communication," *Remote Sens.*, vol. 11, no. 4, p. 427, 2019, doi: 10.3390/rs11040427.
- [114] Y.-S. Kuo, P. Pannuto, K.-J. Hsiao, and P. Dutta, "Luxapose:Indoor Positioning with Mobile Phones and Visible Light," *Proc. 20th Annu. Int. Conf. Mob. Comput. Netw. - MobiCom 14*, pp. 447–458, 2014, doi: 10.1145/2639108.2639109.
- [115] L. Yin, X. Wu, and H. Haas, "Indoor visible light positioning with angle diversity transmitter," *2015 IEEE 82nd Veh. Technol. Conf. VTC Fall 2015 - Proc.*, pp. 1–5, 2015, doi: 10.1109/VTCFall.2015.7390984.
- [116] S. Cincotta, A. Neild, C. He, and J. Armstrong, "Visible light positioning using an aperture and a quadrant photodiode," *2017 IEEE Globecom Workshop GC Wkshps 2017 - Proc.*, vol. 2017, pp. 1–6, 2017, doi: 10.1109/GLOCOMW.2017.8269150.

- [117] S. Bastiaens and H. Steendam, "Coarse estimation of the incident angle for VLP with an aperture-based receiver," *2017 14th Workshop Position. Navig. Commun. WPNC 2017*, pp. 1–6, 2017, doi: 10.1109/WPNC.2017.8250050.
- [118] T. Tanaka and S. Haruyama, "New position detection method using image sensor and visible light LEDs," *2009 2nd Int. Conf. Mach. Vis. ICMV 2009*, pp. 150–153, 2009, doi: 10.1109/ICMV.2009.44.
- [119] Z. Yang, Z. Wang, J. Zhang, C. Huang, and Q. Zhang, "Wearables can afford: Light-weight indoor positioning with visible light," presented at the Proceedings of the 13th Annual International Conference on Mobile Systems, Applications, and Services, 2015, pp. 317–330.
- [120] M. Yasir, S. Ho, and B. N. Vellambi, "Indoor localization using visible light and accelerometer," in *2013 IEEE Global Communications Conference (GLOBECOM)*, Dec. 2013, pp. 3341–3346. doi: 10.1109/GLOCOM.2013.6831588.
- [121] M. Yasir, S.-W. Ho, and B. N. Vellambi, "Indoor Positioning System Using Visible Light and Accelerometer," *J. Light. Technol.*, vol. 32, no. 19, pp. 3306–3316, Oct. 2014, doi: 10.1109/JLT.2014.2344772.
- [122] Seongsu Lee and Sung-Yoon Jung, "Location awareness using Angle-of-arrival based circular-PD-array for visible light communication," in *2012 18th Asia-Pacific Conference on Communications (APCC)*, Oct. 2012, pp. 480–485. doi: 10.1109/APCC.2012.6388185.
- [123] X. Sun, Y. Zou, J. Duan, and A. Shi, "The positioning accuracy analysis of AOA-based indoor visible light communication system," in *2015 International Conference on Optoelectronics and Microelectronics (ICOM)*, Jul. 2015, pp. 186–190. doi: 10.1109/ICoOM.2015.7398801.
- [124] Y. S. Erogluy, I. Guvency, N. Palay, and M. Yukselz, "AOA-based localization and tracking in multi-element VLC systems," *2015 IEEE 16th Annu. Wirel. Microw. Technol. Conf. WAMICON 2015*, pp. 1–5, 2015, doi: 10.1109/WAMICON.2015.7120424.
- [125] C. Sertthin and E. Tsuji, "A Switching Estimated Receiver Position Scheme For Visible Light Based Indoor Positioning System," 2009.
- [126] G. B. Prince and T. D. C. Little, "A two phase hybrid RSS/AoA algorithm for indoor device localization using visible light," in *2012 IEEE Global Communications Conference (GLOBECOM)*, Dec. 2012, pp. 3347–3352. doi: 10.1109/GLOCOM.2012.6503631.
- [127] J. Herrnsdorf, M. J. Strain, E. Gu, R. K. Henderson, and M. D. Dawson, "Positioning and Space-Division Multiple Access Enabled by Structured Illumination With Light-Emitting Diodes," *J. Light. Technol.*, vol. 35, no. 12, pp. 2339–2345, Jun. 2017, doi: 10.1109/JLT.2017.2672864.
- [128] M. T. Taylor and S. Hranilovic, "Angular diversity approach to indoor positioning using visible light," in *2013 IEEE Globecom Workshops (GC Wkshps)*, Atlanta, GA, Dec. 2013, pp. 1093–1098. doi: 10.1109/GLOCOMW.2013.6825138.
- [129] G. Cossu, M. Presi, R. Corsini, P. Choudhury, A. M. Khalid, and E. Ciaramella, "A Visible Light localization aided Optical Wireless system," in *2011 IEEE GLOBECOM Workshops (GC Wkshps)*, Dec. 2011, pp. 802–807. doi: 10.1109/GLOCOMW.2011.6162565.
- [130] X. Liu, H. Makino, and Y. Maeda, "Basic study on indoor location estimation using Visible Light Communication platform," in *2008 30th Annual International Conference of the IEEE Engineering in Medicine and Biology Society*, Aug. 2008, pp. 2377–2380. doi: 10.1109/IEMBS.2008.4649677.
- [131] C. Amini, A. Taherpour, T. Khattab, and S. Gazor, "On the more accurate channel model and positioning based on time-of-arrival for visible light localization," *Opt. Eng.*, vol. 56, no. 1, p. 016110, 2017, doi: 10.1117/1.oe.56.1.016110.
- [132] T. Akiyama, M. Sugimoto, and H. Hashizume, "Time-of-arrival-based smartphone localization using visible light communication," *2017 Int. Conf. Indoor Position. Indoor Navig. IPIN 2017*, vol. 2017-Janua, pp. 1–7, 2017, doi: 10.1109/IPIN.2017.8115904.

- [133] T.-H. Do and M. Yoo, "An in-Depth Survey of Visible Light Communication Based Positioning Systems," *Sensors*, vol. 16, no. 5, p. 678, May 2016, doi: 10.3390/s16050678.
- [134] T. Q. Wang, Y. A. Sekercioglu, A. Neild, and J. Armstrong, "Position accuracy of time-of-arrival based ranging using visible light with application in indoor localization systems," *J. Light. Technol.*, vol. 31, no. 20, pp. 3302–3308, 2013, doi: 10.1109/JLT.2013.2281592.
- [135] Yiu-Tong Chan, Wing-Yue Tsui, Hing-Cheung So, and Pak-chung Ching, "Time-of-arrival based localization under NLOS conditions," *IEEE Trans. Veh. Technol.*, vol. 55, no. 1, pp. 17–24, Jan. 2006, doi: 10.1109/TVT.2005.861207.
- [136] T.-H. Do and M. Yoo, "TDOA-based indoor positioning using visible light," *Photonic Netw. Commun.*, vol. 27, no. 2, pp. 80–88, Apr. 2014, doi: 10.1007/s11107-014-0428-4.
- [137] K. Panta and J. Armstrong, "Indoor localisation using white LEDs," *Electron. Lett.*, vol. 48, no. 4, pp. 228–230, 2012.
- [138] S.-Y. Jung, S. Hann, and C.-S. Park, "TDOA-based optical wireless indoor localization using LED ceiling lamps," *IEEE Trans. Consum. Electron.*, vol. 57, no. 4, pp. 1592–1597, Nov. 2011, doi: 10.1109/TCE.2011.6131130.
- [139] Young Hoon Choi, In Hwan Park, Yoon Hyun Kim, and J. Y. Kim, "Novel LBS technique based on visible light communications," in *2012 IEEE International Conference on Consumer Electronics (ICCE)*, Jan. 2012, pp. 576–577. doi: 10.1109/ICCE.2012.6161980.
- [140] J. H. Y. Nah, R. Parthiban, and M. H. Jaward, "Visible Light Communications localization using TDOA-based coherent heterodyne detection," in *2013 IEEE 4th International Conference on Photonics (ICP)*, Melaka, Malaysia, Oct. 2013, pp. 247–249. doi: 10.1109/ICP.2013.6687128.
- [141] T. Q. Wang, Y. A. Sekercioglu, A. Neild, and J. Armstrong, "Position Accuracy of Time-of-Arrival Based Ranging Using Visible Light With Application in Indoor Localization Systems," *J. Light. Technol.*, vol. 31, no. 20, pp. 3302–3308, Oct. 2013, doi: 10.1109/JLT.2013.2281592.
- [142] K. Wang, A. Nirmalathas, C. Lim, and E. Skafidas, "Optical Wireless-Based Indoor Localization System Employing a Single-Channel Imaging Receiver," *J. Light. Technol.*, vol. 34, no. 4, p. 9, 2016.
- [143] H. S. Kim, D. R. Kim, S. H. Yang, Y. H. Son, and S. K. Han, "An indoor visible light communication positioning system using a RF carrier allocation technique," *J. Light. Technol.*, vol. 31, no. 1, pp. 134–144, 2013, doi: 10.1109/JLT.2012.2225826.
- [144] H. Zheng, Z. Xu, C. Yu, and M. Gurusamy, "Indoor three-dimensional positioning based on visible light communication using Hamming filter," *Opt. InfoBase Conf. Pap.*, vol. 2016, pp. 4–6, 2016, doi: 10.1364/sppcom.2016.spm4e.3.
- [145] X. L. Xiang Liu, A. Y. Aiying Yang, Y. W. Yu Wang, and L. F. and Lihui Feng, "Combination of light-emitting diode positioning identification and time-division multiplexing scheme for indoor location-based service," *Chin. Opt. Lett.*, vol. 13, no. 12, pp. 120601–120606, 2015, doi: 10.3788/col201513.120601.
- [146] T. H. Do and M. Yoo, "An in-depth survey of visible light communication based positioning systems," *Sens. Switz.*, vol. 16, no. 5, 2016, doi: 10.3390/s16050678.
- [147] M. Aminikashani, W. Gu, and M. Kavehrad, "Indoor location estimation with optical-based orthogonal frequency division multiplexing communications," *Opt. Eng.*, vol. 55, no. 5, p. 056116, May 2016, doi: 10.1117/1.OE.55.5.056116.
- [148] X. Zhang, J. Duan, Y. Fu, and A. Shi, "Theoretical Accuracy Analysis of Indoor Visible Light Communication Positioning System Based on Received Signal Strength Indicator," *J. Light. Technol.*, vol. 32, no. 21, pp. 4180–4186, Nov. 2014, doi: 10.1109/JLT.2014.2349530.
- [149] M. Rahaim, G. B. Prince, and T. D. C. Little, "State estimation and motion tracking for spatially diverse VLC networks," in *2012 IEEE Globecom Workshops*, Anaheim, CA, USA, Dec. 2012, pp. 1249–1253. doi: 10.1109/GLOCOMW.2012.6477760.

- [150] W. Gu, W. Zhang, J. Wang, M. R. Amini Kashani, and M. Kavehrad, "Three dimensional indoor positioning based on visible light with Gaussian mixture sigma-point particle filter technique," presented at the SPIE OPTO, San Francisco, California, United States, Feb. 2015, p. 93870O. doi: 10.1117/12.2076607.
- [151] W. Gu, M. Aminikashani, P. Deng, and M. Kavehrad, "Impact of Multipath Reflections on the Performance of Indoor Visible Light Positioning Systems," *J. Light. Technol.*, vol. 34, no. 10, pp. 2578–2587, May 2016, doi: 10.1109/JLT.2016.2541659.
- [152] W. Gu, M. Aminikashani, and M. Kavehrad, "Indoor visible light positioning system with multipath reflection analysis," in *2016 IEEE International Conference on Consumer Electronics (ICCE)*, Las Vegas, NV, USA, Jan. 2016, pp. 89–92. doi: 10.1109/ICCE.2016.7430533.
- [153] N. A. Mohammed and M. A. Elkarim, "Exploring the effect of diffuse reflection on indoor localization systems based on RSSI-VLC," *Opt. Express*, vol. 23, no. 16, p. 20297, Aug. 2015, doi: 10.1364/OE.23.020297.
- [154] Y. Zhuang *et al.*, "A Survey of Positioning Systems Using Visible LED Lights," *IEEE Commun. Surv. Tutor.*, vol. 20, no. 3, pp. 1963–1988, 2018, doi: 10.1109/COMST.2018.2806558.
- [155] M. Yasir, S.-W. Ho, and B. N. Vellambi, "Indoor Position Tracking Using Multiple Optical Receivers," *J. Light. Technol.*, vol. 34, no. 4, pp. 1166–1176, Feb. 2016, doi: 10.1109/JLT.2015.2507182.
- [156] S.-K. Han, E.-M. Jeong, S.-H. Yang, and H.-S. Kim, "Tilted receiver angle error compensated indoor positioning system based on visible light communication," *Electron. Lett.*, vol. 49, no. 14, pp. 890–892, Jul. 2013, doi: 10.1049/el.2013.1368.
- [157] H.-S. Kim, D.-R. Kim, S.-H. Yang, Y.-H. Son, and S.-K. Han, "An Indoor Visible Light Communication Positioning System Using a RF Carrier Allocation Technique," *J. Light. Technol.*, vol. 31, no. 1, pp. 134–144, Jan. 2013, doi: 10.1109/JLT.2012.2225826.
- [158] L. Li, P. Hu, C. Peng, G. Shen, and F. Zhao, "Epsilon: A visible light based positioning system," presented at the 11th USENIX Symposium on Networked Systems Design and Implementation (NSDI 14), 2014, pp. 331–343.
- [159] W. Zhang, M. I. S. Chowdhury, and M. Kavehrad, "Asynchronous indoor positioning system based on visible light communications," *Opt. Eng.*, vol. 53, no. 4, p. 045105, Apr. 2014, doi: 10.1117/1.OE.53.4.045105.
- [160] Hyun-Seung Kim, Deok-Rae Kim, Se-Hoon Yang, Yong-Hwan Son, and Sang-Kook Han, "Inter-cell interference mitigation and indoor positioning system based on carrier allocation visible light communication," in *2011 5th International Conference on Signal Processing and Communication Systems (ICSPCS)*, Dec. 2011, pp. 1–7. doi: 10.1109/ICSPCS.2011.6140854.
- [161] Z. Zhou, "Indoor positioning algorithm using light-emitting diode visible light communications," *Opt. Eng.*, vol. 51, no. 8, p. 085009, Aug. 2012, doi: 10.1117/1.OE.51.8.085009.
- [162] P. Luo, M. Zhang, Z. Ghassemlooy, S. Zvanovec, S. Feng, and P. Zhang, "Undersampled-Based Modulation Schemes for Optical Camera Communications," *IEEE Commun. Mag.*, vol. 56, no. 2, pp. 204–212, 2018, doi: 10.1109/mcom.2018.1601017.
- [163] N. T. Le and Y. M. Jang, "Photography Trilateration Indoor Localization with Image Sensor Communication," *Sensors*, vol. 19, no. 15, 2019, doi: 10.3390/s19153290.
- [164] M. Shahjalal, M. Hossan, M. Hasan, M. Z. Chowdhury, N. T. Le, and Y. M. Jang, "An implementation approach and performance analysis of image sensor based multilateral indoor localization and navigation system," *Wirel. Commun. Mob. Comput.*, vol. 2018, 2018.
- [165] H. Huang, B. Lin, L. Feng, and H. Lv, "Hybrid indoor localization scheme with image sensor-based visible light positioning and pedestrian dead reckoning," *Appl. Opt.*, vol. 58, no. 12, pp. 3214–3221, Apr. 2019, doi: 10.1364/AO.58.003214.

- [166] Y. Ji *et al.*, "A single LED lamp positioning system based on CMOS camera and visible light communication," *Opt. Commun.*, vol. 443, pp. 48–54, Jul. 2019, doi: <https://doi.org/10.1016/j.optcom.2019.03.002>.
- [167] H. Cheng, C. Xiao, Y. Ji, J. Ni, and T. Wang, "A Single LED Visible Light Positioning System Based on Geometric Features and CMOS Camera," *IEEE Photonics Technol. Lett.*, vol. 32, no. 17, pp. 1097–1100, Sep. 2020, doi: 10.1109/LPT.2020.3012476.
- [168] J. Hao, J. Chen, and R. Wang, "Visible Light Positioning Using A Single LED Luminaire," *IEEE Photonics J.*, vol. 11, no. 5, pp. 1–13, Oct. 2019, doi: 10.1109/JPHOT.2019.2930209.
- [169] Zhong Zheng, Lu Liu, Che Zhao, and Weiwei Hu, "High accuracy indoor positioning scheme using single LED and camera," *Electron. Lett.*, vol. 54, no. 4, pp. 227–229, 2018.
- [170] J. Lee, S. Kim, and S. Han, "3D Visible Light Indoor Positioning by Bokeh Based Optical Intensity Measurement in Smartphone Camera," *IEEE Access*, vol. 7, pp. 91399–91406, 2019, doi: 10.1109/ACCESS.2019.2927356.
- [171] J. Hao, J. Chen, and R. Wang, "Visible Light Positioning Using A Single LED Luminaire," *IEEE Photonics J.*, vol. 11, no. 5, pp. 1–13, 2019, doi: 10.1109/JPHOT.2019.2930209.
- [172] W. Guan, L. Huang, B. Hussain, and C. Patrick Yue, "Robust Robotic Localization using Visible Light Positioning and Inertial Fusion," *IEEE Sens. J.*, pp. 1–1, 2021, doi: 10.1109/JSEN.2021.3053342.
- [173] J. Fang *et al.*, "High-Speed Indoor Navigation System based on Visible Light and Mobile Phone," *IEEE Photonics J.*, vol. 9, no. 2, pp. 1–11, Apr. 2017, doi: 10.1109/JPHOT.2017.2687947.
- [174] M. Saadi, T. Ahmad, Y. Zhao, and L. Wuttistitikulkij, "An LED Based Indoor Localization System Using k-Means Clustering," in *2016 15th IEEE International Conference on Machine Learning and Applications (ICMLA)*, Anaheim, CA, USA, Dec. 2016, pp. 246–252. doi: 10.1109/ICMLA.2016.0048.
- [175] C.-W. Hsu, S. Liu, F. Lu, C.-W. Chow, C.-H. Yeh, and G.-K. Chang, "Accurate Indoor Visible Light Positioning System utilizing Machine Learning Technique with Height Tolerance," in *Optical Fiber Communication Conference*, San Diego, California, 2018, p. M2K.2. doi: 10.1364/OFC.2018.M2K.2.
- [176] H. Tran and C. Ha, "Improved Visible Light-Based Indoor Positioning System Using Machine Learning Classification and Regression," *Appl. Sci.*, vol. 9, no. 6, p. 1048, Mar. 2019, doi: 10.3390/app9061048.
- [177] H. H. Heqing Huang, A. Y. Aiying Yang, L. F. Lihui Feng, G. N. Guoqiang Ni, and P. G. and Peng Guo, "Artificial neural-network-based visible light positioning algorithm with a diffuse optical channel," *Chin. Opt. Lett.*, vol. 15, no. 5, pp. 050601–050605, 2017, doi: 10.3788/col201715.050601.
- [178] B. Lin, Q. Guo, C. Lin, X. Tang, Z. Zhou, and Z. Ghassemlooy, "Experimental demonstration of an indoor positioning system based on artificial neural network," *Opt. Eng.*, vol. 58, no. 01, p. 1, Jan. 2019, doi: 10.1117/1.OE.58.1.016104.
- [179] H. Nishikata *et al.*, "Basis research of indoor positioning method using visible light communication and dead reckoning," presented at the Proceedings of the 2011 International Conference on Indoor Positioning and Indoor Navigation (IPIN), 2011.
- [180] W. Gu, W. Zhang, J. Wang, M. R. Amini Kashani, and M. Kavehrad, "Three dimensional indoor positioning based on visible light with Gaussian mixture sigma-point particle filter technique," presented at the SPIE OPTO, San Francisco, California, United States, Feb. 2015, p. 93870O. doi: 10.1117/12.2076607.
- [181] D. Zheng, K. Cui, B. Bai, G. Chen, and J. A. Farrell, "Indoor localization based on LEDs," presented at the 2011 IEEE International Conference on Control Applications (CCA), 2011, pp. 573–578.

- [182] D. Plets, Y. Almadani, S. Bastiaens, M. Ijaz, L. Martens, and W. Joseph, "Efficient 3D trilateration algorithm for visible light positioning," *J. Opt.*, vol. 21, no. 5, p. 05LT01, May 2019, doi: 10.1088/2040-8986/ab1389.
- [183] N. Chaudhary, L. N. Alves, and Z. Ghassemlooy, "Impact of Transmitter Positioning and Orientation Uncertainty on RSS-Based Visible Light Positioning Accuracy," *Sensors*, vol. 21, no. 9, p. 3044, Apr. 2021, doi: 10.3390/s21093044.
- [184] W. Gu, M. Aminikashani, P. Deng, and M. Kavehrad, "Impact of Multipath Reflections on the Performance of Indoor Visible Light Positioning Systems," *J. Light. Technol.*, vol. 34, no. 10, pp. 2578–2587, May 2016, doi: 10.1109/JLT.2016.2541659.
- [185] Q. Peng, W. Guan, Y. Wu, Y. Cai, C. Xie, and P. Wang, "Three-dimensional high-precision indoor positioning strategy using Tabu search based on visible light communication," *Opt. Eng.*, vol. 57, no. 01, p. 1, 2018, doi: 10.1117/1.oe.57.1.016101.
- [186] C. T. Nguyen *et al.*, "A Comprehensive Survey of Enabling and Emerging Technologies for Social Distancing—Part I: Fundamentals and Enabling Technologies," *IEEE Access*, vol. 8, pp. 153479–153507, 2020.
- [187] J. Luo, L. Fan, and H. Li, "Indoor Positioning Systems Based on Visible Light Communication: State of the Art," *IEEE Commun. Surv. Tutor.*, vol. 19, no. 4, pp. 2871–2893, 2017, doi: 10.1109/COMST.2017.2743228.
- [188] J. Armstrong, Y. A. Sekercioglu, and A. Neild, "Visible Light Positioning: A Roadmap for International Standardization," *IEEE Commun. Mag.*, vol. 51, no. 12, pp. 68–73, Dec. 2013, doi: 10.1109/mcom.2013.6685759.
- [189] P. Chvojka, S. Zvanovec, P. A. Haigh, and Z. Ghassemlooy, "Channel Characteristics of Visible Light Communications Within Dynamic Indoor Environment," *J. Light. Technol.*, vol. 33, no. 9, pp. 1719–1725, 2015, doi: 10.1109/JLT.2015.2398894.
- [190] W. Gu, M. Aminikashani, P. Deng, and M. Kavehrad, "Impact of Multipath Reflections on the Performance of Indoor Visible Light Positioning Systems," *J. Light. Technol.*, vol. 34, no. 10, pp. 2578–2587, May 2016, doi: 10.1109/jlt.2016.2541659.
- [191] David Plets, Abdülkadir Eryildirim, Sander Bastiaens, Nobby Stevens, Luc Martens, and Wout Joseph, "A Performance Comparison of Different Cost Functions for RSS-Based Visible Light Positioning Under the Presence of Reflections," presented at the Proceedings of the 4th ACM Workshop on Visible Light Communication Systems, Snowbird, Utah, USA, 2017.
- [192] Y. Liu, J. Zhang, Y. Liu, B. Chen, S. Liu, and Y. Zuo, *A new indoor visible light positioning scheme to reduce the influence of reflections*, vol. 11048. SPIE, 2019.
- [193] J.-Y. Wang, Q.-L. Li, J.-X. Zhu, and Y. Wang, "Impact of receiver's tilted angle on channel capacity in VLCs," *Electron. Lett.*, vol. 53, no. 6, Mar. 2017, doi: 10.1049/el.2016.4657.
- [194] D. Plets, S. Bastiaens, L. Martens, and W. Joseph, "An Analysis of the Impact of LED Tilt on Visible Light Positioning Accuracy," *Electronics*, vol. 8, no. 4, 2019.
- [195] Willem Raes and Nobby Stevens, "Performance Assessment of Artificial Neural Networks on the RSS-Based Visible Light Positioning Accuracy with Random Transmitter Tilt," presented at the International Symposium on Communication Systems, Networks and Digital Signal Processing (CSNDSP), 2020.
- [196] W. Lixuan, G. Caili, P. Luo, and Q. Li, "Indoor visible light localization algorithm based on received signal strength ratio with multi-directional LED array," presented at the 2017 IEEE International Conference on Communications Workshops (ICC Workshops), May 2017, pp. 138–143. doi: 10.1109/ICCW.2017.7962647.
- [197] L. Yin, X. Wu, and H. Haas, "Indoor Visible Light Positioning with Angle Diversity Transmitter," presented at the 2015 IEEE 82nd Vehicular Technology Conference (VTC2015-Fall), Sep. 2015, pp. 1–5. doi: 10.1109/VTCFall.2015.7390984.

- [198] B. Zhou, A. Liu, and V. Lau, "Performance Limits of Visible Light-Based User Position and Orientation Estimation Using Received Signal Strength Under NLOS Propagation," *IEEE Trans. Wirel. Commun.*, vol. 18, no. 11, pp. 5227–5241, 2019, doi: 10.1109/TWC.2019.2934689.
- [199] F. Miramirkhani and M. Uysal, "Channel Modeling and Characterization for Visible Light Communications," *IEEE Photonics J.*, vol. 7, no. 6, pp. 1–16, 2015.
- [200] M. Uysal, F. Miramirkhani, O. Narmanlioglu, T. Baykas, and E. Panayirci, "IEEE 802.15.7r1 Reference Channel Models for Visible Light Communications," *IEEE Commun. Mag.*, vol. 55, no. 1, pp. 212–217, 2017, doi: 10.1109/MCOM.2017.1600872CM.
- [201] Z. Nazari Chaleshtori, Z. Ghassemlooy, H. B. Eldeeb, M. Uysal, and S. Zvanovec, "Utilization of an OLED-Based VLC System in Office, Corridor, and Semi-Open Corridor Environments," *Sensors*, vol. 20, no. 23, 2020, doi: 10.3390/s20236869.
- [202] Z. Ghassemlooy, W. Popoola, and S. Rajbhandari, *Optical wireless communications: system and channel modelling with Matlab®*. CRC press, 2019.
- [203] N. Chaudhary, L. N. Alves, and Z. Ghassemlooy, "Feasibility Study of Reverse Trilateration Strategy with a Single Tx for VLP," in *2019 2nd West Asian Colloquium on Optical Wireless Communications (WACOWC)*, Tehran, Iran, Apr. 2019, pp. 121–126. doi: 10.1109/WACOWC.2019.8770213.
- [204] O. I. Younus, H. Le Minh, P. T. Dat, N. Yamamoto, A. T. Pham, and Z. Ghassemlooy, "Dynamic Physical-Layer Secured Link in a Mobile MIMO VLC System," *IEEE Photonics J.*, vol. 12, no. 3, pp. 1–14, 2020.
- [205] J. Rufo, J. Rabadan, V. Guerra, and R. Perez-Jimenez, "BRDF Models for the Impulse Response Estimation in Indoor Optical Wireless Channels," *IEEE Photonics Technol. Lett.*, vol. 29, no. 17, pp. 1431–1434, Sep. 2017, doi: 10.1109/LPT.2017.2723543.
- [206] C. E. De Normalisation, "EN 12464-1: Light and Lighting-Lighting of work places, Part 1: Indoor work places," *Com. Eur. Norm.*, 2002.
- [207] S. Shawky, M. A. El-Shimy, Z. A. El-Sahn, M. R. M. Rizk, and M. H. Aly, "Improved VLC-based indoor positioning system using a regression approach with conventional RSS techniques," presented at the 2017 13th International Wireless Communications and Mobile Computing Conference (IWCMC), Jun. 2017, pp. 904–909.
- [208] X. Sun, J. Duan, Y. Zou, and A. Shi, "Impact of multipath effects on theoretical accuracy of TOA-based indoor VLC positioning system," *Photonics Res.*, vol. 3, no. 6, pp. 296–299, Dec. 2015, doi: 10.1364/prj.3.000296.
- [209] Yole Développement, *Complementary metal–oxide–semiconductor (CMOS) camera module market size worldwide in 2019 and 2025, by component (in billion U.S. dollars)*. 2020.
- [210] Z. Ghassemlooy, L. N. Alves, S. Zvanovec, and M.-A. Khalighi, *Visible light communications: theory and applications*. CRC press, 2017.
- [211] W. Maddern and P. Newman, "Real-time probabilistic fusion of sparse 3D LIDAR and dense stereo," in *2016 IEEE/RSJ International Conference on Intelligent Robots and Systems (IROS)*, Oct. 2016, pp. 2181–2188. doi: 10.1109/IROS.2016.7759342.
- [212] O. I. Younus *et al.*, "Data Rate Enhancement in Optical Camera Communications Using an Artificial Neural Network Equaliser," *IEEE Access*, vol. 8, pp. 42656–42665, 2020, doi: 10.1109/ACCESS.2020.2976537.
- [213] I. Moreno and C.-C. Sun, "Modeling the radiation pattern of LEDs," *Opt. Express*, vol. 16, no. 3, pp. 1808–1819, Feb. 2008, doi: 10.1364/OE.16.001808.
- [214] N. B. Hassan, Z. Ghassemlooy, S. Zvanovec, P. Luo, and H. Le-Minh, "Non-line-of-sight $2 \times N$ indoor optical camera communications," *Appl. Opt.*, vol. 57, no. 7, pp. B144–B149, Mar. 2018, doi: 10.1364/AO.57.00B144.
- [215] M. Kashiwagi, N. Mishima, T. Kozakaya, and S. Hiura, "Deep Depth From Aberration Map," in *2019 IEEE/CVF International Conference on Computer Vision (ICCV)*, Nov. 2019, pp. 4069–4078. doi: 10.1109/ICCV.2019.00417.

- [216] S. W. Bailey, J. I. Echevarria, B. Bodenheimer, and D. Gutierrez, "Fast depth from defocus from focal stacks," *Vis. Comput.*, vol. 31, no. 12, pp. 1697–1708, Dec. 2015, doi: 10.1007/s00371-014-1050-2.
- [217] E. Eso, Z. Ghassemlooy, S. Zvanovec, J. Sathian, M. M. Abadi, and O. I. Younus, "Performance of Vehicular Visible Light Communications under the Effects of Atmospheric Turbulence with Aperture Averaging," *Sensors*, vol. 21, no. 8, 2021, doi: 10.3390/s21082751.
- [218] "Franka Emika," *The reference robot platform for academic research*. <https://www.franka.de/robot-system/>
- [219] Z. Ghassemlooy, *Optical Wireless Communications*, Second Edition. CRC Press, 2019.
- [220] W. Chujo and M. Kinoshita, "Rolling-Shutter-Based QPSK by Spatial Luminance Distribution for Optical Camera Communication," presented at the 2018 IEEE Globecom Workshops (GC Wkshps), Dec. 2018, pp. 1–6. doi: 10.1109/GLOCOMW.2018.8644404.
- [221] V. P. Rachim and W. Chung, "Multilevel Intensity-Modulation for Rolling Shutter-Based Optical Camera Communication," *IEEE Photonics Technol. Lett.*, vol. 30, no. 10, pp. 903–906, 2018, doi: 10.1109/LPT.2018.2823784.
- [222] L. Liu, R. Deng, and L. Chen, "Spatial and Time Dispersions Compensation With Double-Equalization for Optical Camera Communications," *IEEE Photonics Technol. Lett.*, vol. 31, no. 21, pp. 1753–1756, 2019, doi: 10.1109/LPT.2019.2945405.
- [223] C. Danakis, M. Afgani, G. Povey, I. Underwood, and H. Haas, "Using a CMOS camera sensor for visible light communication," presented at the 2012 IEEE Globecom Workshops, Dec. 2012, pp. 1244–1248. doi: 10.1109/GLOCOMW.2012.6477759.
- [224] J. Ferrandiz-Lahuerta, D. Camps-Mur, and J. Paradells-Aspas, "A Reliable Asynchronous Protocol for VLC Communications Based on the Rolling Shutter Effect," presented at the 2015 IEEE Global Communications Conference (GLOBECOM), Dec. 2015, pp. 1–6. doi: 10.1109/GLOCOM.2015.7417229.
- [225] T. Sonoda, H. Nagahara, K. Endo, Y. Sugiyama, and R. Taniguchi, "High-speed imaging using CMOS image sensor with quasi pixel-wise exposure," presented at the 2016 IEEE International Conference on Computational Photography (ICCP), May 2016, pp. 1–11. doi: 10.1109/ICCPHOT.2016.7492875.
- [226] Y.-S. Kuo, P. Pannuto, K.-J. Hsiao, and P. Dutta, "Luxapose Indoor Positioning with Mobile Phones and Visible Light," presented at the Proceedings of the 20th annual international conference on Mobile computing and networking - MobiCom '14, 2014.
- [227] T. Zinda, K. Ito, and W. Chujo, "Rolling-Shutter-Based Optical Camera Communication Using Distributed LED Array," presented at the 2018 11th International Symposium on Communication Systems, Networks & Digital Signal Processing (CSNDSP), Jul. 2018, pp. 1–4. doi: 10.1109/CSNDSP.2018.8471879.
- [228] N. Bani Hassan *et al.*, "Non-Line-of-Sight MIMO Space-Time Division Multiplexing Visible Light Optical Camera Communications," *J. Light. Technol.*, vol. 37, no. 10, pp. 2409–2417, May 2019.
- [229] Y. Yang and J. Luo, "Composite Amplitude-Shift Keying for Effective LED-Camera VLC," *IEEE Trans. Mob. Comput.*, pp. 1–1, 2019, doi: 10.1109/TMC.2019.2897101.
- [230] P. A. Haigh *et al.*, "A MIMO-ANN system for increasing data rates in organic visible light communications systems," presented at the 2013 IEEE International Conference on Communications (ICC), Jun. 2013, pp. 5322–5327. doi: 10.1109/ICC.2013.6655433.
- [231] S. Rajbhandari, J. Faith, Z. Ghassemlooy, and M. Angelova, "Comparative study of classifiers to mitigate intersymbol interference in diffuse indoor optical wireless communication links," *Optik*, vol. 124, no. 20, pp. 4192–4196, Oct. 2013, doi: <https://doi.org/10.1016/j.ijleo.2012.12.040>.
- [232] X. Li, N. B. Hassan, A. Burton, Z. Ghassemlooy, S. Zvanovec, and R. Perez-Jimenez, "A Simplified Model for the Rolling Shutter Based Camera in Optical Camera

- Communications,” presented at the 2019 15th International Conference on Telecommunications (ConTEL), Jul. 2019, pp. 1–5.
- [233] L. Liu, R. Deng, and L.-K. Chen, “47-kbit/s RGB-LED-based optical camera communication based on 2D-CNN and XOR-based data loss compensation,” *Opt. Express*, vol. 27, no. 23, pp. 33840–33846, Nov. 2019, doi: 10.1364/OE.27.033840.
 - [234] D. T. Nguyen, S. Park, Y. Chae, and Y. Park, “VLC/OCC Hybrid Optical Wireless Systems for Versatile Indoor Applications,” *IEEE Access*, vol. 7, pp. 22371–22376, 2019, doi: 10.1109/ACCESS.2019.2898423.
 - [235] J. C. Chau and T. D. C. Little, “Analysis of CMOS active pixel sensors as linear shift-invariant receivers,” presented at the 2015 IEEE International Conference on Communication Workshop (ICCW), Jun. 2015, pp. 1398–1403. doi: 10.1109/ICCW.2015.7247374.
 - [236] P. A. Haigh, Z. Ghassemlooy, S. Rajbhandari, I. Papakonstantinou, and W. Popoola, “Visible Light Communications: 170 Mb/s Using an Artificial Neural Network Equalizer in a Low Bandwidth White Light Configuration,” *J. Light. Technol.*, vol. 32, no. 9, pp. 1807–1813, 2014, doi: 10.1109/JLT.2014.2314635.
 - [237] H. Brink, J. Richards, and M. Fetherolf, *Real-world machine learning*. Manning Publications Co., 2016.
 - [238] X. Lu *et al.*, “Memory-controlled deep LSTM neural network post-equalizer used in high-speed PAM VLC system,” *Opt. Express*, vol. 27, no. 5, pp. 7822–7833, Mar. 2019, doi: 10.1364/OE.27.007822.
 - [239] B. Zamanlooy and M. Mirhassani, “Efficient VLSI Implementation of Neural Networks With Hyperbolic Tangent Activation Function,” *IEEE Trans. Very Large Scale Integr. VLSI Syst.*, vol. 22, no. 1, pp. 39–48, 2014, doi: 10.1109/TVLSI.2012.2232321.
 - [240] S. Rajbhandari, Z. Ghassemlooy, and M. Angelova, “Effective Denoising and Adaptive Equalization of Indoor Optical Wireless Channel With Artificial Light Using the Discrete Wavelet Transform and Artificial Neural Network,” *J. Light. Technol.*, vol. 27, no. 20, pp. 4493–4500, 2009, doi: 10.1109/JLT.2009.2024432.
 - [241] S. R. Teli, S. Zvanovec, and Z. Ghassemlooy, “Performance evaluation of neural network assisted motion detection schemes implemented within indoor optical camera based communications,” *Opt. Express*, vol. 27, no. 17, pp. 24082–24092, Aug. 2019, doi: 10.1364/OE.27.024082.
 - [242] W. Saputra, Tulus, M. Zarlis, R. W. Sembiring, and D. Hartama, “Analysis Resilient Algorithm on Artificial Neural Network Backpropagation,” *J. Phys. Conf. Ser.*, vol. 930, p. 012035, Dec. 2017, doi: 10.1088/1742-6596/930/1/012035.
 - [243] M. Riedmiller and H. Braun, “A direct adaptive method for faster backpropagation learning: the RPROP algorithm,” presented at the IEEE International Conference on Neural Networks, Apr. 1993, pp. 586–591 vol.1. doi: 10.1109/ICNN.1993.298623.
 - [244] A. Loukas, A. Simonetto, and G. Leus, “Distributed Autoregressive Moving Average Graph Filters,” *IEEE Signal Process. Lett.*, vol. 22, no. 11, pp. 1931–1935, 2015, doi: 10.1109/LSP.2015.2448655.
 - [245] S. Kak, “Unary coding for neural network learning,” *ArXiv Prepr. ArXiv10094495*, 2010.
 - [246] E. Eso *et al.*, “Experimental Demonstration of Vehicle to Road Side Infrastructure Visible Light Communications,” in *2019 2nd West Asian Colloquium on Optical Wireless Communications (WACOWC)*, Tehran, Iran, Apr. 2019, pp. 85–89. doi: 10.1109/WACOWC.2019.8770186.
 - [247] N. Saeed, S. Guo, K.-H. Park, T. Y. Al-Naffouri, and M.-S. Alouini, “Optical camera communications: Survey, use cases, challenges, and future trends,” *Phys. Commun.*, vol. 37, p. 100900, Dec. 2019, doi: <https://doi.org/10.1016/j.phycom.2019.100900>.
 - [248] Hui-Yu Lee, Hao-Min Lin, Yu-Lin Wei, Hsin-I Wu, Hsin-Mu Tsai, and Kate Ching-Ju Lin, “RollingLight: Enabling Line-of-Sight Light-to-Camera Communications,” presented at

- the Proceedings of the 13th Annual International Conference on Mobile Systems, Applications, and Services, Florence, Italy, 2015.
- [249] T. Nguyen, A. Islam, T. Hossan, and Y. M. Jang, "Current Status and Performance Analysis of Optical Camera Communication Technologies for 5G Networks," *IEEE Access*, vol. 5, pp. 4574–4594, 2017, doi: 10.1109/ACCESS.2017.2681110.
 - [250] E. Eso, S. Teli, N. Bani Hassan, S. Vitek, Z. Ghassemlooy, and S. Zvanovec, "400 m rolling-shutter-based optical camera communications link," *Opt. Lett.*, vol. 45, no. 5, pp. 1059–1062, Mar. 2020, doi: 10.1364/OL.385423.
 - [251] S. Lauxtermann, A. Lee, J. Stevens, and A. Joshi, "Comparison of global shutter pixels for CMOS image sensors," presented at the 2007 International Image Sensor Workshop, 2007, p. 8.
 - [252] A. Sturniolo *et al.*, "ROI Assisted Digital Signal Processing for Rolling Shutter Optical Camera Communications," presented at the 2018 11th International Symposium on Communication Systems, Networks & Digital Signal Processing (CSNDSP), Jul. 2018, pp. 1–6. doi: 10.1109/CSNDSP.2018.8471770.
 - [253] T. Nguyen, A. Islam, T. Yamazato, and Y. M. Jang, "Technical Issues on IEEE 802.15.7m Image Sensor Communication Standardization," *IEEE Commun. Mag.*, vol. 56, no. 2, pp. 213–218, 2018, doi: 10.1109/MCOM.2018.1700134.
 - [254] W. A. Cahyadi, Y. H. Chung, Z. Ghassemlooy, and N. B. Hassan, "Optical Camera Communications: Principles, Modulations, Potential and Challenges," *Electronics*, vol. 9, no. 9, p. 1339, 2020.
 - [255] P. Luo, Z. Ghassemlooy, H. Le Minh, X. Tang, and H.-M. Tsai, "Undersampled phase shift ON-OFF keying for camera communication," presented at the 2014 Sixth International Conference on Wireless Communications and Signal Processing (WCSP), 2014.
 - [256] P. Luo, Z. Ghassemlooy, H. L. Minh, H. Tsai, and X. Tang, "Undersampled-PAM with subcarrier modulation for camera communications," presented at the 2015 Opto-Electronics and Communications Conference (OECC), Jul. 2015, pp. 1–3. doi: 10.1109/OECC.2015.7340212.
 - [257] V. P. Rachim and W.-Y. Chung, "Multilevel intensity-modulation for rolling shutter-based optical camera communication," *IEEE Photonics Technol. Lett.*, vol. 30, no. 10, pp. 903–906, 2018.
 - [258] P. Hu, P. H. Pathak, H. Zhang, Z. Yang, and P. Mohapatra, "High Speed LED-to-Camera Communication using Color Shift Keying with Flicker Mitigation," *IEEE Trans. Mob. Comput.*, vol. 19, no. 7, pp. 1603–1617, 2020, doi: 10.1109/TMC.2019.2913832.
 - [259] P. Luo *et al.*, "Experimental demonstration of RGB LED-based optical camera communications," *IEEE Photonics J.*, vol. 7, no. 5, pp. 1–12, 2015.
 - [260] A. D. Griffiths, J. Herrnsdorf, M. J. Strain, and M. D. Dawson, "Scalable visible light communications with a micro-LED array projector and high-speed smartphone camera," *Opt. Express*, vol. 27, no. 11, pp. 15585–15594, May 2019, doi: 10.1364/OE.27.015585.
 - [261] C. Willy Anugrah and C. Yeon Ho, "Smartphone camera-based device-to-device communication using neural network-assisted high-density modulation," *Opt. Eng.*, vol. 57, no. 9, pp. 1–9, Spring 2018, doi: 10.1117/1.OE.57.9.096102.
 - [262] A. Islam, M. T. Hossan, and Y. M. Jang, "Convolutional neural networkscheme-based optical camera communication system for intelligent Internet of vehicles," *Int. J. Distrib. Sens. Netw.*, vol. 14, no. 4, p. 1550147718770153, Apr. 2018, doi: 10.1177/1550147718770153.
 - [263] O. Isam Younus *et al.*, "An Artificial Neural Network Equalizer for Constant Power 4-PAM in Optical Camera Communications," presented at the 2020 12th International Symposium on Communication Systems, Networks and Digital Signal Processing (CSNDSP), Jul. 2020, pp. 1–6. doi: 10.1109/CSNDSP49049.2020.9249579.
 - [264] H. Nguyen, T. L. Pham, H. Nguyen, and Y. M. Jang, "Trade-off Communication distance and Data rate of Rolling shutter OCC," in *2019 Eleventh International Conference on*

- Ubiquitous and Future Networks (ICUFN)*, Jul. 2019, pp. 148–151. doi: 10.1109/ICUFN.2019.8806101.
- [265] B. Lehman, A. Wilkins, S. Berman, M. Poplawski, and N. J. Miller, “Proposing measures of flicker in the low frequencies for lighting applications,” presented at the 2011 IEEE Energy Conversion Congress and Exposition, 2011, pp. 2865–2872.
- [266] D. L. DiLaura, K. Houser, R. Mistrick, and G. R. Steffy, “The lighting handbook: reference and application,” 2011.
- [267] S. Rajbhandari *et al.*, “Neural Network-Based Joint Spatial and Temporal Equalization for MIMO-VLC System,” *IEEE Photonics Technol. Lett.*, vol. 31, no. 11, pp. 821–824, 2019, doi: 10.1109/LPT.2019.2909139.
- [268] ON Semiconductor, “1.3Mp CMOS Digital Image Sensor.” Semiconductor Components Industries, LLC: Aurora, CO, USA, 2017. Accessed: Mar. 20, 2021. [Online]. Available: <https://www.onsemi.com/pdf/datasheet/mt9m131-d.pdf>
- [269] G. Cossu, A. Sturniolo, and E. Ciaramella, “Modelization and Characterization of a CMOS Camera as an Optical Real-Time Oscilloscope,” *IEEE Photonics J.*, vol. 12, no. 6, pp. 1–13, 2020, doi: 10.1109/JPHOT.2020.3032951.
- [270] Intel, “AN 835: PAM4 Signaling Fundamentals.” Intel Corporation: USA, 2019. Accessed: Mar. 10, 2021. [Online]. Available: <https://www.intel.com/content/dam/www/programmable/us/en/pdfs/literature/an/an835.pdf>